Study on UV Excitable Lanthanide Doped M-SiAlON (M = La, Sr) Phosphors for White LEDs

Chunyun Wang

Graduate School of Chemical Sciences and Engineering

Hokkaido University

July 2017

Table of contents

Abstract

Phosphor-converted white light-emitting diodes (pc-wLEDs) have been widely used for lighting and displays because of their high energy conversion efficiency, long lifetime and environmental benefits. However, pc-wLEDs with a higher luminous efficacy and better color rendition are urgently required, especially for illumination-grade light sources. Pc-wLEDs based on a blue LED chip and a yellow-emitting phosphor (typically $Y_3Al_5O_{12}:Ce^{3+}$) suffer from a low color rendering. A better color rendering can be achieved if a near-UV LED chip is combined with multiple phosphors. Moreover, the color will be more stable for near-UV pumping LEDs as it is independent of the driven current and the temperature of the chips. Since the energy of UV or near UV light is much stronger than blue light, the phosphors required for UV or near UV-LEDs need to be more thermally stable and robust. However, the number of phosphors that can be efficiently excited with UV or near UV light and have high quantum efficiency and good thermal stability is very limited. Ce^{3+} and Eu^{2+} doped nitride and oxynitride phosphors have been reported with good chemical and thermal stability, as well as high luminescence efficiency. In this thesis, the focus is on developing novel UV or near-UV excitable oxynitride phosphors for white LEDs. The synthesis, structure and photoluminescence properties of these phosphors are investigated.

Chapter 1 elaborates on the scope of my PhD research. The concept of pc-wLEDs is described, discussing different approaches to obtain white LEDs by using luminescent materials. In addition, I focus on the theoretical background of luminescence and the selection criteria of white LED phosphors. The effects of host lattice on the energy levels of lanthanide activators, such as centroid shift, crystal field splitting and Stokes shift are discussed. The method to construct an energy level scheme that positions 4f and 5d levels of lanthanide ions with respect to the valence band of the host material is explained.

Chapter 2 describes the solid-state reaction method that is used to synthesize the oxynitride phosphors that are investigated. The structural characterization techniques such as XRD, NMR and SEM are briefly explained. Also discussed are the optical characterization methods that have been used to study the luminescence properties. Examples hereof are photoluminescence spectroscopy, temperature dependent measurements, quantum efficiency and time-resolved luminescence decay.

Chapter 3 and chapter 4 study synthesis and photoluminescence properties of Eu, Ce, Sm, Yb doped $LaAl(Si_{6-z}Al_z)(N_{10-z}O_z)$ (termed JEM, $z \approx 1$) phosphors. Ce doped JEM phosphor has been reported as a promising blue-emitting phosphor for white LEDs using near-UV excitation, particularly for home

illumination. However, the unavailability of a phase pure JEM:Ce phosphor prevents widespread application. In addition, there was no report on the photoluminescence properties of an Eu^{2+} doped JEM phosphor. Chapters 3 focuses on synthesis and photoluminescence properties of Eu doped JEM phosphor. Phase pure JEM:Eu phosphors have been obtained by carefully controlling the sintering temperature and chemical composition of starting materials (z value, N/O ratio and Si/Al ratio). Photoluminescence properties including photoluminescence spectra, the red-shift of emission, thermal quenching and luminescence decay have been investigated for the first time. It was found that JEM:Eu phosphor emits green light after UV excitation and its emission band largely redshifts with increasing Eu concentration. This phosphor shows an unusual thermal quenching behavior and double exponential decay due to different Eu local environments, although there is only one crystallographic site which Eu can occupy.

Chapter 4 further studies the synthesis and photoluminescence properties of Ce, Sm, Yb doped JEM phosphors. JEM:Ce phosphor shows higher quantum efficiency and better thermal stability than JEM:Eu phosphor. An energy level scheme has been constructed by investigating the redshift of Ce^{3+} and Eu^{2+} ions, the charge transfer transitions of Yb and Sm, the centroid shift of Ce^{3+} and the chemical shift of Eu^{2+} ions in JEM. The scheme contains the positions of the 4f and 5d levels of all divalent and trivalent lanthanide ions with respect to the valence band of JEM, and allows the prediction and explanation of the photoluminescence properties of lanthanide ions doped JEM phosphors.

Chapter 5 investigates the photoluminescence properties of Ce doped Al-containing La N(ew)-phase $La_3Si_{8-x}Al_xN_{11-x}O_{4+x}$ (x = 1.5) phosphor and its application for white LEDs. The effect of Al-O substitution for Si-N and the effect of Ce concentration on phosphor performance have been studied. Solid state ^{29}Si and ^{27}Al NMR have been used to study the local coordinations. $La_3Si_{6.5}Al_{1.5}N_{9.5}O_{5.5}$:Ce phosphor shows deep blue emission with a narrow emission band after UV or near-UV excitation with high quantum efficiency and color purity. A white LED containing $La_3Si_{6.5}Al_{1.5}N_{9.5}O_{5.5}$:0.05Ce phosphor as the blue phosphor has high color rendering index, showing the great potential of the phosphor for white LEDs.

In chapter 6, a new Sr-sialon phase $Sr_{3.6}Si_{16.2}Al_{5.4}O_{3.6}N_{27}$ is described that I discovered during my PhD research. The photoluminescence properties when doped with Eu or Ce are investigated. Ce^{3+} doped Sr-sialon phosphor shows strong blue emission around 435 nm with a fwhm ≈ 90 nm after 355 nm light excitation. The blue luminescence exhibits a small thermal quenching behavior at high temperature. Upon doping with Eu^{2+}, the emission band can be tuned from 487 nm to 541 nm by

increasing Eu concentration.

Finally, in chapter 7 the most important conclusions are summarized and an outlook is given on the potential of the UV-excitable sialon phosphors for white LED applications.

Chapter 1 Introduction

1.1 White LED

Global warming, caused by burning fossil fuels, has become a serious problem with noticeable climate changes, widespread melting of ice and rising sea levels. The development of green energy sources is therefore urgently needed, and energy efficiency has become an increasingly important criterion for new light sources. White LEDs (light emitting diodes) are considered as one of the most promising light sources, because of a higher efficiency (Figure 1.1a),[1] longer lifetime (100 000 h),[2] robustness, non-toxicity and smaller size compared to traditional lighting sources such as incandescent and fluorescent lamps.[2] LEDs are therefore already used for automotive headlamps, traffic lighting, aviation lighting and television screens. However, for general household lighting applications, white LEDs are necessary and there are still some challenges.

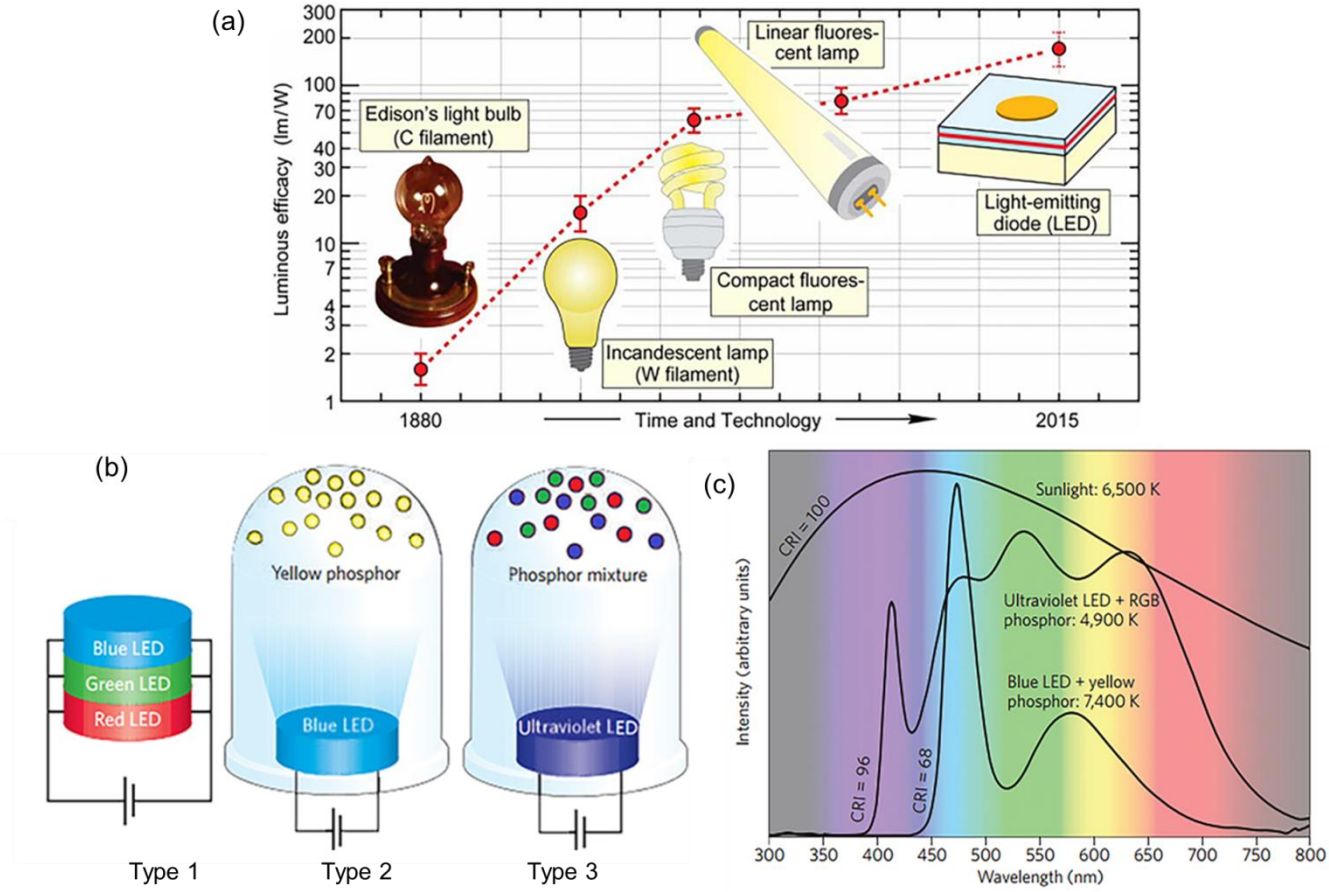

Figure 1.1 (a) Comparison of the luminous efficacy of several lighting technologies;[1](b) three dominant

ways to produce white LEDs; (c) comparison of the spectrum of ideal sunlight with two LED-based white-light sources.[3]

There are three dominant ways to generate white LEDs: (1) combination of red, green and blue LEDs; (2) a blue LED with a yellow phosphor; or (3) an ultraviolet LED with a mixture of red, green and blue phosphors, as shown in Figure 1.1b. In principle, the ideal approach to get a white LED is the multi-LED strategy (type 1) because in that case there is no energy-conversion loss due to the Stokes shift of the phosphor. However, the current low efficiency of yellow and green LEDs prevents multi-LED devices from achieving high efficiencies. In addition, the multi-LED approach suffers from poor color rendering, associated with the relatively narrow radiation components. Furthermore, different LED chips have different aging and responses to temperature and driving current. In order to counteract the different aging, the manipulation system will be more complicated and it will increase the cost.[4-5] It would be much cheaper if only one type of LED is used, like type 2 or 3. These two types are called phosphor-converted white LEDs (pc-white LEDs), because phosphors (luminescent materials) are used to convert the UV or blue light emitted by the InGaN/AlGaN-based LED into different colors of light. For type 2, although it has the lowest cost, the color rendering is too bad for indoor lighting, because the white light lacks a red component, as shown in Figure 1.1c. A better color rendering can be achieved by adding a red-emitting phosphor or replacing the single yellow-emitting phosphor (YAG:Ce) with a green-emitting phosphor and a red-emitting phosphor. The challenge is to develop red- and green-emitting phosphors that can be excited by a blue LED light at 450 – 470 nm.[2] Type 3 can also enhance the color rendering, but it depends on the availability of red- and green-emitting phosphors.[3] Compared to the type of a blue LED combined red- and green-emitting phosphors white LED, type 3 white LED has higher flexibility to get various white light and its emission color is more stable, because it is independent of the driven current and the temperature of the chips.[4]

The current state-of-the art commercial pc-LED for warm white light, with a luminous efficacy of approximately 137 lm/W, is about 33% efficient.[6] The package efficiency (33%) is equal to the product of the blue LED efficiency (66%), phosphor and mixing/scattering/absorption efficiency (63%), and white light spectra efficiency (78%).[6] An “upper pc-LED potential” with a luminous efficacy of 355 lm/W, or an efficiency of 61% can be considered if all other losses is eliminated except for the fundamental Stokes efficiency loss.[6] So there is great potential to improve the efficiency for pc-White LEDs.

1.2 Selections of phosphors for white LED

The phosphors are required to strongly absorb near UV or blue light and emit visible light at the desired wavelength with high efficiency, chemical and thermal stability, low thermal quenching and short lifetime (avoiding saturation effect). Furthermore the phosphors should be cheap and environmentally friendly.[5] Unfortunately, the number of phosphors that meet all these requirements is very limited and new phosphors need to be discovered.

1.2.1 Selection of lanthanide ions

Phosphors for white LED application are usually composed of an inert host lattice material with a wide band gap material (e.g. oxides, nitrides, and sulfides) and a small amount of a dopant ion (called an activator, which usually is a lanthanide ion or a transition metal ion).[5] So the composition of phosphors is usually written as host:activator (e.g. Y_2O_3:Eu^{3+}). This thesis focuses on the lanthanide ions as activators. Based on the electronic transitions associated with the optical absorption,[7] the candidate lanthanide ions can be classified into two categories:

(1) 4f→5d transition with band emission

Ce^{3+} ($4f^1$), Eu^{2+} ($4f^7$) and Yb^{2+} ($4f^{14}$) ions can be directly excited from a $4f^n$ state to $4f^{n-1}5d^1$ state and then emit through 5d-4f transitions with a broad band emission. Since the electrons of excited 5d states are diffuse and overlap with the host ligand orbitals, the 4f→5d transition is strongly affected by the host and activator combination, and the excitation and emission wavelength can be tuned by varying the composition of host and activator.

The Ce^{3+} ion has only one 4f electron and the 4f ground state is split into $^2F_{5/2}$ and $^2F_{7/2}$ levels with an energy difference of 2000 cm^{-1}. The emission energy depends strongly on the host crystal through the crystal-field splitting of the 5d states, and varies from near-ultraviolet to the green region. The decay time of the Ce^{3+} emission is 10^{-7} to 10^{-8} s, the shortest among the lanthanide ions. This is because the d→f transition is both parity-allowed and spin-allowed since $5d^1$ and $4f^1$ states are spin doublets.[7]

Eu^{2+} has the ground state of $4f^7$ ($^8S_{7/2}$) and the excited state $4f^65d^1$. The excitation spectrum of Eu^{2+} doped compounds is usually very broad, due to the splitting of the 5d excited state by the crystal field and the coupling to the multiple splitting of the $4f^6$ configuration.[5] The emission energy also strongly depends on the host lattice due to the crystal field splitting, varying from the near-UV to red. With increasing crystal field strength, the emission bands shift to longer wavelength. So Ce^{3+} and Eu^{2+} ions are the mostly used activators for white LED phosphors, owing to the high flexibility to tailor the emission. The lifetime of the Eu^{2+} luminescence is 10^{-5}~10^{-6} s.[7]

The luminescence of Yb^{2+} is due to $4f^{13}5d \rightarrow 4f^{14}$ transition, with the emission color varying from UV to red. In general, the 5d-4f emission energies of Eu^{2+} and Yb^{2+} in inorganic compounds are expected to be similar within 0.1 eV.[8] However, the thermal quenching resulting from thermal ionization is usually more serious for Yb^{2+} emission than Eu^{2+} emission, since the lowest 5d state of Yb^{2+} is much closer to the bottom of conduction band.[8] In addition, the relatively long decay time of Yb^{2+} (1 - 10 ms)[9] could lead to saturation for high excitation flux. These characters make Yb^{2+} less suitable as conversion phosphors for white LED application.[5]

(2) 4f→4f transition with line emissions

Most trivalent rare earth ions except for Ce^{3+} can yield line emissions due to 4f↔4f transitions, which are hardly affected by the host compound, because the 4f electrons are well shielded by the 5s and 5p electrons. Tb^{3+}, Er^{3+} and Dy^{3+} emit in the green-yellow region, and Pr^{3+}, Sm^{3+} and Eu^{3+} emit in the orange-red region.[10] Especially Tb^{3+} (main peak near 545 nm) and Eu^{3+} (main peak near 600 or 620 nm) have been widely used in fluorescent lamps or cathode ray tubes.[5] These phosphors are excited through charge transfer bands or 4f→5d transitions, and emissions occur through 4f→4f transitions. For these rare-earth ions with 4f→4f line emission doped compounds, their apparently limited efficiency, in combination with a lack of efficient broad band excitation in the near-UV and blue makes them less suitable for white LED application.[5]

The sensitizing approach through the appropriate addition of co-dopants can extend the excitation spectrum. It has been reported that Tb^{3+} f→f emission can be sensitized by the addition of Ce^{3+} such as a well-known phosphor $LaPO_4:Ce^{3+}$, Tb^{3+} that is used in fluorescent lamps,[11] and Eu^{3+} can be sensitized by Bi^{3+} in $ZnB_2O_4:Bi^{3+},Eu^{3+}$ phosphor.[12] Phosphors displaying broad absorption bands accompanied by narrow band emissions through f→f transitions have the advantage that the intra- and inter-phosphor absorption of radiation will be avoided. If an efficient, sensitized trivalent lanthanide ions based phosphors is identified, it could be of importance for low flux LED applications.[11]

1.2.2 Selection of host materials

The host materials for the LED phosphor should be thermally and chemically stable in order to resist the heat produced by LED chips during operation, especially for high powder white LEDs. The material should also be optically transparent for the emitted light and the emission of the pumping LED, which limits the choice to materials with a wide band gap. Finally, the phosphor production process should also be cheap and last but not least environmentally friendly.[5]

The garnet structure based host is one of the most widely used hosts for white LED phosphors in industry. $(Y_{1-a}Gd_a)(Al_{1-b}Ga_b)O_{12}:Ce^{3+}$ ($YAG:Ce^{3+}$) yellow emitting phosphor is widely used with (Ga, In)N diodes as a down-converting phosphor to make white light. However, this type of white LED suffers from low color rendering and high correlated color temperature for general illumination, as discussed in section 1. For most oxide-based phosphors, the shift of the emission band to longer wavelength and the flexibility of structural variety is limited compared to nitride- or oxynitride-based phosphors, making them less interesting for white LED application. Most sulfide-based phosphors are usually very sensitive to moisture and not thermally stable.

Silicon-based nitrides and oxynitrides have received great attention as hosts for white LED phosphors due to their unique and rigid crystal structures, structural diversity, high chemical and thermal stability, and suitable crystal sites for activators,[13] which are generally formed from highly condensed networks by corner-sharing SiX_4 (X = N, O) tetrahedra. The structural variety of silicon-based nitrides can be widely extended by introducing alkaline-earth ions and rare-earth ions, or by the partial substitution of Si-N by Al-O or Si-C, forming a large group of compounds, such as M-Si-N, M-Ln-Si-N, Ln-Si-C-N, M-Si-Al-O-N (M = alkaline earth ion, Ln = lanthanide ion).[13-14]

In this thesis, I focus on Eu^{2+} and Ce^{3+} doped M-Si-Al-O-N (M = La, Sr) system phosphors, as the optical properties of Eu^{2+} and Ce^{3+} ions are strongly affected by the surrounding environment. Longer excitation and emission wavelengths can be expected compared to oxide-based phosphors, due to crystal-field splitting and nephelauxetic effect. Furthermore, the Stokes shift of phosphors becomes smaller in a rigid lattice with a more extended network of SiX_4 (X = O, N) tetrahedra.

1.3 Theory of luminescence

1.3.1 Effects of centroid shift, crystal field splitting and Stokes shift

The optical properties of Eu^{2+} and Ce^{3+} activated phosphors strongly depend on the local environments of the activator ion, as discussed in section 1.2.1. When an activator ion is placed in a host crystal, the electronic energy levels of the activator differ greatly from those of a free ion in vacuum. Three major effects determine the photoluminescence properties: the centroid shift, the crystal field splitting and the Stokes shift, as shown in Figure 1.2.

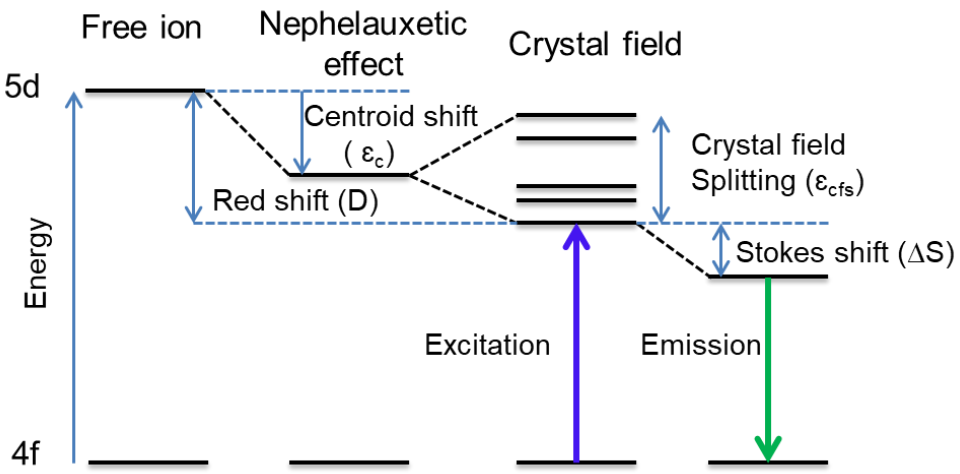

Figure 1.2 A diagram of the effects of centroid shift, crystal field splitting and Stokes shift on lowering of the energy of the 5d levels for Eu^{2+} or Ce^{3+} ion in a compound.

The centroid shift (ε_c)[15] is the lowered average energy of the 5d levels of the activator ion in a compound compared to that of the corresponding gaseous ions, due to a decrease in the inter-electron repulsion (nephelauxetic effect). The nephelauxetic effect is usually ascribed to the covalency of the bonds between activators and coordinating anions. With the increase of the covalency, the nephelauxetic effect thus becomes stronger. In addition, the increase of the polarizability of the surrounding anion ligands can also reduce the energy of the 5d level.[15] Considering N^{3-} has a lower electronegativity and higher spectroscopic polarizability than O^{2-}, a larger centroid shift is expected for nitride compounds compared to oxide compounds.

The crystal field splitting (ε_{cfs})[16] refers to the difference in energy between the highest and lowest 5d levels. The strength of the crystal field splitting is related to the bond lengths from the activator ion to the coordinating anions, the degree of covalency between the activator ion and its ligands, the coordination environment, and the symmetry of the activator site.[4] With decreasing the bond length or polyhedral volume, the crystal field splitting effect becomes stronger.[17] Dorenbos[16] found that the crystal field splitting tends to be largest for octahedral coordination, followed by cubic coordination and dodecahedral coordination, and smallest for tricapped trigonal prisms and cuboctahedral coordination. As illustrated in Figure 1.2, two major effects of the centroid shift and crystal field splitting lead to lowering of the $5d^1$ level by an amount that is named the redshift D. Obviously, the value of D determines the color of emission and wavelength of the 4f-5d absorption.

The Stokes shift is another effect of the host crystal on the energy of the activator ion, which is related to the ease of the relaxation of the excited ion in the lattice.[18] It determines the difference in energy between excitation and emission. A large Stokes shift reduces the emission intensity, because once an electron is excited to the 5d level, the surrounding lattice relaxes to new equilibrium positions due to coupling of the 5d electron with phonons.[4] This relaxation to a new equilibrium position leads to an effective lowering of the energy difference between the 5d and 4f levels in the excited states.[4] In general, a more rigid host lattice has a smaller Stokes shift.[19]

1.3.2 Effects of lanthanide energy level locations

The emission color, quantum efficiency and thermal stability of the emission are of crucial importance for phosphor performance in white LED applications. These three parameters of phosphor performance are related to the relative and absolute location of the lanthanide energy levels. For example, the absolute position of the 4f and 5d states relative to valence band and conduction band affects luminescence quenching and charge-trapping phenomena.[20] Dorenbos[21-22] has developed methods to position the lanthanide 4f and 5d levels, such as those of Eu^{2+} or Ce^{3+}, with respect to the valence and conduction band in inorganic compounds. The methods are based on four semi-empirical models (the redshift model,[23-24] the charge transfer model,[25] the centroid shift model,[15] and the chemical shift model[26]). With these models, one is able to use the optical properties of a certain lanthanide in a compound, to predict and explain luminescence properties of other divalent and trivalent lanthanide dopants in the same compound. The models have been successfully applied in many halide, chalcogenide and nitride compounds.

1.3.3 Theoretical models to predict lanthanide level locations

(1) The redshift model

The redshift D(Q,A)[23-24] is defined as the lowering of the 4f-$5d_1$ transition energy difference $E_{fd}(n,Q,A)$for a lanthanide ion with ionic charge Q in a compound A, as compared to that difference $E_{fd}(n,Q,free)$ for the lanthanide ion as a free ion in vacuum, where n is the number of electrons in the 4f-shell. The model states that the redshift is the same for each lanthanide ion, i.e., independent on n when on the same site of the same host compound.[22] So once $E_{fd}(n,Q,A)$ is known for one lanthanide ion, then it can be predicted all other lanthanide ions using[22]

$$E_{fd}(n,Q,A) = E_{fd}(n,Q,free) - D(Q,A) \quad (1)$$

here $E_{fd}(n,Q,free)$ is the 4f-5d_1 transition energy for the free lanthanide ions in vacuum as derived by Dorenbos[22] listed in Table 1.1. The energy of the 4f-5d_1 transition for each divalent and trivalent lanthanide ion in a compound can be predicted from such equations:

$$E_{fd}(n,2+,A) = E_{fd}(n,2+,free) - D(2+,A) \quad (2)$$

$$E_{fd}(n,3+,A) = E_{fd}(n,3+,free) - D(3+,A) \quad (3)$$

In addition, a roughly linear relationship between the redshift of divalent lanthanides D(2+,A) and that of trivalent lanthanides D(3+,A) has been found.[18]

$$D(2+,A) = 0.64\ D(3+,A) - 0.233\ eV \quad (4)$$

Investigations also show a linear relationship between crystal field splitting, centroid shift, and Stokes shift.[18] The relationships help in predicting spectroscopic properties for Ce^{3+} from properties known for Eu^{2+} and vice versa. Provided that Eu^{2+} occupies the same site as Ce^{3+}, the charge compensating defect is located beyond the first anion coordination shell, and the lattice relaxation around Eu^{2+} is similar to that around Ce^{3+}, $D(Eu^{2+})$ can be predicated with a standard deviation of about ±0.12 eV from Ce^{3+} data.[18] $D(Ce^{3+})$ can be predicated with about ±0.2 eV accuracy from Eu^{2+} data. It is concluded that the crystal field splitting in Eu^{2+} usually is 0.77 times that of Ce^{3+}, but the centroid shift and Stokes shift is 0.61 times as large.[18]

Table 1.1 Parameter values (in eV) that define the 4f and 5d binding energy curves for the divalent and trivalent lanthanides in compounds.[22]

n	Ln	ΔE (n+1,7,2+)	E_{fd}(n+1,2+,free)	ΔE (n,6,3+)	$E_{fd}^{sa}(n,3+,free)$
0	La	5.61	-0.94	-	-
1	Ce	4.13	-0.35	5.24	6.12
2	Pr	2.87	1.56	3.39	7.63
3	Nd	2.43	1.93	1.9	8.92
4	Pm	2.34	1.96	1.46	9.24
5	Sm	1.25	3	1.27	9.34
6	Eu	0	4.22	0	10.5
7	Gd	4.56	-0.2	-1.34	11.8
8	Tb	3.21	1.19	3.57	7.78
9	Dy	2.27	2.17	2.15	9.25
10	Ho	2.4	2.25	1.05	10.1
11	Er	2.58	2.12	1.12	9.86
12	Tm	1.72	2.95	1.28	9.75
13	Yb	0.433	4.22	0.236	10.89
14	Lu	-		-1.02	12.26

(2) The charge transfer model (CT-model)

The charge transfer transition is the electron transfer from a neighboring anion ligand to the 4f-shell of a trivalent lanthanide ion, which appears as a typically 0.8 eV broad band in absorption and excitation spectra of the trivalent lanthanide.[27] The CT energy can therefore in first approximation provide the location of the divalent lanthanide ground state levels with respect to the top of valence band. The energy of this band shows very characteristic and systematic change with the number of 4f electrons n. It is found that the CT-band energy to a trivalent lanthanide is always a fixed amount of energy larger than to Eu^{3+} when in the same site of the same compound. Dorenbos[22] obtained the average energy differences $\Delta E(n+1,7,2+)$ (shown in column 3 of Table 1.1) by collecting the CT-band energy data in many different compounds. With the knowledge that $\Delta E(n+1,7,2+)$ is independent of the type of compound, once the CT-band energy for one lanthanide ion is known, then that of all others can be predicated based on the relationship[27]

$$E^{CT}(n,3+,A) = E^{CT}(6,3+,A) + \Delta E(n+1,7,2+) \qquad (5)$$

$E^{CT}(6,3+,A)$ values can be obtained from experimentally observed Eu^{3+} CT-band energies or derived from the CT-band energies observed for other lanthanides.

(3) The centroid shift model

When the wave functions of the five 5d-orbital are added, a spherically symmetric electron distribution function is obtained centered at the nucleus of the lanthanide. The centroid shift therefore reflects the interaction of such charge distribution with its chemical environment, which is related to the covalency between anion ligands and 5d-ligands and the polarizability of the anions in the first coordination sphere around the lanthanide.[15] Since the redshift is a combination of the crystal field splitting and the centroid shift of the 5d-energy levels, as discussed before, which is similar for all trivalent lanthanides, the focus has been entirely on Ce^{3+} ion that has the most simple electron configuration ($4f^1$). The crystal field splitting depends on the size and the shape of the first anion coordination polyhedron around Ce^{3+}. The centroid shift $\varepsilon_{c(Ce^{3+},\ A)}$ is defined as the energy shift of the average 4f-5d$_i$ (i = 1-5) transition energy in a compound A as compared to the value of 6.35 eV for Ce^{3+} as a free ion in vacuum.[22]

$$\varepsilon_{c(Ce^{3+},\ A)} = 6.35 - \frac{1}{5}\sum_{i=1}^{5} E_{4f-5d_i}\ (Ce^{3+},\ A) \qquad (6)$$

(4) The chemical shift model

The chemical shift[26] is defined as the lowered energy of the 4f-electron binding energy of lanthanide ions in compounds compared to that in vacuum. Dorenbos[28] demonstrated that the chemical environment that causes the chemical shift and that determines the Coulomb repulsion energy U(Eu,A) for Eu affects the centroid shift for Ce^{3+} in a similar fashion. An empirical relationship was found[22]

$$U(Eu,A) = 5.44 + 2.834\, e^{-\varepsilon_{c(Ce^{3+},\ A)}/2.2} \quad (7)$$

Here the Coulomb repulsion energy is defined as

$$U(Eu,A) = E_{4f}(Eu^{2+},A) - E_{4f}(Eu^{3+}, A) \quad (8)$$

For many compounds the value for $\varepsilon_{c(Ce^{3+},\ A)}$ can be determined much more accurately with standard error ±0.05 eV than the value for U(Eu,A) (typically ±0.2 eV).[22] U(Eu,A) is found to be about 7.6 to 7.3 eV in poorly polarizable fluoride compounds, 7.3 to 6.5 eV in oxide compound, 6.3 to 6.1 eV in sulfide compound, and 6.5 to 6.0 eV in nitride compound.[21]

1.3.4 Methods to construct lanthanide energy level scheme

In order to construct the energy level scheme that displays the 4f and 5d energy level locations of trivalent and divalent lanthanide ions in a compound with respect to the valence band or the conduction band, three host-dependent parameters are necessary. (1) the band gap E_{VC} that refers to the energy difference between the top of valence band and the bottom of conduction band; (2) CT-band energy $E^{CT}(6, 3+, A)$; (3) redshift D(2+, A) or D(3+, A)

(1) Band gap E_{VC}

The optical band gap is usually derived from excitation, absorption and reflectance spectra, and the energy E^{ex} [22] stands for the energy needed to create a host exciton, that is to say an electron in the conduction band that is still bonded to a hole in the valence band. Therefore, an estimated value for the electron-hole binding energy is needed to obtain the energy at the bottom of the conduction band (the mobility edge). As a rule of thumb, the electron-hole binding energy is assumed 8% of E^{ex}.[29] In the energy level scheme, the experimental value E^{ex} at low temperature (10 K) is usually used, or otherwise a value 0.1-0.2 eV larger than the experimental value at room temperature.[22] The energy E_{VC} can therefore be estimated with this relationship:[22]

$$E_{VC} = 1.08\, E^{ex} \quad (9)$$

By using the energy E_{VC}, the distance between the top of valence band and the bottom of conduction band can be fixed.

(2) Locations of 4f states for Ln^{2+} and Ln^{3+} ions

$E^{CT}(6,3+,A)$ values can be obtained from experimentally observed Eu^{3+} CT-band energies or derived from the CT-band energies observed for other lanthanides by using equation 5, as discussed in CT-model section. For example, Eu in nitride and sulfide compounds is often hard or impossible to stabilize as trivalent impurity. In that case, the energy of CT-band can be derived from the more stable Yb^{3+} or Sm^{3+} dopant. By using the systematic energy difference $\Delta E(n+1, 7, 2+)$, the CT-band energy $E^{CT}(n, 3+, A)$ for all trivalent lanthanide ions can be certified with the aid of equation 5. Once $E^{CT}(n, 3+, A)$ values are known, the positions of 4f states for all divalent lanthanide ions (Ln^{2+}) relative to the top of the valence band can be determined. If the CT-band energy for Ln^{4+} is available, a similar method can be used to determine the locations of 4f states trivalent lanthanide ions. Otherwise by using the U(Eu,A) value derived from the centroid shift of Ce^{3+}, the energy of Eu^{3+} 4f state $E_{4f}(Eu^{3+},A)$ can be obtained. Once the $E_{4f}(Eu^{3+},A)$ is known, the positions of 4f states for all trivalent ions can be determined via the energy difference $\Delta E(n, 6, 3+)$.

(3) Locations of the lowest 5d states for Ln^{2+} and Ln^{3+} ions

The energy levels of the lowest 5d states for Ln^{2+} and Ln^{3+} ions with respected to the band gap can be positioned via either the redshift D (using equations 2, 3, 4) or thermal quenching data of the 5d-4f emission if the emission is quenched due to autoionization. So the energy difference between the relaxed lowest 5d state and the bottom of conduction band plays an important role in thermal quenching behavior.

The energy level scheme that can be constructed with a few parameters by using the methods above for all the lanthanide ions in a compound, provides a powerful tool to explain and predict the optical properties, such as 4f-5d and CT transition energies, quenching routes, valencies of lanthanide ions, and charge trapping depths.

1.4 State-of-the-art of nitride and oxynitride phosphors

Ce^{3+} and Eu^{2+}doped nitride and oxynitride phosphors have been found to have good chemical and thermal stability, high quantum efficiency and large flexibility in tuning the photoluminescence. Their structures are usually built up with highly condensed frameworks by corner or edge sharing $Si(N,O)_4$ or $Al(N,O)_4$ tetrahedrons, which give a high rigidity of structures.[13, 30] The structural variety can be further extended by incorporating other elements in the networks such as B, Li, Mg or Ga.[30-33]

Photoluminescence properties of Ce^{3+} and Eu^{2+} are very dependent on local structures due to nephelauxetic effect and crystal field splitting. The photoluminescence spectra can therefore be flexibly tailored by varying structures.

Some nitride and oxynitride phosphors have shown very promising properties for application as conversion phosphors for pc-wLEDs, among them are the (1) blue-emitting phosphors: $LaSi_3N_5$:Ce,[34] $LaAl(Si_{6-z}Al_z)(N_{10-z}O_z)$:Ce,[35] $BaSi_3Al_3O_4N_5$:Eu,[36] and Ca-α-sialon:Ce ($Ca_{m/2}Si_{12-(m+n)}Al_{m+n}O_nN_{16-n}$:Ce);[37] (2) green-emitting phosphors: β-sialon:Eu ($Si_{6-z}Al_zO_zN_{8-z}$:Eu),[38] $SrSi_2O_2N_2$:Eu,[39] and $Ba_2LiSi_7AlN_{12}$:Eu;[40] (3) red-emitting phosphors: $Sr_2Si_5N_8$:Eu,[41] $CaAlSiN_3$:Eu,[42] and $Sr(LiAl_3N_4)$:Eu.[30] Several of these phosphors have already been commercially applied for white LEDs such as the β-sialon:Eu,[38] $SrSi_2O_2N_2$:Eu,[39] $Sr_2Si_5N_8$:Eu,[41] and $CaAlSiN_3$:Eu[42] phosphors. Recently, new methods have been developed in order to find new phosphors, such as the single particles diagnosis approach[43-44] and heuristics-assisted combinatorial chemistry.[45] With the single particle diagnosis approach, several phosphors with new crystal structures such as $Ba_5Si_{11}Al_7N_{25}$:Eu,[43] $BaSi_4Al_3N_9$:Eu,[43] $Ba_2LiSi_7AlN_{12}$:Eu,[40] $Sr_2B_{2-2x}Si_{2+3x}Al_{2-x}N_{8+x}$:Eu,[31] $Sr_3Si_{8-x}Al_xO_{7+x}N_{8-x}$:Eu,[46] and $Ca_{1.62}Eu_{0.38}Si_5O_3N_6$[47] have been discovered. The phosphors $Ca_{15}Si_{20}N_{30}O_{10}$:Eu,[48] $Ba(Si,Al)_5(O,N)_8$:Eu[49] and $La_{4-x}Ca_xSi_{24}O_{3+x}N_{18-x}$:Eu[45] have recently been discovered via the heuristics-assisted combinatorial chemistry method.

However, despite the promising properties of these phosphors in terms of luminescence efficiency and emission wavelength, several challenges still remain. One of them is the thermal degradation that the phosphors undergo when subject to higher temperatures for longer time. In addition there is also still a lack of highly efficient deep blue emitting phosphors.

1.5 Scope and overview of this thesis

Phosphor-converted white light-emitting diodes (pc-wLEDs) have become the most preferred way to generate white light in general lighting compared to multi-LED approach, owing to the lower cost, higher color rendering and great potential to get higher luminous efficacy.[6] Due to the lack of a red light component, the low color rendering for most commercially available single-phosphor pc-wLEDs (a blue LED + a yellow-emitting YAG:Ce phosphor) prevents further application in illumination-grade lighting. A novel type of pc-wLED, consisting of a combination of a UV or near-UV LED chip and multiple phosphors, can reach a higher color rendering. However, highly efficient UV or near-UV excitable phosphors with good thermal stability are still lacking, especially for deep blue-emitting (410-450 nm emission) phosphors. In this thesis, I focus on developing novel UV or near-UV excitable oxynitride

phosphors for white LEDs. The synthesis, structure and photoluminescence properties of lanthanide doped M-SiAlON (M = La, Sr) phosphors are investigated. This thesis is composed of seven chapters. Chapter 1 is about general introduction of white LED, theory of luminescence and scope of thesis. In chapter 2, a brief description is given about the synthesis method and characterization techniques involving in structures and photoluminescence properties. The most important conclusions are summarized in Chapter 7, and an outlook on the potential of the UV excitable sialon phosphors for white LED application is given as well. The main research work consists of three parts, which is described from chapter 3 to chapter 6.

The first part is covered in chapter 3 and chapter 4, and is an investigation of the synthesis and photoluminescence properties of lanthanide doped $LaAl(Si_{6-z}Al_z)(N_{10-z}O_z)$ (termed JEM, $z \approx 1$) phosphors. Chapters 3 studies the synthesis and photoluminescence properties of Eu doped JEM phosphor. The effects of sintering temperature and chemical composition of starting materials (z value, N/O ratio and Si/Al ratio) on phase formation are investigated in order to get phase pure JEM:Eu samples. With the phase pure JEM:Eu samples obtained, the photoluminescence spectra, thermal quenching, quantum efficiency, red-shift of emission by varying Eu concentration and luminescence decay are further studied in order to evaluate the performance of JEM:Eu phosphors for white LED application. Chapter 4 further investigates the z value effect on phase purity of JEM:Ce phosphors and the photoluminescence properties including thermal quenching, quantum efficiency and luminescence decay behavior in order to make a comparison with JEM:Eu phosphors. The quantum efficiency and thermal stability of JEM:Ce phosphors are better than those of JEM:Eu phosphors. JEM:Ce phosphor shows a single luminescence decay behavior instead of bi-exponential decay for JEM:Eu phosphor, the reason of which is discussed. In addition to JEM:Ce phosphor, the photoluminescence properties of JEM:Yb and JEM:Sm phosphors are also studied. In order to explain their optical properties in terms of charge transfer transitions and dopant valencies, an energy level scheme is constructed by relating the optical properties of the Ce, Eu, Yb and Sm doped JEM phosphors with each other. The scheme shows the positions of the 4f and 5d levels of all divalent and trivalent lanthanide ions with respect to the valence and conduction bands, and allows the explanation and prediction of the photoluminescence properties of lanthanide ions doped JEM phosphors. It is shown that the experimental values agree well with the corresponding predicated values from the constructed energy level scheme by taking systematic errors into account.

The second part of the research work described in this thesis is on Ce doped Al-containing La N(ew)-phase $La_3Si_{8-x}Al_xN_{11-x}O_{4+x}$ (x = 1.5) phosphor, and is described in the chapter 5. Its photoluminescence properties and application for white LEDs are investigated. In order to compare with $La_3Si_8N_{11}O_4$, the effect of Al-O substitution on local structures is studied by measuring ^{29}Si and ^{27}Al NMR for non-doped $La_3Si_{6.5}Al_{1.5}N_{9.5}O_{5.5}$ sample. The effects of Ce concentration and Al-O substitution on photoluminescence spectra, quantum efficiency, and thermal quenching are also investigated. It is found that $La_3Si_{6.5}Al_{1.5}N_{9.5}O_{5.5}$:Ce phosphor is a highly efficient deep blue-emitting phosphor after UV or near-UV excitation. Compared to $La_3Si_8O_4N_{11}$:Ce phosphor, the quantum efficiency and thermal stability have been enhanced for $La_3Si_{6.5}Al_{1.5}N_{9.5}O_{5.5}$:Ce phosphor. In order to explain these improvements, temperature dependency of luminescence decay is measured for Ce doped without Al and Al-containing samples, the band gap of both non-doped samples is also checked. A very high color rendering (Ra = 93.2, R9 = 91.4, R12 = 89.5) white LED is made by using $La_3Si_{6.5}Al_{1.5}N_{9.5}O_{5.5}$:0.05Ce phosphor as the blue phosphor, showing the great potential of the phosphor for white LEDs.

The last part is about the discovery of a new Sr-sialon phase $Sr_{3.6}Si_{16.2}Al_{5.4}O_{3.6}N_{27}$ and the photoluminescence properties after doping with Eu and Ce, and is described in chapter 6 of this thesis. The photoluminescence properties of Eu and Ce doped the new Sr-sialon phosphors including photoluminescence spectra, thermal quenching, quantum efficiency and luminescence decay are investigated in order to evaluate their potential for white LED application.

1.6 References

(1) Kim, J. K.; Schubert, E. F. Transcending the Replacement Paradigm of Solid-State Lighting *Optics Express* **2008**, *16*, 21835-21842.

(2) McKittrick, J.; Shea‐Rohwer, L. E. Review: Down Conversion Materials for Solid-State Lighting *Journal of the American Ceramic Society* **2014**, *97*, 1327-1352.

(3) Pimputkar, S.; Speck, J. S.; DenBaars, S. P.; Nakamura, S. Prospects for LED Lighting *Nature Photonics* **2009**, *3*, 180-182.

(4) George, N. C.; Denault, K. A.; Seshadri, R. Phosphors for Solid-State White Lighting *Annual Review of Materials Research* **2013**, *43*, 481-501.

(5) Smet, P. F.; Parmentier, A. B.; Poelman, D. Selecting Conversion Phosphors for White Light-Emitting Diodes *Journal of the Electrochemical Society* **2011**, *158*, R37-R54.

(6) Bardsley, N.; Bland, S.; Hansen, M.; Pattison, L.; Pattison, M.; Stober, K.; Yamada, M. *Solid-State Lighting R&D Plan-2015*, EERE Publication and Product Library, 2015.

(7) Yamamoto, H. *Fundamentals of Luminescence*; CRC Press, New York, **2007**.

(8) Dorenbos, P. Anomalous Luminescence of Eu^{2+} and Yb^{2+} in Inorganic Compounds *Journal of Physics: Condensed Matter* **2003**, *15*, 2645.

(9) Lizzo, S.; Meijerink, A.; Blasse, G. Luminescence of Divalent Ytterbium in Alkaline Earth Sulphates *Journal of Luminescence* **1994**, *59*, 185-194.

(10) McKittrick, J.; Hannah, M.; Piquette, A.; Han, J.; Choi, J.; Anc, M.; Galvez, M.; Lugauer, H.; Talbot, J.; Mishra, K. Phosphor Selection Considerations for near-UV LED Solid State Lighting *ECS Journal of Solid State Science and Technology* **2013**, *2*, R3119-R3131.

(11) Piquette, A.; Bergbauer, W.; Galler, B.; Mishra, K. On Choosing Phosphors for near-Uv and Blue LEDs for White Light *Ecs Journal of Solid State Science and Technology* **2016**, *5*, R3146-R3159.

(12) Liu, W.-R.; Lin, C. C.; Chiu, Y.-C.; Yeh, Y.-T.; Jang, S.-M.; Liu, R.-S. $ZnB_2O_4:Bi^{3+},Eu^{3+}$: A Highly Efficient, Red-Emitting Phosphor *Optics Express* **2010**, *18*, 2946-2951.

(13) Xie, R.-J.; Hirosaki, N. Silicon-Based Oxynitride and Nitride Phosphors for White LEDs—a Review *Science and Technology of Advanced Materials* **2007**, *8*, 588-600.

(14) Li, Y. Q. *Structure and Luminescence Properties of Novel Rare-Earth Doped Silicon Nitride Based Materials*; Technische Universiteit Eindhoven, **2005**.

(15) Dorenbos, P. Relating the Energy of the $[Xe]5d_1$ Configuration of Ce^{3+} in Inorganic Compounds with Anion Polarizability and Cation Electronegativity *Physical Review B* **2002**, *65*, 235110.

(16) Dorenbos, P. Crystal Field Splitting of Lanthanide $4f^{n-1}5d$-Levels in Inorganic Compounds *Journal of Alloys and Compounds* **2002**, *341*, 156-159.

(17) Rack, P. D.; Holloway, P. H. The Structure, Device Physics, and Material Properties of Thin Film Electroluminescent Displays *Materials Science and Engineering: R: Reports* **1998**, *21*, 171-219.

(18) Dorenbos, P. Relation between Eu^{2+} and Ce^{3+} f↔ d-Transition Energies in Inorganic Compounds *Journal of Physics: Condensed Matter* **2003**, *15*, 4797.

(19) Verwey, J.; Blasse, G. The Luminescence Efficiency of Ions with Broad-Band Excitation in Borate Glasses *Materials Chemistry and Physics* **1990**, *25*, 91-103.

(20) Tanimizu, S.; Shionoya, S.; Yen, W.; Yamamoto, H. *Principal Phosphor Materials and Their Optical Properties*; Boca Raton, FL: CRC Press, **1999**.

(21) Dorenbos, P. Determining Binding Energies of Valence-Band Electrons in Insulators and Semiconductors Via Lanthanide Spectroscopy *Physical Review B* **2013**, *87*, 035118.

(22) Dorenbos, P. Ce^{3+} 5d-Centroid Shift and Vacuum Referred 4f-Electron Binding Energies of All Lanthanide Impurities in 150 Different Compounds *Journal of Luminescence* **2013**, *135*, 93-104.

(23) Dorenbos, P. The $4f^n \leftrightarrow 4f^{n-1}5d$ Transitions of the Trivalent Lanthanides in Halogenides and Chalcogenides *Journal of Luminescence* **2000**, *91*, 91-106.

(24) Dorenbos, P. f→ d Transition Energies of Divalent Lanthanides in Inorganic Compounds *Journal of Physics: Condensed Matter* **2003**, *15*, 575.

(25) Dorenbos, P. Systematic Behaviour in Trivalent Lanthanide Charge Transfer Energies *Journal of Physics: Condensed Matter* **2003**, *15*, 8417.

(26) Dorenbos, P. Modeling the Chemical Shift of Lanthanide 4f Electron Binding Energies *Physical Review B* **2012**, *85*, 165107.

(27) Dorenbos, P. A Review on How Lanthanide Impurity Levels Change with Chemistry and Structure of Inorganic Compounds *ECS Journal of Solid State Science and Technology* **2013**, *2*, R3001-R3011.

(28) Dorenbos, P. Lanthanide 4f-Electron Binding Energies and the Nephelauxetic Effect in Wide Band Gap Compounds *Journal of Luminescence* **2013**, *136*, 122-129.

(29) Dorenbos, P. The Eu^{3+} Charge Transfer Energy and the Relation with the Band Gap of Compounds *Journal of Luminescence* **2005**, *111*, 89-104.

(30) Pust, P.; Weiler, V.; Hecht, C.; Tücks, A.; Wochnik, A. S.; Henß, A.-K.; Wiechert, D.; Scheu, C.; Schmidt, P. J.; Schnick, W. Narrow-Band Red-Emitting $Sr[LiAl_3N_4]:Eu^{2+}$ as a Next-Generation LED-Phosphor Material *Nature Materials* **2014**, *13*, 891-896.

(31) ten Kate, O. M.; Xie, R.-J.; Wang, C.-Y.; Funahashi, S.; Hirosaki, N. Eu^{2+}-Doped $Sr_2B_{2-2x}Si_{2+3x}Al_{2-x}N_{8+x}$: A Boron-Containing Orange-Emitting Nitridosilicate with Interesting Composition-Dependent Photoluminescence Properties *Inorganic Chemistry* **2016**, *55*, 11331-11336.

(32) Pust, P.; Hintze, F.; Hecht, C.; Weiler, V.; Locher, A.; Zitnanska, D.; Harm, S.; Wiechert, D.; Schmidt, P. J.; Schnick, W. Group (III) Nitrides M $[Mg_2Al_2N_4]$(M= Ca, Sr, Ba, Eu) and Ba $[Mg_2Ga_2N_4]$ − Structural Relation and Nontypical Luminescence Properties of Eu^{2+} Doped Samples *Chemistry of Materials* **2014**, *26*, 6113-6119.

(33) Hintze, F.; Johnson, N. W.; Seibald, M.; Muir, D.; Moewes, A.; Schnick, W. Magnesium Double Nitride Mg_3GaN_3 as New Host Lattice for Eu^{2+} Doping: Synthesis, Structural Studies, Luminescence, and Band-Gap Determination *Chemistry of Materials* **2013**, *25*, 4044-4052.

(34) Suehiro, T.; Hirosaki, N.; Xie, R.-J.; Sato, T. Blue-Emitting $LaSi_3N_5:Ce^{3+}$ Fine Powder Phosphor for UV-Converting White Light-Emitting Diodes *Applied Physics Letters* **2009**, *95*, 051903.

(35) Takahashi, K.; Hirosaki, N.; Xie, R.-J.; Harada, M.; Yoshimura, K.-i.; Tomomura, Y. Luminescence Properties of Blue $La_{1-x}Ce_xAl_z(Si_{6-z}Al_z)(N_{10-z}O_z)$ ($z \sim 1$) Oxynitride Phosphors and Their Application in White Light-Emitting Diode *Applied Physics Letters* **2007**, *91*, 091923.

(36) Tang, J.-Y.; Xie, W.-J.; Huang, K.; Hao, L.-Y.; Xu, X.; Xie, R.-J. A High Stable Blue $BaSi_3Al_3O_4N_5:Eu^{2+}$ Phosphor for White Leds and Display Applications *Electrochemical and Solid-State Letters* **2011**, *14*, J45-J47.

(37) Xie, R. J.; Hirosaki, N.; Mitomo, M.; Yamamoto, Y.; Suehiro, T.; Ohashi, N. Photoluminescence of Cerium-Doped α-Sialon Materials *Journal of the American Ceramic Society* **2004**, *87*, 1368-1370.

(38) Hirosaki, N.; Xie, R.-J.; Kimoto, K.; Sekiguchi, T.; Yamamoto, Y.; Suehiro, T.; Mitomo, M. Characterization and Properties of Green-Emitting β-Sialon:Eu^{2+} Powder Phosphors for White Light-Emitting Diodes *Applied Physics Letters* **2005**, *86*, 211905-211905.

(39) Li, Y.; Delsing, A.; De With, G.; Hintzen, H. Luminescence Properties of Eu^{2+}-Activated Alkaline-Earth Silicon-Oxynitride $MSi_2O_{2-\delta}N_{2+2/3\delta}$ (M= Ca, Sr, Ba): A Promising Class of Novel Led Conversion Phosphors *Chemistry of Materials* **2005**, *17*, 3242-3248.

(40) Takeda, T.; Hirosaki, N.; Funahshi, S.; Xie, R.-J. Narrow-Band Green-Emitting Phosphor $Ba_2LiSi_7AlN_{12}:Eu^{2+}$ with High Thermal Stability Discovered by a Single Particle Diagnosis Approach *Chemistry of Materials* **2015**, *27*, 5892-5898.

(41) Höppe, H.; Lutz, H.; Morys, P.; Schnick, W.; Seilmeier, A. Luminescence in Eu^{2+}-Doped $Ba_2Si_5N_8$: Fluorescence, Thermoluminescence, and Upconversion *Journal of Physics and Chemistry of Solids* **2000**, *61*, 2001-2006.

(42) Uheda, K.; Hirosaki, N.; Yamamoto, Y.; Naito, A.; Nakajima, T.; Yamamoto, H. Luminescence Properties of a Red Phosphor, $CaAlSiN_3:Eu^{2+}$, for White Light-Emitting Diodes *Electrochemical and Solid-State Letters* **2006**, *9*, H22-H25.

(43) Hirosaki, N.; Takeda, T.; Funahashi, S.; Xie, R.-J. Discovery of New Nitridosilicate Phosphors for Solid State Lighting by the Single-Particle-Diagnosis Approach *Chemistry of Materials* **2014**, *26*, 4280-4288.

(44) Takeda, T.; Hirosaki, N.; Funahashi, S.; Xie, R.-J. New Phosphor Discovery by the Single Particle Diagnosis Approach *Materials Discovery* **2015**, *1*, 29-37.

(45) Park, W. B.; Shin, N.; Hong, K. P.; Pyo, M.; Sohn, K. S. A New Paradigm for Materials Discovery: Heuristics‐Assisted Combinatorial Chemistry Involving Parameterization of Material Novelty *Advanced Functional Materials* **2012**, *22*, 2258-2266.

(46) Wang, X.-J.; Wang, L.; Takeda, T.; Funahashi, S.; Suehiro, T.; Hirosaki, N.; Xie, R.-J. Blue-Emitting $Sr_3Si_{8-x}Al_xO_{7+x}N_{8-x}:Eu^{2+}$ Discovered by a Single-Particle-Diagnosis Approach: Crystal Structure, Luminescence, Scale-up Synthesis, and Its Abnormal Thermal Quenching Behavior *Chemistry of Materials* **2015**, *27*, 7689-7697.

(47) Wang, X.-J.; Funahashi, S.; Takeda, T.; Suehiro, T.; Hirosaki, N.; Xie, R.-J. Structure and Luminescence of a Novel Orange-Yellow-Emitting $Ca_{1.62}Eu_{0.38}Si_5O_3N_6$ Phosphor for Warm White Leds, Discovered by a Single-Particle-Diagnosis Approach *Journal of Materials Chemistry C* **2016**, *4*, 9968-9975.

(48) Park, W. B.; Singh, S. P.; Yoon, C.; Sohn, K.-S. Eu^{2+} Luminescence from 5 Different Crystallographic Sites in a Novel Red Phosphor, $Ca_{15}Si_{20}O_{10}N_{30}:Eu^{2+}$ *Journal of Materials Chemistry* **2012**, *22*, 14068-14075.

(49) Park, W. B.; Singh, S. P.; Sohn, K.-S. Discovery of a Phosphor for Light Emitting Diode Applications and Its Structural Determination, $Ba(Si,Al)_5(O,N)_8:Eu^{2+}$ *Journal of the American Chemical Society* **2014**, *136*, 2363-2373.

Chapter 2 Experimental

In this chapter the methods and techniques are discussed that have been used for my PhD work. The synthesis method of the powder samples is discussed in section 2.1, the structural characterization techniques (XRD, NMR and SEM-EDS) are discussed in section 2.2, and the different photoluminescence characterization techniques are described in section 2.3.

2.1 Synthesis of powder samples with solid-state reaction method

All of the samples during my PhD research are synthesized by using solid state reaction method in a gas pressure furnace at high temperature (between 1700 and 1900 °C at 0.92 MPa), since the studied materials are all high-temperature sialon phases. The samples are mixed with the designed chemical composition and packed in boron nitride crucibles for firing. If the starting material is sensitive to oxygen and moisture, the mixing and packages have to be done in a glove box filled with highly pure nitrogen gas. After firing, the powder samples are cooled down automatically and finely ground with a mortar for further characterization of structure and photoluminescence properties. Taken JEM:Eu phosphor as an example, the process of synthesis can be briefly expressed as shown in Figure 2.1.

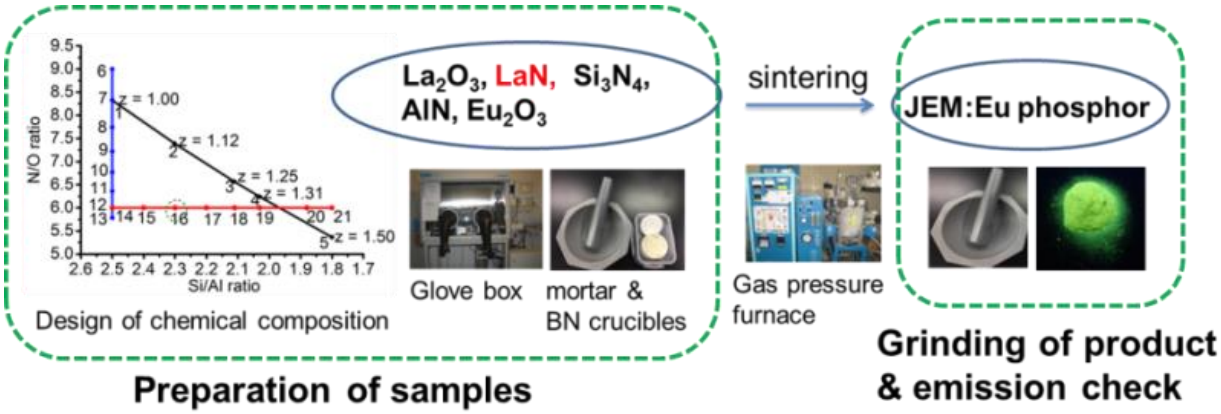

Figure 2.1 A schematic diagram of process to synthesize JEM:Eu phosphor.

2.2. Structural characterization

2.2.1 X-ray diffraction (XRD)

X-ray diffraction (XRD) is a basic analytical technique that measures the angles of diffraction of X-rays on a crystalline sample. It is used to analyze the crystal structure of materials, making use of

Bragg's law $2d_{hkl}*\sin\theta = n\lambda$, where n is the order of reflection or diffraction, d is the spacing between the crystal lattice plane (hkl), λ is the wavelength of the incident wave, and θ is the angle between the incoming X-ray and the crystal lattice plane.[1] The powder X-ray diffraction (PXRD) patterns are measured with a Smartlab from Rigaku by using Cu Kα1 radiation, and Bragg-Brentano diffractometers are used as shown in Figure 2.2.

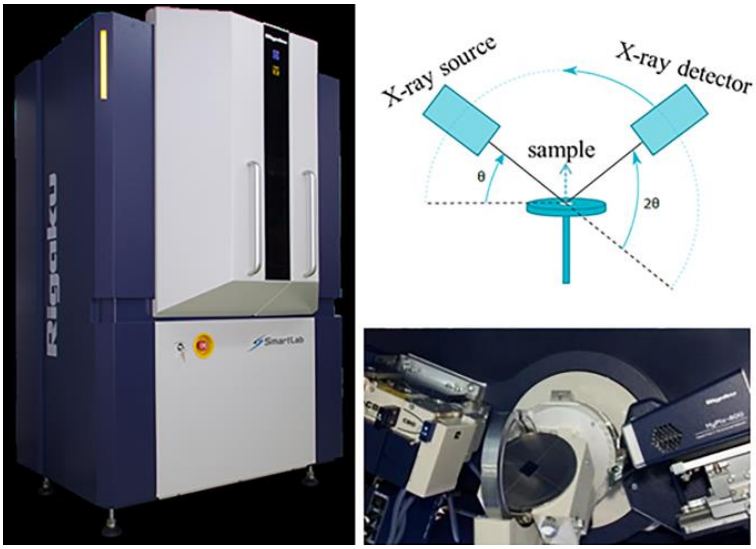

Figure 2.2 Smartlab XRD (left) used for PXRD measurement and a Bragg-Brentano diffractometer (right).

During the XRD measurement, the X-ray tube is fixed, the sample rotates at θ°/min and the detector rotates at 2θ°/min, as illustrated in Figure 2.2 (right). The work voltage is 40 kV and the current is 200 mA. By scanning the sample through a range of 2θ angles, all possible diffraction directions of the lattice can be obtained due to the random orientation of the powdered material. Conversion of the diffraction peaks to d-spacings allows identification of the crystalline phase presented in the sample, because each crystalline phase has a set of unique d-spacings.[1]

2.2.2 Solid-state nuclear magnetic resonance (NMR)

Solid-state NMR is a kind of NMR spectroscopy that makes use of the absorption of electromagnetic radiation in a magnetic field by certain isotopes at specific resonance frequencies.[2] The chemical environment influences the resonance frequency, resulting in a chemical shift, which is measured with NMR. Because the interactions are directionally dependent (anisotropic) in solid-state NMR, they are typically very broad as compared to liquid-state NMR in which the Brownian motion leads to averaging

of the anisotropic interactions. NMR is principally concerned with short-range, local order and is element specific, which can provide valuable information on the local coordination environment of atoms that have similar scattering factors (O and N, Si and Al) and can therefore not be distinguished using the XRD technique.[2] In this thesis, ^{29}Si and ^{27}Al NMR have been studied by using high-resolution solid-state magic angle spinning (MAS) NMR technique to get high resolution spectra and better identification. A solid sample is placed in a rotor and mechanically rotated at a high frequency about an axis oriented at the magic angle of θ_m = 54.74° (yielding $3\cos^2\theta_m$-1 =0) with respect to the static magnetic field B_0,[3] as shown in Figure 2.3. The ^{29}Si MAS NMR spectrum was collected with a JEOL RESONANCE ECA 500 spectrometer at a magnetic field of 11.75 T, as shown in Figure 2.3. A JEOL RESONANCE ECA 800 spectrometer is used to record the signal of ^{27}Al MAS NMR and the measurement was performed at a magnetic field of 18.79 T.

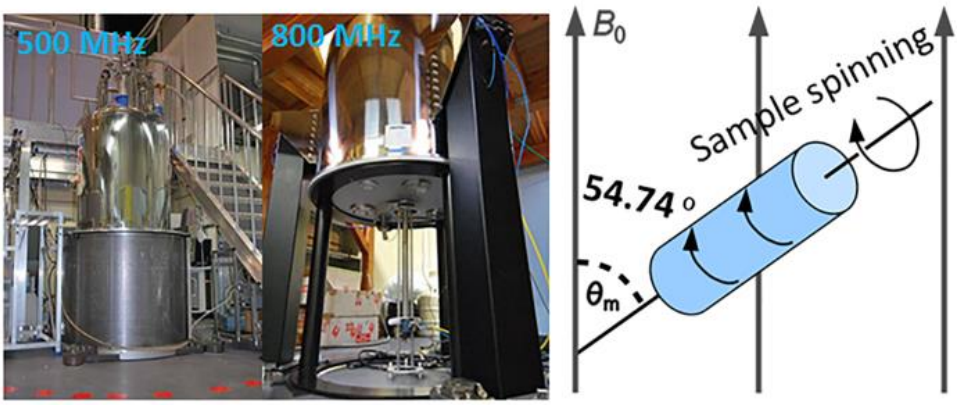

Figure 2.3 The solid-state NMR with 500 MHz and 800 MHz that are used for ^{29}Si and ^{27}Al high-resolution MAS NMR measurements, respectively, and a schematic diagram of the MAS technique.

The main three interactions (dipolar, chemical shift anisotropy and quadrupolar) in solids are orientation dependent and can be averaged by MAS. This orientation averaging causes the signal to become narrower, giving rise to the isotropic value and spinning sidebands that can be used to determine the chemical shift anisotropy of the nuclei.[2] For ^{27}Al NMR, a multiple quantum magic-angle spinning (MQ MAS) NMR is also used, which can provide a high resolution spectrum of half-integer spin quadrupolar nuclei. It is performed as a two-dimensional NMR experiment, and correlates a high resolution (isotropic) spectrum to the anisotropic central MAS spectrum.[4]

2.2.3 Scanning electron microscopy (SEM) and energy-dispersive X-ray spectroscopy (EDS)

A field emission scanning electron microscope (FE-SEM) S-4800 from Hitachi equipped with EDX (Horiba Emax) is used to get the information of the sample's topography and chemical composition, as presented in Figure 2.4 (left). The signals used to produce an image result from interactions of the electron beam with atoms at various depths within the sample, as shown in Figure 2.4 (middle). The secondary electrons (SE) are emitted from very close to the specimen surface. Therefore the signal of the SE is used to produce a high-resolution image of the topography of a sample surface, which can reveal details less than 1 nm in size.[5] Characteristic X-rays are emitted when the electron beam removes an inner shell electron from the sample, causing a higher-energy electron to fill the shell and release energy, as illustrated in Figure 2.4 (right). The number and energies of the X-rays emitted from a specimen can be measured by an energy-dispersive spectrometer. As the energies are characteristic of the energy difference between two shells and of the atomic structure of the emitting element, EDS is used to identify the composition and measure the abundance of elements in the sample.[5]

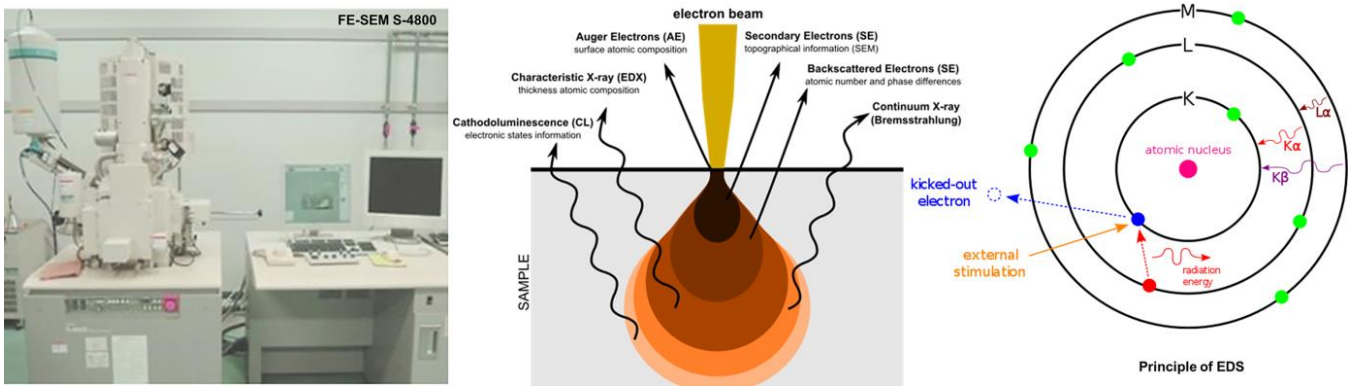

Figure 2.4 A field emission scanning electron microscope (FE-SEM) S-4800 from Hitachi equipped with EDX (left), signals emitted from different parts of the interaction volume (middle)[6] and principle of EDS (right).[7]

2.3 Photoluminescence properties characterization

2.3.1 Diffuse reflectance spectroscopy

A diffuse reflectance spectrum is measured to identify the color of powders, the absorption of light and estimate the optical band gap of the phosphor host. The diffuse reflectance measurement is performed with a V-560 UV/vis spectrophotometer from JASCO, in which a deuterium lamp (190 to 350 nm) is used for measuring in the ultraviolet light region and a halogen lamp (340 to 900 nm) is to measure in the visible light region. For diffuse reflectance spectroscopy, the backscattered signal is

detected and compared to the backscattered signal from a white reference material ($BaSO_4$) that has a reflectance of 100%. The reflectance R is then defined as the ratio of the amount light reflected from the sample over the amount of light reflected from the reference material. The diffuse reflectance spectrum of a non-doped sample can be used to estimate the optical band gap of the host through the transformation of Kubelka–Munk function[8]

$$f(R) = \frac{(1-R)^2}{2R} = \frac{K}{S}$$

where R is the absolute reflectance of a sampled layer, K is the molar absorption coefficient and S is the scattering coefficient. The optical band gap can be roughly estimated by taking the absorption edge.[9]

2.3.2 X-ray absorption near edge structure (XANES) spectroscopy

X-ray absorption near edge structure (XANES) is a technique that can be used to determine the valency of atoms in a material. During a XANES measurement the sample is irradiated with X-rays. The atoms in the material can absorb these X-rays, resulting in a lower transmission of the X-rays through the sample. The absorption of X-rays by an atom is strongest if the energy matches the binding energy of the electron, resulting in an absorption edge.[10] The energy of the absorption edge is dependent on the type of atom as well as its valency and therefore a way to detect the valency of the atoms in the material. In addition, the absorption edge is also sensitive for the coordination environment of the atom and can thus also give structural information.[10] For the work described in this thesis, XANES was used to determine the valencies of the lanthanides. The measurement was done with the BL-9C beamline from the Photon Factory (PF) synchrotron radiation facility from KEK.

2.3.3 Photoluminescence (PL) spectroscopy

Photoluminescence spectroscopy is used to determine the excitation wavelengths under which a phosphor emits light at a specific wavelength, and the emission intensity of a phosphor when excited at a fixed wavelength. A Hitachi F-4500 fluorescence spectrophotometer is used to record the PL spectra, which basically consists of a 150 W Xe lamp, excitation and emission monochromators that are used to select a specific wavelength from the incoming and emitted light, sample holders and a photodetector. A Xenon lamp is used as the light source because of its high intensity and steady state in a short time period. In addition, its light covers the entire UV and visible wavelength range, from 190nm to 1100nm.

The light from a Xe lamp passes through the excitation monochromator, and irradiates the sample in a sample cell. Partial incident light is absorbed by the sample. The emitted light from the sample passes through a second emission monochromator and is then recorded by a photodetector.[11] The photodetector transforms the photons into electrical signals, which are amplified and processed by a computer.

To measure an excitation spectrum, the emission intensity is recorded at a fixed emission wavelength as a function of the excitation wavelength. An excitation spectrum is used to determine the most efficient excitation wavelength for a phosphor and is related to the absorption spectrum of the phosphor. To measure an emission spectrum, the excitation wavelength is fixed and the emission intensity is measured as a function of the emission wavelength. Due to the Stokes shift, the emission wavelength is much longer than the chosen excitation wavelength.

2.3.4 Quantum efficiency (QE)

Quantum efficiency is one of the important parameters to evaluate the performance of a phosphor. The internal quantum efficiency (IQE) evaluates how much of the light (photons) absorbed by the phosphor is converted to luminescence. The external quantum efficiency (EQE) indicates the ratio of the number of photons from the light emitted by the phosphor compared to that from incident light. The IQE (η_i) and EQE (η_e) can be calculated by the equations as follows:[12]

$$\eta_i = \frac{\int \lambda P(\lambda) d\lambda}{\int \lambda [E(\lambda) - R(\lambda)] d\lambda}$$

$$\eta_e = \frac{\int \lambda P(\lambda) d\lambda}{\int \lambda \, E(\lambda) d\lambda}$$

where E(λ), R(λ) and P(λ) are the intensity per unit wavelength in the spectra of excitation, reflectance, and emission of the phosphor, respectively.

The measurement system for the quantum efficiency is shown in Figure 2.5. An integrating sphere is used to collect all emitted light. A multi-channel photo detector (MCPD) from Otsuka Electronics Company is used as a spectrometer to measure reflectance and emission spectrum.

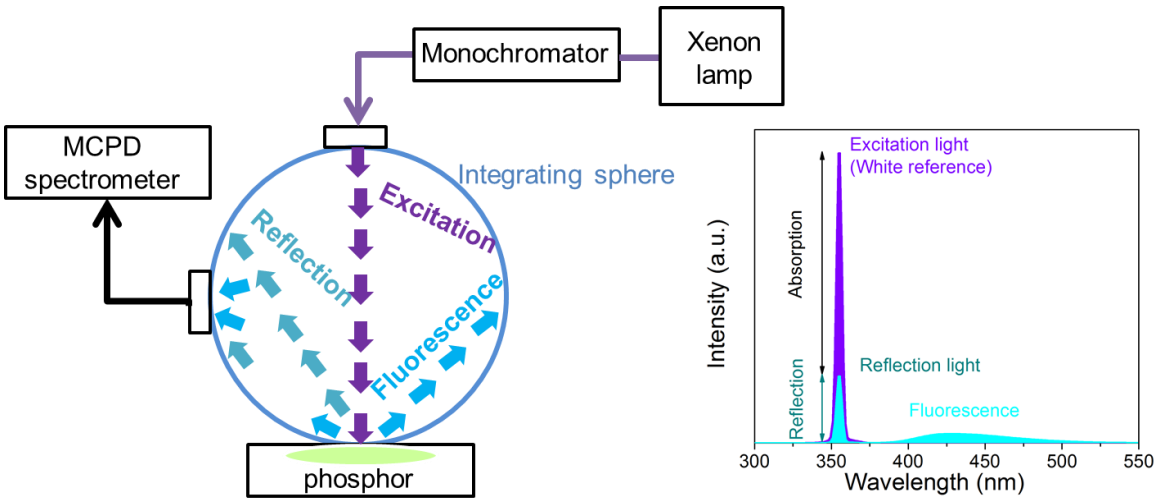

Figure 2.5 A schematic of the measurement system for quantum efficiency (left) and typical spectra obtained for a luminescent sample and a white reference sample (right).

2.3.5 Temperature dependent photoluminescence

High temperature dependent photoluminescence (thermal quenching) measurement is used to assess the thermal stability of phosphors from the application point of view for white LED. The properties of phosphors that are used should be stable up to the working temperatures of LEDs, especially for high power LEDs. The measurement system is similar to that for quantum efficiency measurement, and a heater and a temperature controller are added to adjust the temperature of the sample. The temperature can be increased up to 600 °C from room temperature.

Low temperature dependent photoluminescence spectra are used to more accurately identify different electronic and vibrational levels or distinguish different luminescence centers from different coordination environments. The sample is put in a vacuum chamber and can be cooled down from 298 K to 4 K by using a He cryostat (Oxford, OPTICOOL).

2.3.6 Time-resolved photoluminescence (TRPL) and time-resolved emission spectroscopy (TRES)

Time-resolved photoluminescence (TRPL) records the decay in photoluminescence with respect to time where the sample is excited with a light pulse. A nano LED from Horiba with 370 nm emission and 1.2 ns pulse duration is used as excitation source. The decay of the intensity as a function of time is given by $I_t = I_0 e^{-t/\tau}$, where I_0 is the intensity at time t = 0, t is the time after absorption and τ is the fluorescence lifetime.[13] The fluorescence lifetime is defined as the time at which the intensity has

decayed to 1/e (36.8%) of the original value.[13] Fluorescence lifetime is an intrinsic property of phosphors, which is related to the structure and it can give some interpretations of fluorescent phenomenon such as quenching and the presence of luminescent centers in different environments.[13-14] TRPL is measured by using a time-correlated single photon counting system (TCSPC) technique.

Time-resolved emission spectroscopy (TRES) is similar to TRPL but not just the intensity at a certain emission wavelength is monitored, but the entire emission spectrum can be obtained at different time intervals. In this way it can be checked whether there are differences in decay time between photons emitted at different wavelength. In this thesis TRES is used to check the presence and emission spectrum of luminescent centers in different crystallographic environments which have different decay times. In order to get time-resolved emission spectra, the wavelength dependent time resolved delays are required. By taking the slices of data in the wavelength (λ) – intensity (I) plane shown in Figure 2.6 with a fixed time interval, the emission spectra at different times (t) during the decay can be obtained.

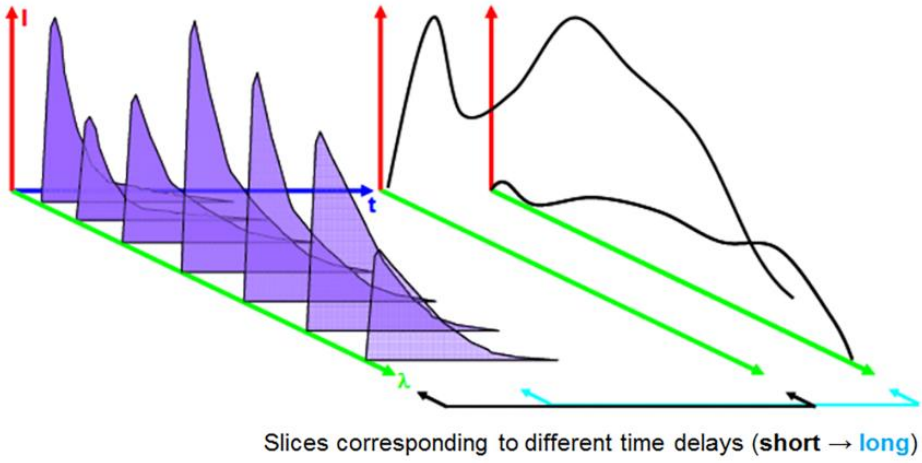

Figure 2.6 A Scheme showing spectra slices to give TRES.

2.4 References

(1) Suryanarayana, C.; Norton, M. G. *X-Ray Diffraction: A Practical Approach*; Springer Science & Business Media, **2013**.

(2) Bakhmutov, V. I. *Solid-State NMR in Materials Science: Principles and Applications*; CRC Press, 2011.

(3) Alia, A.; Ganapathy, S.; de Groot, H. J. Magic Angle Spinning (MAS) NMR: A New Tool to Study the Spatial and Electronic Structure of Photosynthetic Complexes *Photosynthesis research* **2009**, *102*, 415.

(4) Medek, A.; Frydman, L. Multiple-Quantum Magic-Angle Spinning NMR: A New Technique for Probing Quadrupolar Nuclei in Solids *Journal of the Brazilian Chemical Society* **1999**, *10*, 263-277.

(5) Lawes, G. Scanning Electron Microscopy and X-Ray Microanalysis **1987**.

(6) Commonswiki, C. **2013**, *Signals emitted from different parts of the interaction volume*, https://en.wikipedia.org/wiki/Scanning_electron_microscope.

(7) Muso, **2007**, *Principle of EDS*, https://en.wikipedia.org/wiki/Energy-dispersive_X-ray_spectroscopy.

(8) Torrent, J.; Barron, V. Diffuse Reflectance Spectroscopy *Methods of soil analysis. Part* **2008**, *5*, 367-387.

(9) Fox, M.; *Optical properties of solids*, AAPT: 2002.

(10) Koningsberger, D.; Prins, R. *X-Ray Absorption: Principles, Applications, Techniques of EXAFS, SEXAFS, and XANES*, John Wiley and Sons, **1988**.

(11) Xie, R.-J.; Li, Y. Q.; Hirosaki, N.; Yamamoto, H. *Nitride Phosphors and Solid-State Lighting*; CRC Press, **2011**.

(12) Kazuaki Ohkubo, T. S. Absolute Fluorescent Quantum Efficiency of Nbs Phosphor Standard Samples *Journal of the Illuminating Engineering Institute ofJapan*, **1999**, *83*, 87-93.

(13) Berezin, M. Y.; Achilefu, S. Fluorescence Lifetime Measurements and Biological Imaging *Chemical Reviews* **2010**, *110*, 2641-2684.

(14) Maiberg, M.; Scheer, R. Theoretical Study of Time-Resolved Luminescence in Semiconductors. I. Decay from the Steady State *Journal of Applied Physics* **2014**, *116*, 123710.

Chapter 3 Synthesis and photoluminescence properties of a phase pure green-emitting Eu doped JEM sialon ($LaSi_{6-z}Al_{1+z}N_{10-z}O_z$, z ~ 1) phosphor with a large red-shift of emission and unusual thermal quenching behavior

This chapter has been published as Chun-Yun Wang, Takashi Takeda, Otmar Melvin ten Kate, Rong-Jun Xie, Kohsei Takahashi and Naoto Hirosaki. Journal of Materials Chemistry C. 2016, 4, 10358 - 10366.

3.1 Introduction

$LaAl(Si_{6-z}Al_z)(N_{10-z}O_z)$ (termed as JEM, z ~ 1) was discovered as an intergranular phase in ceramic materials by Grins et al. in 1995 and the name was an acronym of the initial authors.[1-2] JEM has an orthorhombic structure with lattice parameters a = 9.4303 Å, b = 9.7689 Å, and c = 8.9386 Å in space group Pbcn. The Al atoms and (Si,Al) atoms are tetrahedrally coordinated by (N,O) atoms, yielding an $Al(Si,Al)_6(N,O)_{10}^{3-}$ network. The La atoms are located in the tunnels formed by the network extending along the [001] direction and are irregularly coordinated by seven (N,O) atoms at an average distance of 2.70 Å.[1] It was mainly studied as heat-resistant material until 2007 when Takahashi et al.[3] reported that Ce doped JEM phase phosphor can emit blue light with high quantum efficiency (internal quantum efficiency is around 62%) after 405 nm light excitation. Its emission spectra peak wavelength is widely tunable in a range of 460-500 nm, and high color rendering index (Ra = 95-96) has been obtained for the near-UV LED with various correlated color temperatures. Therefore, JEM:Ce^{3+} has been strongly suggested as a candidate for solid-state lighting, especially for home illumination. Afterwards, the photoluminescence properties of JEM:Ce^{3+} phosphor were enhanced by co-doping Ca.[4] However, a phase pure JEM phosphor has not yet been obtained, with some impure phases even coexisting inside the same particle.[5] In general, Eu^{2+} and Ce^{3+} are the two most effective and frequently used activators in LED phosphors due to their flexibility to control and tailor the photoluminescence properties. However, the properties of Eu^{2+} doped JEM phosphor have not been reported at present.

In this work, I reported the synthesis of Eu doped JEM phosphor by using La_2O_3, LaN, Si_3N_4, AlN and Eu_2O_3 as starting materials. Aiming at a phase pure JEM:Eu phosphor, the effects of synthesis temperature and chemical composition of starting materials (z value; N/O ratio and Si/Al ratio) were investigated. After getting the Eu doped single phase JEM sample, I further investigated the photoluminescence properties of JEM:Eu phosphor.

3.2 Experimental section

3.2.1 Sample preparation

Eu^{2+} doped $LaAl(Si_{6-z}Al_z)(N_{10-z}O_z)$ (z ~ 1) phosphor powder samples were prepared with a solid-state reaction method. Appropriate amount of starting materials including La_2O_3 (Shin-Etsu Chemical Co.), LaN, α-Si_3N_4 (SN-E10, Ube Industries), AlN (Tokuyama, E-grade) and Eu_2O_3 (Shin-Etsu Chemical Co.) powder were weighted with designed chemical compositions and then packaged in boron nitride crucibles in a glove box filled with nitrogen gas. The samples were fired in a nitrogen gas-pressure sintering furnace (Fujidempa Kogyo Co. Ltd., Osaka, Japan) at 1800 °C - 1900 °C for 2 hours. After heating, the sintered samples were finely ground with a mortar for further characterization.

3.2.2 Characterization

The characterization techniques related to X-ray diffraction, microstructure, photoluminescence spectra, diffuse reflectance spectra, temperature dependent luminescence spectra, quantum efficiency and luminescence decay have been described in the sections of 2.2 and 2.3 in Chapter 2. The quantitative analysis of crystalline phases was conducted with reference intensity ratio (RIR) method.[6] X-Ray absorption of the Eu-L_{III} edge was measured by the transparent method with the beam line BL9C of Photo Factory in KEK.

3.3 Results and discussion

3.3.1 Phase identification and microstructure

Grins et al. [1] reported the first synthesis of $LaAl(Si_{6-z}Al_z)(N_{10-z}O_z)$ (JEM, z ~ 1) phase material with an overall composition of $La_2Al_4Si_{11}N_{18}O_4$ synthesized at 1800 °C, containing 31.7% β-sialon as an impurity phase. Takahashi et al. [3] synthesized Ce doped JEM phosphor $La_{1-x}Ce_xSi_{6-z}Al_{1+z}O_zN_{10-z}$ (z = 1) at 1900 °C by using α-Si_3N_4, AlN, La_2O_3 and CeO_2 as starting materials. The JEM phase content reached 94% in case of x<0.5. However, β-sialon ($Si_{6-z}Al_zO_zN_{8-z}$) was still present as the only secondary phase. Afterwards, Takahashi et al. [5] tried to enhance JEM-

phase purity by setting z value to 1.5 and a synthesis temperature of 1800 °C. Yet a very small amount of La N-phase ($La_3Si_{6.5}Al_{1.5}N_{9.5}O_{5.5}$) formed, while β-sialon could also be detected. Some impure phases even coexisted inside one particle. Based on these previous works, it is believed that the temperature and chemical composition play a key role in JEM phase formation. However, there is no report in literature about the effect of temperature and chemical composition on JEM phase formation.

a. Temperature effect

5% Eu doped JEM ($La_{1-x}Eu_xSi_{6-z}Al_{1+z}O_zN_{10-z}$ with z = 1, x = 0.05) compositional sample was fired at different temperatures from 1800 °C to 1900 °C for 2 hours. Charge compensation has not been considered yet, as the charge balance for the JEM phase structure is complicated owing to the statistical distribution of La atoms.[1] The X-ray diffraction patterns of the products are shown in Figure 3.1a. The main phase observed is the JEM phase (ICSD 81057) for all samples. However, all samples also contain La N-phase (ICSD 93506). The amount of La N-phase is the largest at the lowest temperature (1800 °C) and decreases with increasing temperature, but even at the highest temperature (1900 °C) still some La N-phase is present. Besides the La N-phase, β-sialon (ICSD 74741) is also detected in the samples fired at 1800 °C and 1850 °C.

The sample synthesized at 1900 °C seems to contain the least amount of impurity (β-sialon) based on the XRD. However, the SEM images of the samples shown in Figure 3.1b display that the particles of the sample synthesized at 1900 °C contain a glassy surface, which is probably caused by some melting of the JEM phase during synthesis. The particles of the sample synthesized at 1850 °C are much rougher and do not have the glassy surface. It is therefore believed that the JEM phase could better be synthesized at 1850 °C in order to prevent melting the surface of the particles.

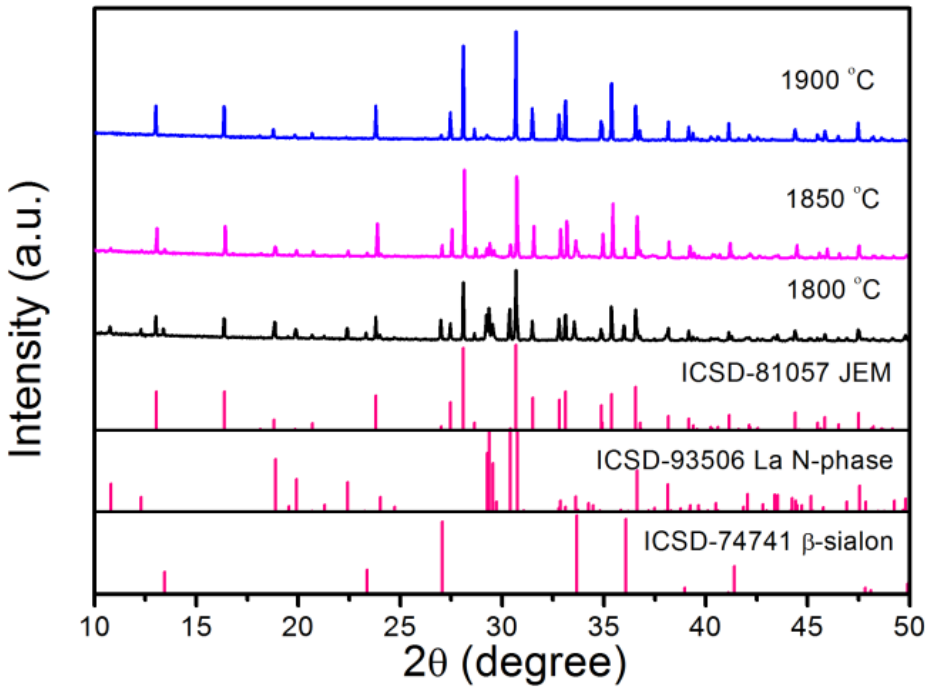

(a)

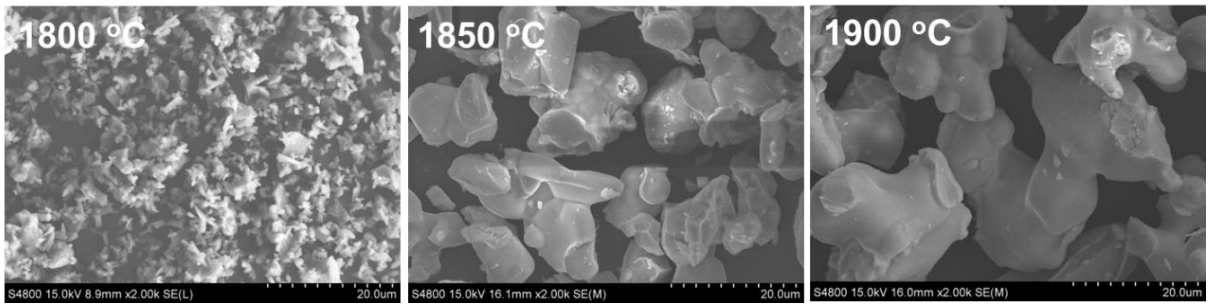

(b)

Figure 3.1 XRD patterns (a) and SEM images (b) of $La_{1-x}Eu_xSi_{6-z}Al_{1+z}O_zN_{10-z}$ (z = 1, x = 0.05) samples sintered at 1800 °C, 1850 °C and 1900 °C.

b. Composition effect

(1) z value effect

The target samples, 5% Eu doped JEM ($La_{1-x}Eu_xSi_{6-z}Al_{1+z}O_zN_{10-z}$, x = 0.05) with different z values (z = 1.00, 1.12, 1.25, 1.31, 1.50), were weighted according to the molar ratios of each starting material listed in Table 1 (samples No. 1-5) and fired at 1850 °C for 2 hours. The XRD patterns of the samples are shown in Figure 3.2a. The main phase is the JEM phase. However, all samples also contain La N-phase as an impurity phase, as well as a small amount of β-sialon,

except for the samples with z = 1.12 and 1.25 in which no beta-sialon is present. It should be noted that varying z value does not lead to a significant change of lattice parameters of the main phase, suggesting that a monophasic JEM sample might be achieved with a specific z value or a very narrow region of z values. When comparing the chemical composition of the crystalline phases (JEM, La N-phase and β-sialon), all of them are sialon phase materials but with different Si/Al and N/O ratios. It is therefore believed that the Si/Al and N/O ratios of the starting materials play a key role in the phase purity of JEM. The adjustment of the z value changes simultaneously the N/O ratio as well as the Si/Al ratio, as shown by the black line in the composition map of Figure 3.2b. It should be noted that the N/O ratio of starting materials might in reality be different from what is suggested by the ratios in Table 3.1, since the Si_3N_4 and AlN that were used probably contain some oxygen impurity. In addition, when Eu^{2+} ions substitute for La^{3+} ions, the charge compensation may affect the distribution of Si/Al and N/O. These might be the reason why it is difficult to get single JEM phase by just changing the z value.

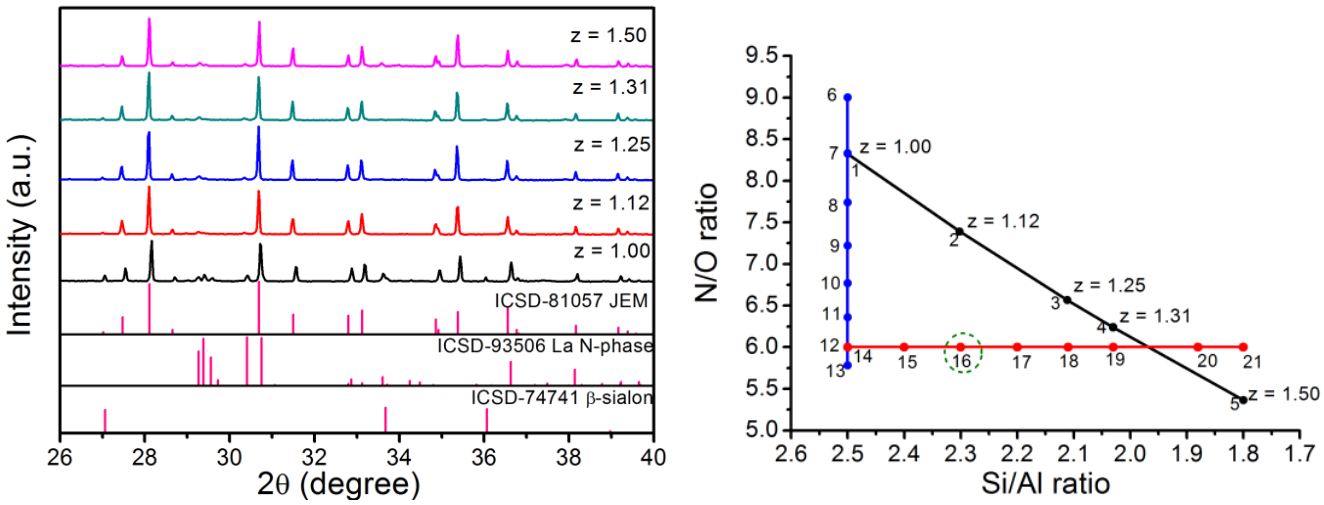

(a) (b)

Figure 3.2 (a) XRD patterns of 5% Eu doped JEM samples $La_{1-x}Eu_xSi_{6-z}Al_{1+z}O_zN_{10-z}$ with different z values (x = 0.05, z = 1.00, 1.12, 1.25, 1.31, 1.50); (b) chemical composition map of the N/O and Si/Al ratios according to the starting materials. The black line presents the change of z value; the blue line shows the change of N/O ratio with the Si/Al ratio fixed at 2.50; the Si/Al ratio was tuned as shown by the red line with N/O ratio fixed at 6.00. The number of each point stands for the sample number that is listed in Table 3.1 (samples No.1 and No.7 and samples No. 12 and No. 14 have the same chemical composition).

Table 3.1 z values, N/O ratio, Si/Al ratio and molar ratios of the starting materials for the synthesis of the JEM:Eu samples (The change in each sample is marked in bold).

No.	z value	Si/Al ratio	N/O ratio	La_2O_3	LaN	Si_3N_4	AlN	Eu_2O_3
1	**1.00**	2.50	8.33	0.32	0.32	1.67	2.00	0.025
2	**1.12**	2.30	7.39	0.36	0.24	1.63	2.12	0.025
3	**1.25**	2.11	6.57	0.40	0.16	1.58	2.25	0.025
4	**1.31**	2.03	6.24	0.42	0.12	1.56	2.31	0.025
5	**1.50**	1.80	5.37	0.48	0	1.50	2.50	0.025
6		2.50	**9.00**	0.31	0.33	1.67	2.00	0.025
7		2.50	**8.33**	0.32	0.32	1.67	2.00	0.025
8		2.50	**7.74**	0.36	0.23	1.67	2.00	0.025
9		2.50	**7.22**	0.38	0.18	1.67	2.00	0.025
10		2.50	**6.77**	0.41	0.13	1.67	2.00	0.025
11		2.50	**6.36**	0.43	0.08	1.67	2.00	0.025
12		2.50	**6.00**	0.45	0.04	1.67	2.00	0.025
13		2.50	**5.78**	0.48	0	1.67	2.00	0.025
14		**2.50**	6.00	0.45	0.04	1.67	2.00	0.025
15		**2.39**	6.00	0.45	0.04	1.63	2.05	0.025
16		**2.30**	6.00	0.45	0.04	1.62	2.11	0.025
17		**2.20**	6.00	0.45	0.04	1.60	2.18	0.025
18		**2.11**	6.00	0.45	0.04	1.58	2.25	0.025
19		**2.03**	6.00	0.45	0.04	1.57	2.31	0.025
20		**1.88**	6.00	0.45	0.04	1.53	2.45	0.025
21		**1.81**	6.00	0.45	0.04	1.52	2.51	0.025
22	1.12	2.30	7.93	0.37	0.25	1.63	2.12	**0**
23		2.30	6.00	0.48	0.04	1.62	2.11	**0.0025**
24		2.30	6.00	0.47	0.04	1.62	2.11	**0.005**
25		2.30	6.00	0.47	0.04	1.62	2.11	**0.01**
26		2.30	6.00	0.45	0.04	1.62	2.11	**0.025**
27		2.30	6.00	0.43	0.04	1.62	2.11	**0.05**
28		2.30	6.00	0.38	0.04	1.62	2.11	**0.10**

(2) N/O and Si/Al ratio effect

Since changing the value of z in $LaSi_{6-z}Al_{1+z}O_zN_{10-z}$ does not result in a pure sample, it is suggested that a pure JEM phase sample might be obtained if a sample composition does not follow the $La_{1-x}Eu_xSi_{6-z}Al_{1+z}O_zN_{10-z}$ (x = 0.05) formula which is shown on the black line but lies at another position in the composition map of Figure 3.2b. The Si/Al ratio was therefore fixed at 2.50, and samples with various N/O ratios were made by changing the amount of La_2O_3 and LaN while keeping the amount of La constant, as shown by the blue line in Figure 3.2b. The chemical composition of the samples (samples No. 6-13) is listed in Table 3.1.

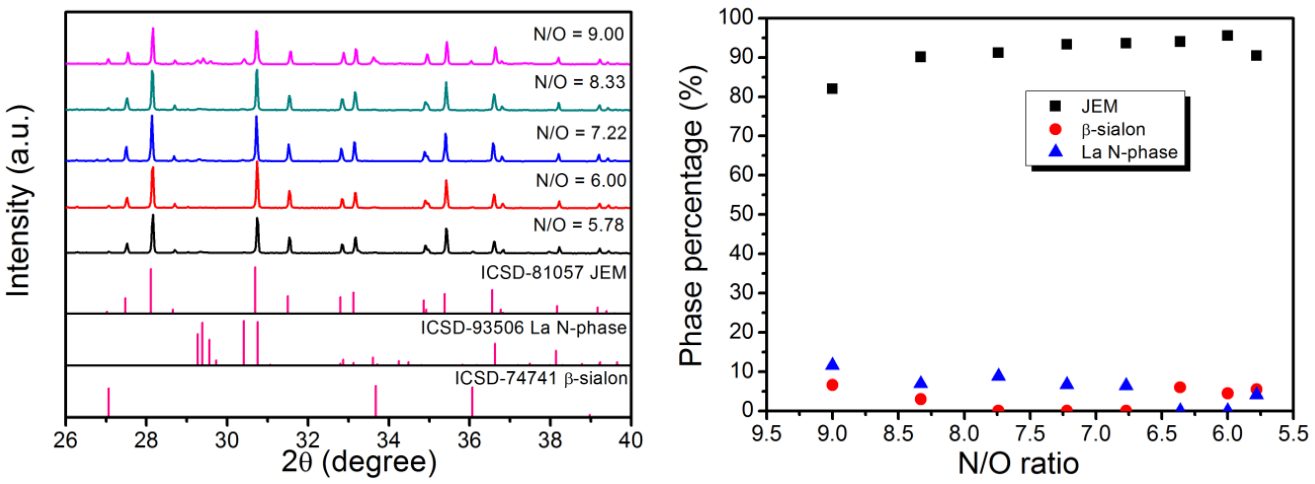

(a) (b)

Figure 3.3 (a) XRD patterns of JEM:Eu samples with different N/O ratios (N/O = 9.00, 8.33, 7.22, 6.00, 5.78) and (b) quantitative analysis of phases for samples with various N/O ratios.

Figure 3.3a shows that the JEM phase purity is improved by decreasing the N/O ratio. The La N-phase impurity disappears when the N/O ratio is 6.00, with only β-sialon left as a secondary phase. When the N/O ratio is 5.78 (sample No. 13), no LaN is added as a starting material and the La N-phase impurity appears again. By analyzing the phase percentages of the samples with different N/O ratios, as shown in Figure 3.3b, it is found that an oxygen rich composition can enhance the phase purity of JEM if the Si/Al ratio is fixed at 2.50. As β-sialon still coexisted with the JEM phase when the N/O ratio is 6.00, the Si/Al ratio was tuned by changing the amount of Si_3N_4 and AlN and keeping the N/O ratio at 6.00 as shown by the red line in Figure 3.2b. The molar ratios of the starting materials are shown in Table 3.1 (samples No. 14-21).

When the N/O ratio is kept with the value of 6.00, the JEM phase purity is significantly improved by changing the Si/Al ratio, as shown in Figure 3.4. Especially for samples with Si/Al = 2.30, 2.11 and 2.20, in which the amount of La N-phase is less than 1%. So carefully controlling the Si/Al ratio is very important to remove the β-sialon impurity phase. Figure 3.4a shows that a single phase JEM phosphor is obtained for the sample with Si/Al = 2.30 and N/O = 6.00 (sample No. 16). The chemical composition is also marked with a green circle in Figure 3.2b, deviating a little from the formula of JEM sialon with z = 1.12 (sample No. 2).

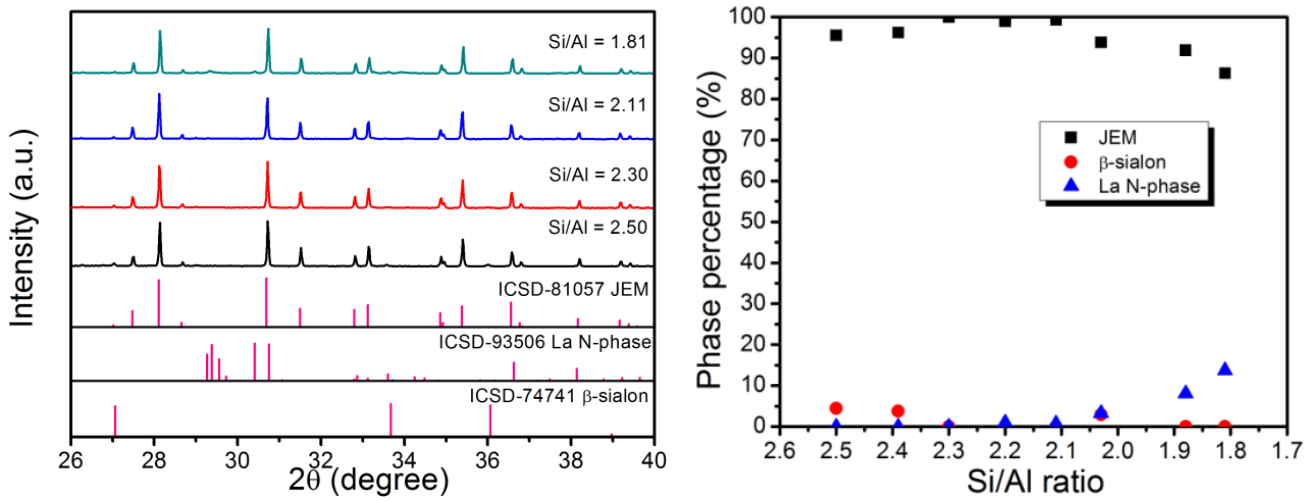

(a) (b)

Figure 3.4 (a) XRD patterns of samples with different Si/Al ratios (Si/Al = 2.50, 2.30, 2.11, 1.81) and (b) quantitative analysis of phases for samples with various Si/Al ratios.

3.3.2 Photoluminescence properties

JEM:xEu (x = 0.005, 0.01, 0.02, 0.05, 0.10, 0.20) samples (samples No. 23-28) were weighted with the ratios of N/O = 6.00 and Si/Al = 2.30, as this is the optimal composition to get single phase according to the experiments mentioned above. It should be noticed that no impure phase can be detected for all samples regardless of the Eu concentration. The variable occupancy of rare earth site should be considered in the detailed structure analysis. For non-doped JEM sample, when a sample was prepared with the optimal ratios of N/O = 6.00 and Si/Al = 2.30, a little bit of the La N-phase was observed; the proper composition to reach single non-doped JEM sample (sample No. 22) is N/O = 7.93 and Si/Al = 2.30, and the corresponding z value is 1.12; This again indicates the precise composition control is important to obtain a single phase JEM. The molar ratio of each sample has been listed in Table 3.1 (samples No. 22-28). Their photoluminescence properties are further investigated.

a. Reflectance and Eu valence

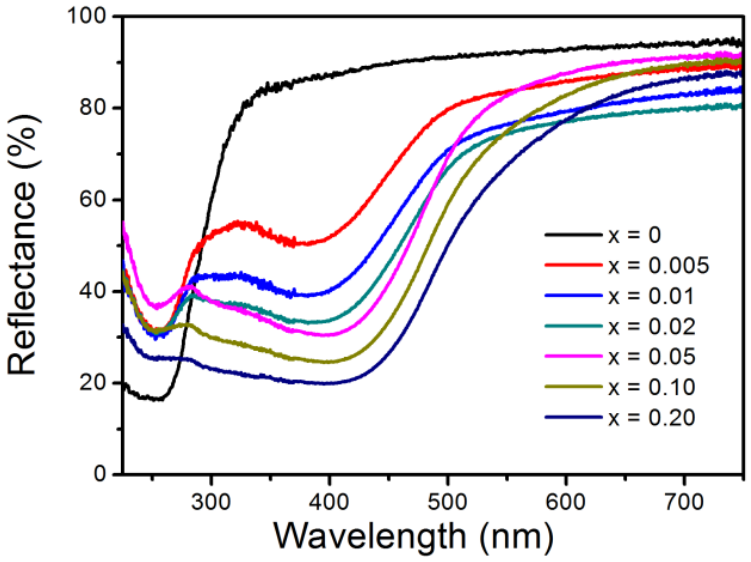

Figure 3.5 Diffuse reflectance spectra of JEM:xEu samples with various Eu concentration (x = 0, 0.005, 0.01, 0.02, 0.05, 0.10, 0.20).

Figure 3.5 shows the diffuse reflectance spectra of non-doped and Eu doped JEM samples. A strong absorption band is observed below 300 nm in the non-doped sample, which can be attributed to the electronic transition from valence to conduction band of the host lattice. This is in agreement with the fact that the non-doped JEM sample has a white color. Eu doping of JEM yields light-blue to yellow body colored samples due to a strong absorption band between 400 and 600 nm. With increasing Eu concentration, the absorption becomes stronger and the absorption edges shift to longer wavelength. This band is therefore assigned to the 4f-5d transition of Eu^{2+}, indicating that Eu is present in the divalent state in the JEM phosphor.

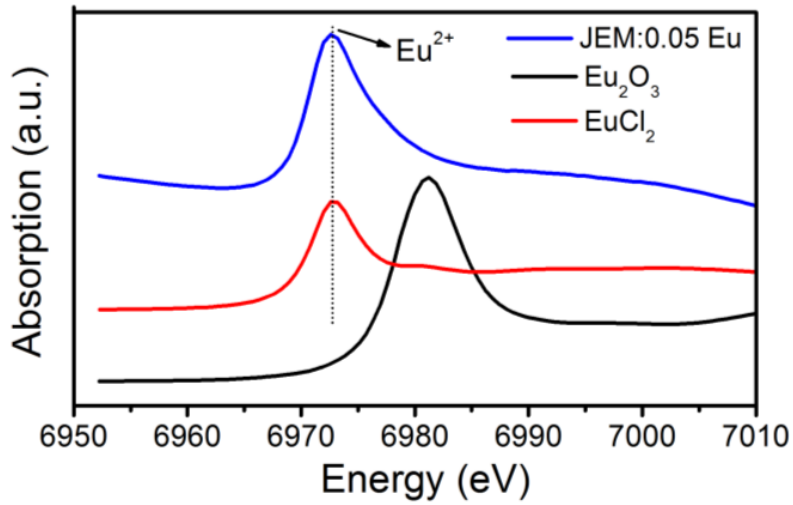

Figure 3.6 The Eu L_{III} XANES spectra of JEM:0.05Eu phosphor and Eu_2O_3, $EuCl_2$ referenced samples for Eu^{3+}, Eu^{2+}, respectively.

The Eu L_{III} edge XANES spectrum of JEM:0.05Eu is shown in Figure 3.6 together with the reference spectra of $EuCl_2$ and Eu_2O_3. The absorption edge of JEM:0.05Eu is located at 6973 eV and coincides with the Eu^{2+} reference position from $EuCl_2$. There is no trace of Eu^{3+} in the JEM:0.05Eu sample, which further confirms that all the Eu ions in the JEM:0.05 Eu phosphor are divalent. This is due to carbon heating at high temperature, which can provide the reductive atmosphere.[7]

b. Eu concentration dependent photoluminescence properties

Figure 3.7a and 3.7b show the excitation and emission spectra of the JEM:xEu phosphors measured at room temperature, respectively. The excitation band gradually becomes broader with increasing Eu concentration, and the maximum of the excitation band is the largest for x = 0.02. As Figure 3.7b shows, the emission intensity increases with higher Eu concentrations and reaches a maximum when x = 0.02. The intensity decreases again when x is over 0.02. The emission band also becomes broader with rising Eu concentration. The full width at half maximum (FWHM) increases from 115 nm when x = 0.005 to 127 nm when x = 0.20, as presented in Figure 3.7c.

The JEM structure has only one La site on which the Eu^{2+} can substitute and La atoms statistically occupy the 8(d) site[1]. In addition, the La atoms are found to be irregularly coordinated by seven anions in JEM structure and the charge compensation makes the coordination environment of Eu^{2+} very complicated. Therefore, a variety of local structures around Eu^{2+} give rise to inhomogeneous broadening, which makes the emission bandwidth of JEM:Eu^{2+} relatively large. A similar case has been observed for the $CaAlSiN_3$:Eu^{2+} phosphor, for which it was reported that the inhomogeneous broadening originates from random distribution of Si and Al ions at an identical crystal site.[8]

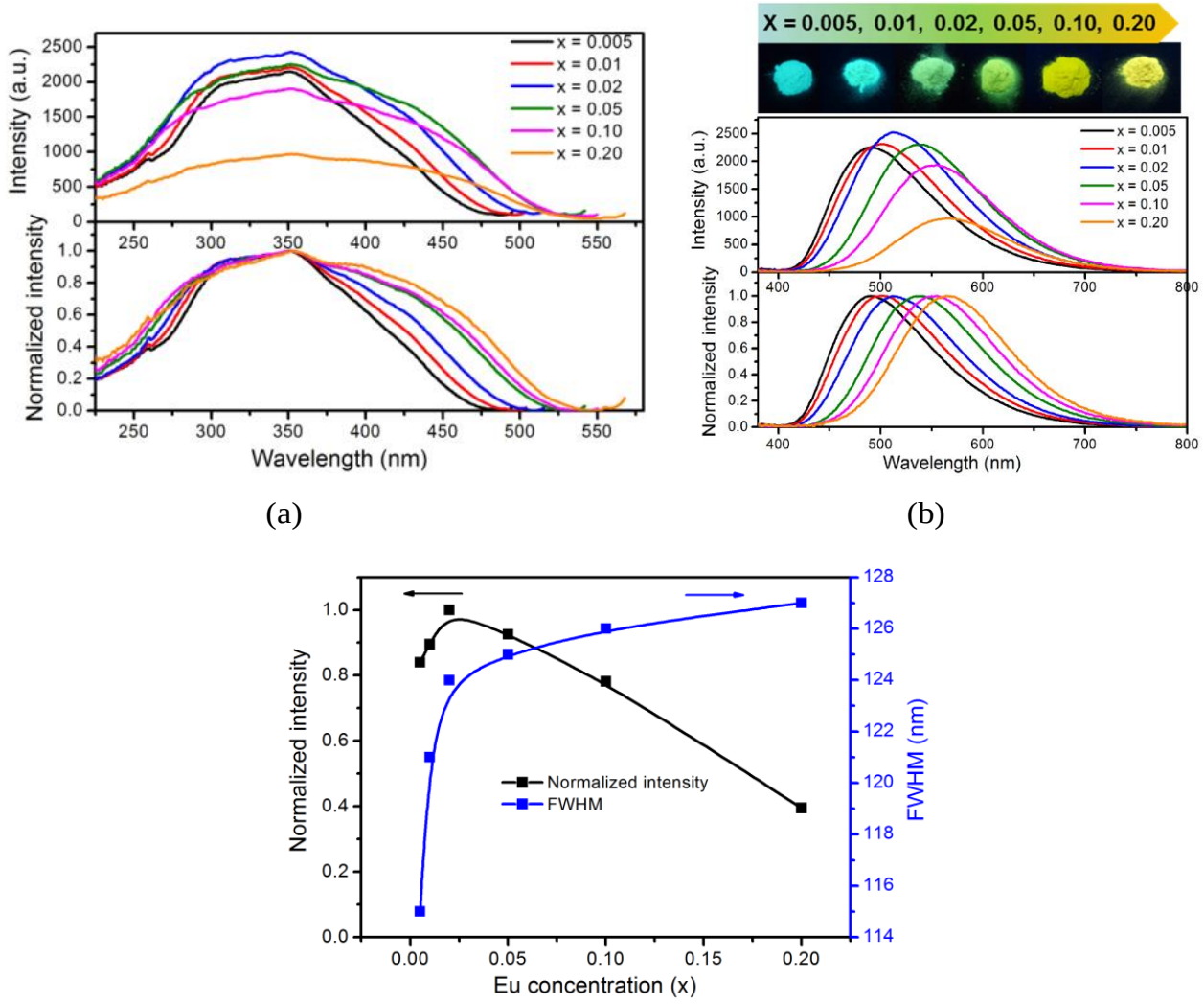

Figure 3.7 JEM:xEu (x =0.005, 0.01, 0.02, 0.05, 0.10, 0.20) samples as measured and normalized excitation spectra (a); emission spectra after 355 nm excitation and luminescence photos of the samples excited by 365 nm UV lamp (b); normalized emission intensity and FWHM (c). The excitation spectra were monitored with the emission peak wavelength.

Another interesting characteristic of the JEM:Eu samples is the unusual large red-shift (490→564 nm) of the emission band that is observed with the increase of the Eu concentration, implying that the luminescence properties of JEM:Eu^{2+} phosphor can be tailored by controlling the Eu concentration. Figure 3.8 shows that the emission band of low concentrated samples is asymmetrical, and can be fitted with two Gaussian curves, which represent high and low energy emission bands. This suggests that there are at least two types of Eu^{2+} sites; one site gives rise to

the higher energy emission band and the other site gives rise to the lower energy emission band. Note that, when x is 0.10, the emission spectrum almost solely consists of the band at longer wavelength, as shown in Figure 3.8.

It is suggested that the main reason for the red shift at lower concentration is different from that at higher concentration. At low concentrations the redshift is mainly caused by a change in distribution of the Eu^{2+} ions over the two sites. Eu^{2+} ions may prefer to occupy the high energy site, which results in a relatively large contribution of the emission at shorter wavelengths. This can be seen from the intensity of the shorter wavelength emission band, which is higher than that of the longer wavelength emission band when the Eu concentration is below 2%. With increasing Eu concentration also the lower energy site will be occupied more, causing a redshift of the emission. A similar explanation has also been reported for $La_{2.5}Ca_{1.5}Si_{12}O_{4.5}N_{6.5}:Eu^{2+}$ [9]. With further increasing the Eu concentration, the red-shift of the emission is further enhanced by energy transfer among Eu^{2+} ions. With increasing Eu concentration the average distance between Eu^{2+} ions becomes shorter, increasing the probability of energy transfer from Eu^{2+} ions at the high energy site towards Eu^{2+} ions at the low energy site. Hence, the increase of the possibility for non-radiative energy transfer between Eu ions at different sites, causes a red-shift of the emission band. This can also be confirmed from Figure 3.8 where the relative intensity of the shorter wavelength emission band becomes lower with increasing Eu concentration and the shorter wavelength emission band almost disappears when Eu concentration reaches 10%. A similar case was also observed in $La_{2.5}Ca_{1.5}Si_{12}O_{4.5}N_{6.5}:Eu^{2+}$ [9] and $Lu_3Al_5O_{12}:Ce^{3+}$ [10].

It should be noted that, due to the partial overlap of emission and excitation spectra, the reabsorption of high-energy emitted photons also contributes to the red-shift. In addition, a lowering of the 5d level further enhances the red-shift with the rise of Eu concentration. These latter two effects are commonly observed in Eu^{2+} doped samples. However, they cannot by itself account for the very large red-shift (490 → 564 nm) and changes in the emission spectrum that are observed with increasing Eu concentration, which can only be fully explained by also taking energy transfer between Eu^{2+} ions at different sites into account.

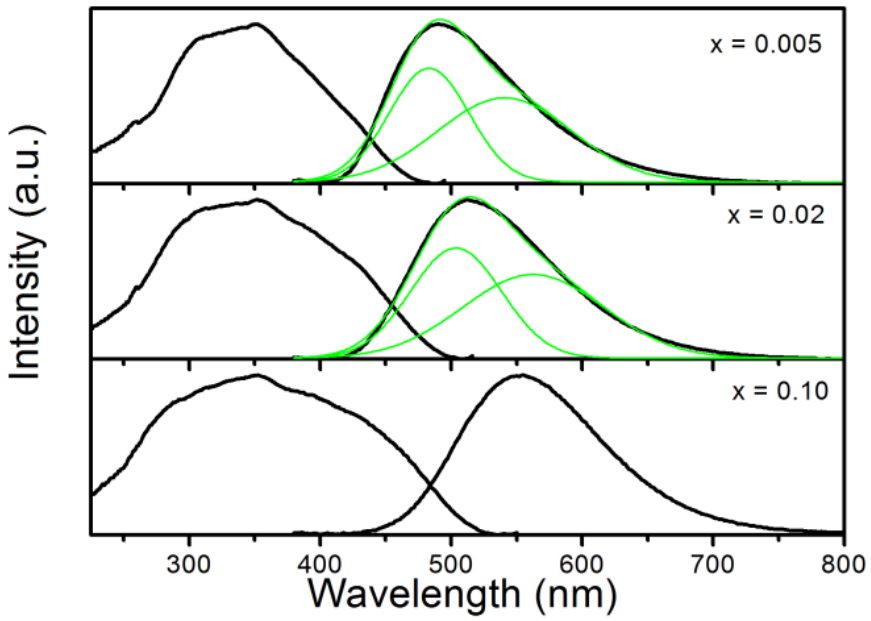

Figure 3.8 Excitation spectra and Gaussian fitting of emission spectra for samples JEM:xEu (x =0.005, 0.02, 0.10) after 355 nm excitation.

c. Temperature dependence luminescence properties

Figure 3.9 shows the emission spectra of JEM:0.02Eu^{2+} (sample No. 25) over a temperature range from 4 K to 573 K. The emission intensity almost immediately starts to drop above 4 K, falling to 83% at 100 K as compared to the intensity at 4 K. Further increasing the temperature results in a nearly linear relation between temperature and luminescence intensity, dropping to 10% around 573 K. The emission is thermally quenched by 50% at room temperature as compared to the emission at 4 K, which leads to relatively low quantum efficiency (IQE = 37%).

In general, the quenching of the 5d→4f luminescence of Eu^{2+} is explained by either thermally activated cross-over from the $4f^6$5d excited state to the $4f^7$ ground state, or the thermal ionization from the $4f^6$5d excited state to the bottom of the conduction band.[11-12] The stokes shift is estimated at 0.23 eV by taking twice the energy difference between the zero phonon line energy and the energy of the emission peak.[13] Given the relatively small stokes shift and low thermal quenching temperature, the thermal quenching is more likely due to thermal ionization from the 5d level to the conduction band, as this has also been suggested as the reason for thermal quenching in other Eu^{2+} doped nitrido-silicates.[12, 14]

Note however that there is a noticeable feature of the JEM phosphor as the luminescence intensity of JEM:Eu shows a much more gradual decrease with increasing temperature; although the luminescence already starts to quench around 4 K, there is still 10% of the luminescence left around 573 K. It is noticed that this slow quenching behavior is due to multiple competitive relaxation processes. One possible reason is related to the two different luminescent sites in Eu^{2+} doped JEM phosphor, as the two sites may have a different energy barrier for thermal quenching. The energy transfer between the two sites may also depend on temperature and therefore influence the luminescence intensity. Furthermore, the emission band shows a slight redshift and a small change of shape with increasing temperature. These changes can also be related to the two types of emission sites in Eu^{2+} doped JEM phosphor with different thermal quenching behavior.

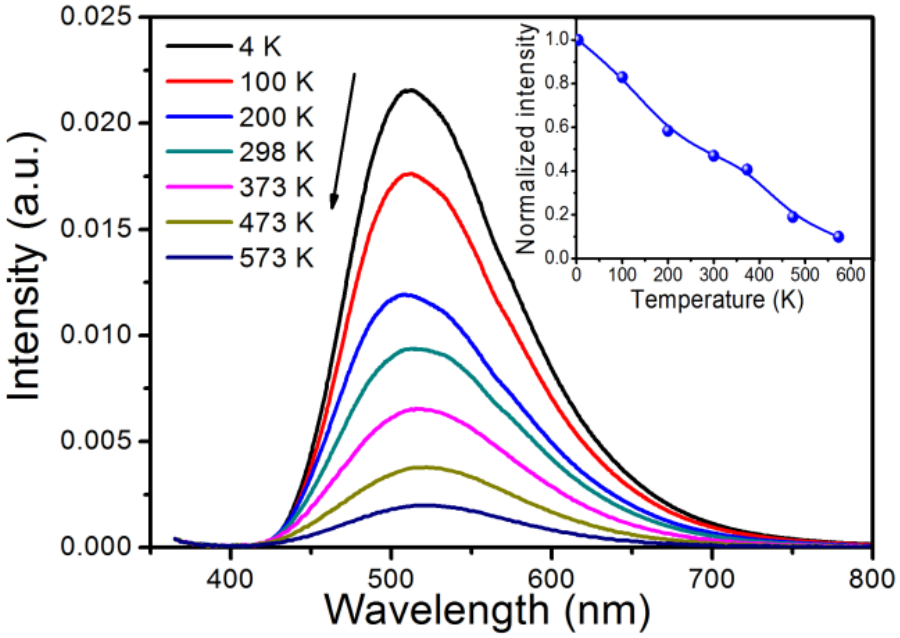

Figure 3.9 Emission spectra of JEM:0.02Eu sample at different temperatures after 355 nm excitation. The inset shows the integrated emission intensity as a function of temperature for the sample, relative to the maximum intensity at 4 K.

d. Luminescence decay

The luminescence decay of JEM:xEu (x = 0.005, 0.02, 0.10) samples are shown in Figure 3.10. The samples were excited with 370 nm nano LED light and monitored at two different emission

wavelengths with 480 nm and 560 nm, respectively. The decay curves show non-linear decay, which can be reasonably fitted using a bi-exponential function:[15]

$$I = A_1 exp\left(-\frac{t}{\tau_1}\right) + A_2 exp\left(-\frac{t}{\tau_2}\right)$$

where I is the luminescence intensity; A_1 and A_2 are constants; t is the time; and τ_1 and τ_2 are the lifetimes for the exponential components. The double decay is a strong evidence that there are at least two types of Eu^{2+} ions. The effective decay time τ can be calculated according to the formula:

$$\tau = (A_1\tau_1^2 + A_2\tau_2^2)/(A_1\tau_1 + A_2\tau_2)$$

Regarding to the JEM:xEu samples with x = 0.005, 0.02, 0.10, the calculated effective decay times are 0.67 μs, 0.51 μs and 0.39 μs for the 480 nm emission, and 1.05 μs, 1.15 μs and 1.02 μs respectively, which are close to the typical value of Eu^{2+} decay.[16] For all concentrations, the 480 nm emission shows faster decay than the 560 nm emission, indicating that the decay related to the high energy site is faster than the decay associated with the low energy sites. The decay time for the 560 nm emission initially increases with rising Eu concentration, which is due to the energy transfer from the high energy Eu^{2+} site to the low energy Eu^{2+} site, as the high energy Eu^{2+} sites with faster decay have a larger contribution to the emission of the low Eu concentrated samples. For the high Eu concentrated sample, concentration quenching leads to a shorter decay.

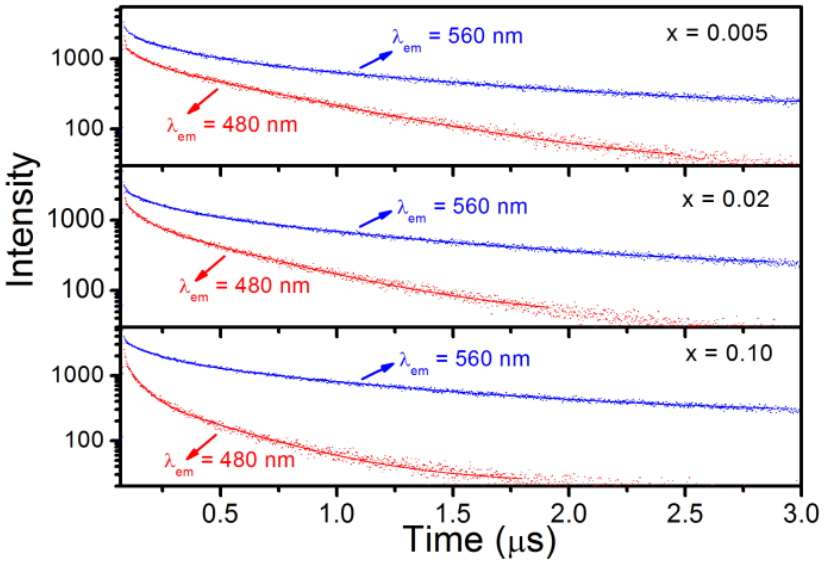

Figure 3.10 Luminescence decay curves of JEM:xEu (x = 0.005, 0.02, 0.10) samples after 370 nm excitation, monitoring the 480 nm (red lines) and 560 nm emission (blue lines).

In order to further confirm there are two types of Eu^{2+} emission sites, time-resolved photoluminescence emission spectra have been measured as shown in Figure 3.11. Each time-resolved photoluminescence emission spectrum contains two distinctive Gaussian peaks, which confirms the existence of the two luminescent centers. The intensity of the high energy component reduces with rising the delay time, which is in agreement with the observation that the short monitored wavelength leads to faster decay rate, as shown in Figure 3.10.

The broad Eu^{2+} emission band, the red-shift of the Eu^{2+} emission with increasing concentration, the unusual thermal quenching behavior, the luminescence decay curves and the time-resolved photoluminescence spectra all indicate that there are two types of Eu^{2+} luminescent centers in JEM:Eu^{2+} phosphor. However, since there is only one type of La site in the JEM structure, it is believed that the second luminescent center is cause by local inhomogeneous distribution of Si/Al and/or O/N. This would be similar as has been observed for $CaAlSiN_3$:Eu^{2+}, [26] where there is only one type of Ca site, but nevertheless two types of luminescent centers due to inhomogeneous distribution of Si/Al, resulting in Eu^{2+} ions in Si rich and Al rich local environments. Further detailed investigations of the JEM structure in order to determine the precise distribution of the Si, Al, O and N atoms would be required to get a full understanding of the nature of the two luminescent centers in the JEM structure.

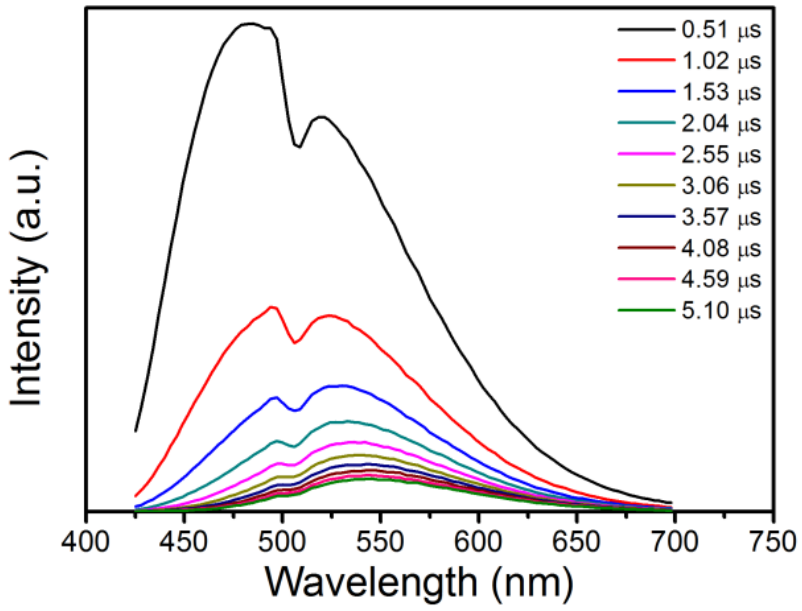

Figure 3.11 Time-resolved photoluminescence emission spectra of JEM:0.02 Eu phosphor.

3.4 Conclusions

A phase pure JEM:Eu^{2+} green-emission phosphor was obtained with a solid-state reaction at 1850 °C for 2 hours by using La_2O_3, LaN, Si_3N_4, AlN and Eu_2O_3 as starting materials in a Si/Al ratio of 2.30 and N/O ratio of 6.00. The phosphor can be excited with UV or blue light, resulting in a broad Eu^{2+} 5d-4f emission band which has, at low Eu concentrations, a maximum at 490 nm. With increasing Eu concentration, the emission band changes shape and its maximum shifts to 564 nm, shifting the emission color from blue-green to yellow. These changes suggest that there are two types of emission sites, although there is only one crystallographic site in JEM structure. Furthermore, Eu^{2+} doped JEM phosphor shows an abnormal nearly linear thermal quenching behavior. The non-linear luminescence decay with bi-exponential curve and time-resolved photoluminescence emission spectra with two distinctive Gaussian peaks further confirm the existence of two types of emission sites.

Since the phase pure Eu^{2+} doped JEM sialon phosphors and non-doped JEM sample have now been prepared by adapting the chemical composition and carefully controlling the temperature, it will be of interest to investigate whether a phase pure Ce^{3+} doped JEM phase phosphor may also be obtained using a similar approach, as JEM:Ce phosphor has been mentioned as a strong candidate for home illumination.[8] Additionally, the availability to obtain the single JEM sialon sample makes it possible to further investigate the details of JEM structure, which could not be done up till now because of the lack of a single phase sample.

3.5 References

(1) Grins, J.; Shen, Z.; Nygren, M.; Ekström, T. Preparation and Crystal Structure of $LaAl(Si_{6-Z}Al_Z)N_{10-Z}O_Z$ *Journal of Materials Chemistry* **1995**, *5*, 2001-2006.

(2) Riedel, R.; Chen, I.-W., *Ceramics Science and Technology, Materials and Properties*. John Wiley & Sons: 2011; Vol. 2.

(3) Takahashi, K.; Hirosaki, N.; Xie, R.-J.; Harada, M.; Yoshimura, K.-i.; Tomomura, Y. Luminescence Properties of Blue $La_{1-x}Ce_xAl_z(Si_{6-z}Al_z)(N_{10-z}O_z)$ (z ~ 1) Oxynitride Phosphors and Their Application in White Light-Emitting Diode *Applied Physics Letters* **2007**, *91*, 091923.

(4) Takahashi, K.; Harada, M.; Yoshimura, K.-i.; Fukunaga, H.; Tomomura, Y.; Hirosaki, N.; Xie, R.-J. Improved Photoluminescence of Ce^{3+} Activated $LaAl(Si_{6-z}Al_z)(N_{10-z}O_z)$(z ~ 1) Blue Oxynitride Phosphors by Calcium Co-Doping *Ecs Journal of Solid State Science and Technology* **2012**, *1*, R109-R112.

(5) Takahashi, K.; Dierre, B.; Cho, Y.; Sekiguchi, T.; Xie, R. J.; Hirosaki, N. Microanalysis of Calcium Codoped $LaAl(Si_{6-z}Al_z)(N_{10-z}O_z)$(z ~ 1):$Ce^{3+}$ Blue Phosphor *Journal of the American Ceramic Society* **2015**, *98*, 1253-1258.

(6) Hubbard, C. R.; Evans, E.; Smith, D. The Reference Intensity Ratio, I/I_c, for Computer Simulated Powder Patterns *Journal of Applied Crystallography* **1976**, *9*, 169-174.

(7) Takeda, T.; Hirosaki, N.; Xie, R.-J.; Kimoto, K.; Saito, M. Anomalous Eu Layer Doping in Eu, Si Co-Doped Aluminium Nitride Based Phosphor and Its Direct Observation *Journal of Materials Chemistry* **2010**, *20*, 9948-9953.

(8) Lee, S.; Sohn, K.-S. Effect of Inhomogeneous Broadening on Time-Resolved Photoluminescence in $CaAlSiN_3:Eu^{2+}$ *Optics Letters* **2010**, *35*, 1004-1006.

(9) ten Kate, O.; Xie, R.; Funahashi, S.; Takeda, T.; Hirosaki, N. Significant Colour Tuning Via Energy Transfer in Eu^{2+} Solely Doped $La_{2.5}Ca_{1.5}Si_{12}O_{4.5}N_{16.5}$ *RSC Advances* **2016**, *6*, 20681-20686.

(10) Piquette, A. P.; Hannah, M. E.; Mishra, K. C. An Investigation of Self-Absorption and Corresponding Spectral Shift in Phosphors *Gallium Nitride and Silicon Carbide Power Technologies 3* **2012**, *41*, 1-9.

(11) Dorenbos, P. Thermal Quenching of Eu^{2+} 5d–4f Luminescence in Inorganic Compounds *Journal of Physics: Condensed Matter* **2005**, *17*, 8103.

(12) Bachmann, V.; Jüstel, T.; Meijerink, A.; Ronda, C.; Schmidt, P. J. Luminescence Properties of $SrSi_2O_2N_2$ Doped with Divalent Rare Earth Ions *Journal of Luminescence* **2006**, *121*, 441-449.

(13) Nazarov, M.; Tsukerblat, B. Vibronic Coupling Parameters and Stokes Shift in Thiogallate Phosphors *Journal of Physics and Chemistry of Solids* **2008**, *69*, 2605-2612.

(14) Mikami, M.; Shimooka, S.; Uheda, K.; Imura, H.; Kijima, N. In *Key Engineering Materials*; Trans Tech Publ: 2008; Vol. 403, p 11-14.

(15) Long, Q.; Wang, C.; Ding, J.; Li, Y.; Wu, Q.; Wang, Y. Synthesis and Luminescence Properties of a Novel Red-Emitting $LiSr_4(BN_2)_3:Eu^{2+}$ Phosphor *Dalton Transactions* **2015**, *44*, 14507-14513.

(16) Poort, S.; Meyerink, A.; Blasse, G. Lifetime Measurements in Eu^{2+}-Doped Host Lattices *Journal of Physics and Chemistry of Solids* **1997**, *58*, 1451-1456.

Chapter 4 Photoluminescence properties of JEM:Ln (Ln = Ce, Eu, Sm, Yb) and the 4f and 5d energy level locations of the lanthanides in JEM

The content of this chapter has been submitted to Journal of Materials Chemistry C.

4.1 Introduction

Ce doped $LaAl(Si_{6-z}Al_z)(N_{10-z}O_z)$ ($z \approx 1$, termed JEM phase) phosphor has been reported to be a promising blue phosphor for white LED application, especially for illumination grade lighting.[1] A high color rendering index of 95-96 with various correlated color temperatures was achieved for white LEDs in which JEM:Ce phosphor was used as a blue phosphor component.[1] However, the unavailability of phase pure JEM:Ce has prevented commercial application. Due to the lack of a single phase JEM:Ce sample, it has been very difficult to truly assess its quantum efficiency. In addition, the thermal quenching behavior and luminescence decay of JEM:Ce have never been investigated before.

In chapter 3, I reported on the synthesis and optical properties of Eu^{2+} doped JEM phosphor.[2] I was able to synthesize a phase pure JEM:Eu sample for the first time, by carefully controlling the chemical composition and synthesis conditions of the solid-state reaction. In addition, I found that JEM:Eu^{2+} exhibits a bi-exponential luminescence decay behavior and an abnormal nearly linear thermal quenching behavior,[2] even though there is only one crystallographic La site in JEM structure on which Eu^{2+} can substitute.

In this work, the nearly single phase JEM:Ce phosphors have been synthesized with a solid-state reaction method by carefully controlling the synthesis condition. The photoluminescence properties, luminescence decay and thermal quenching are investigated. The results are then compared to JEM:Eu phosphor in order to get a better understanding of the luminescence mechanisms and lanthanide site. JEM:Yb and JEM:Sm phosphors are also prepared and an energy level scheme is constructed that displays the locations of the 4f and 5d states of the lanthanide ions within the bandgap of the JEM structure. The energy level scheme is used to clarify the optical data, and to predict the photoluminescence properties of lanthanide doped JEM phosphors.

4.2 Experimental section

4.2.1 Synthesis

Ce, Eu, Yb and Sm doped $LaAl(Si_{6-z}Al_z)(N_{10-z}O_z)$ phosphor powder samples were synthesized with a solid-state reaction method. Starting materials including La_2O_3 (Shin-Etsu Chemical Co.), LaN (Kojundo Chemical Laboratory co.), α-Si_3N_4 (SN-E10, Ube Industries), AlN (Tokuyama, E-grade) and CeO_2, Eu_2O_3, Sm_2O_3, Yb_2O_3 (Shin-Etsu Chemical Co.) were used. 2 g starting materials were weighted with designed chemical compositions and mixed in a glove box filled with nitrogen gas, then packaged in boron nitride crucibles for firing. The samples were fired in a nitrogen gas-pressure sintering furnace (Fujidempa Kogyo Co. Ltd., Japan) at 1850 °C for 2 hours. After heating, the sintered samples were cooled down and finely ground with a mortar for further characterization.

4.2.2 Characterization

The characterization techniques of X-ray diffraction, photoluminescence spectra, diffuse reflectance spectra, temperature dependent luminescence spectra, quantum efficiency and luminescence decay are described in the sections of 2.2 and 2.3 in Chapter 2. The Ce L_3 X-ray absorption near edge structure (XANES) was detected by the transparent method with the beam line BL9C (Photo Factory, KEK, Japan). The photoluminescence spectra of Yb doped samples are measured with a Photal QE-2100 lamp combined with MCPD-9800 detectors. An MCPD-9800 spectrometer system combined with an integrating sphere was also used to measure the emission and reflectance of the phosphors for calculating internal quantum efficiency (IQE). The details have been described in previous work.[2]

4.3 Results and discussion

4.3.1 Synthesis and XRD analysis of JEM:Ce

Ce doped JEM phosphors ($La_{(1-x)}Si_{6-z}Al_{1+z}N_{10-z}O_z$:xCe) with x = 0.05 and different z values were prepared by using the starting materials in the ratio (1-x)/3 La_2O_3 : (1-x)/3 LaN : (6-z)/3 Si_3N_4 : (1+z) AlN : x CeO_2. As shown in Figure 4.1, when the z values are 0.90, 1.25 and 1.50, the La N-phase (ICSD 93506, $La_3Si_{6.5}Al_{1.5}N_{9.5}O_{5.5}$) impurity can be detected. A small amount of β-sialon (ICSD 74741, $Si_{6-z}Al_zO_zN_{8-z}$) can also be observed for the samples with the z value of 1.00 (containing 2.4% β-sialon) and 1.12 (containing 1.6% β-sialon). So the highest purity was

obtained when the z value is 1.12, resulting in nearly single phase (98.4% JEM) JEM:Ce phosphor. Note that for an Eu^{2+} doped JEM sample a different composition is necessary, as I reported before,[2] because a pure Eu^{2+} doped sample cannot be obtained by exactly following the $LaSi_{6-z}Al_{1+z}N_{10-z}O_z$ formula, independent of the choice of z. In order to obtain a pure Eu doped sample, the chemical composition should have, according to the starting materials, a Si/Al ratio of 2.30 and a N/O ratio of 6.00.[2] A reason for this difference may be the charge compensation that is necessary when a divalent Eu^{2+} ion is substituted on a trivalent La^{3+} site.

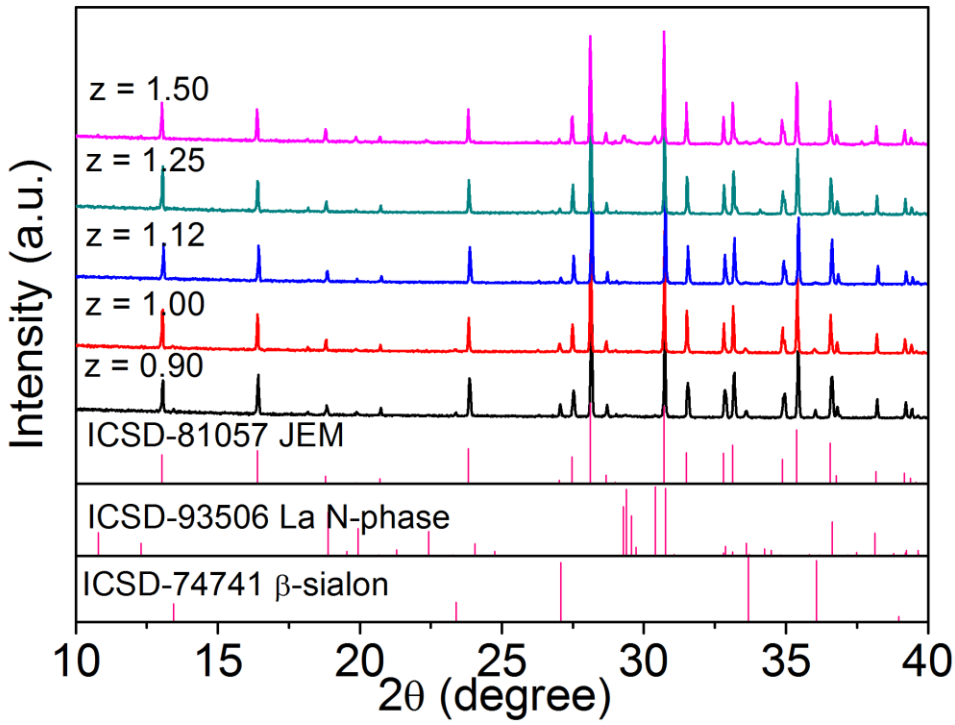

Figure 4.1 X-ray diffraction patterns of $La_{(1-x)}Si_{6-z}Al_{1+z}N_{10-z}O_z$:xCe phosphors (x = 0.05, z = 0.90, 1.00, 1.12, 1.25, 1.50).

4.3.2 Photoluminescence properties of JEM:Ce phosphors

Figure 4.2a shows the excitation and emission spectra of 1% and 5% Ce doped JEM phosphor. JEM:0.01Ce phosphor displays a broad Ce^{3+} 4f-5d absorption band extending from UV to 415 nm, with a maximum at 355 nm. Excitation at 355 nm yields a relatively narrow emission band (FWHM = 74 nm) centered at 420 nm, which is attributed to the Ce^{3+} 5d-4f transition. The Ce L_3 XANES spectra shown in Figure 4.2b further confirm that all of Ce ions in JEM:0.05Ce phosphor are present in trivalent state. The emission band is composed of two bands centered at

414 nm (3.00 eV) and 448 nm (2.77 eV) attributed to the emission from the 5d excited state to the $^2F_{5/2}$ and $^2F_{7/2}$ ground states. The excitation spectrum of 5% Ce doped JEM phosphor extends from UV to 425 nm. It is similar in shape as that of 1% Ce doped JEM, and also has a maximum at 355 nm. The emission band of the JEM:0.05Ce phosphor observed after 355 nm excitation is centered at 430 nm, and has a FWHM of 81 nm. The emission band is thus slightly broader and shifts to longer wavelength as compared to the 1% Ce doped phosphor. When exciting the 5% doped sample with 405 nm light, the emission maximum shifts to 455 nm. That is slightly shorter than what has been reported by Takahashi et al[1] for 5% doped JEM:Ce sample, showing an emission maximum at 470 nm for 405 nm excitation. Note however that the sample from the previous report contained a higher amount of β-sialon impurity phase,[1] which may have caused a redshift of the emission. As a result of the higher phase purity, the luminescence efficiency of our sample is improved as compared to the efficiency reported in the previous report. At 405 nm excitation, I obtain an IQE of 57% for a 5% Ce doped sample as compared to an IQE of 35% in the previous report for a sample with the same Ce concentration. At 355 nm excitation, I obtain an even higher IQE, namely 75% for a 5% Ce doped sample and 69% for a 1% Ce doped sample.

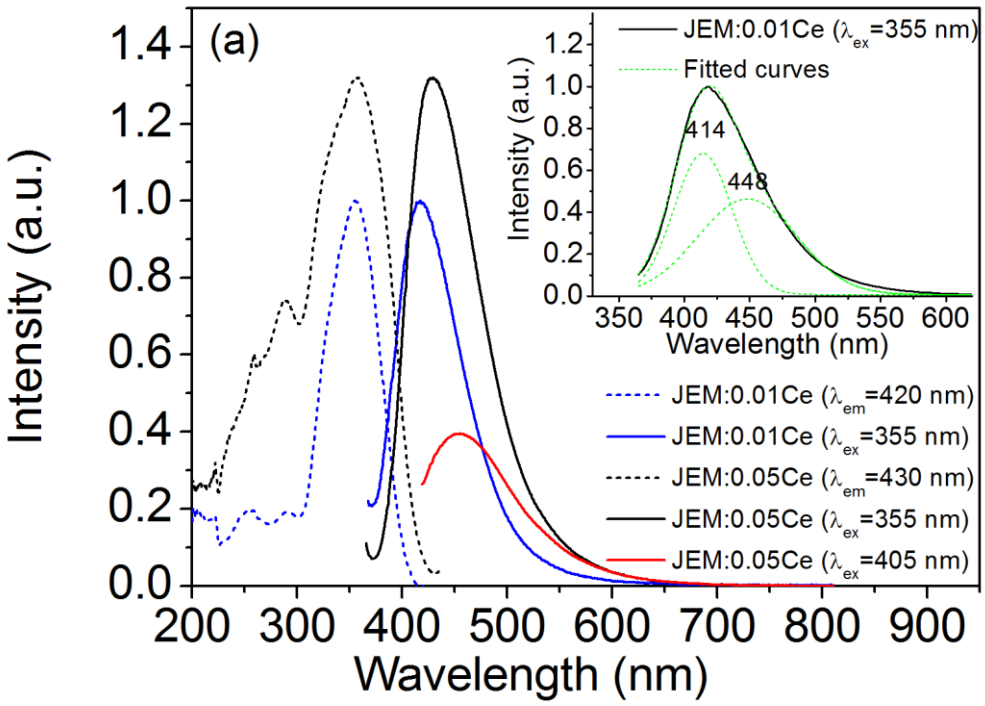

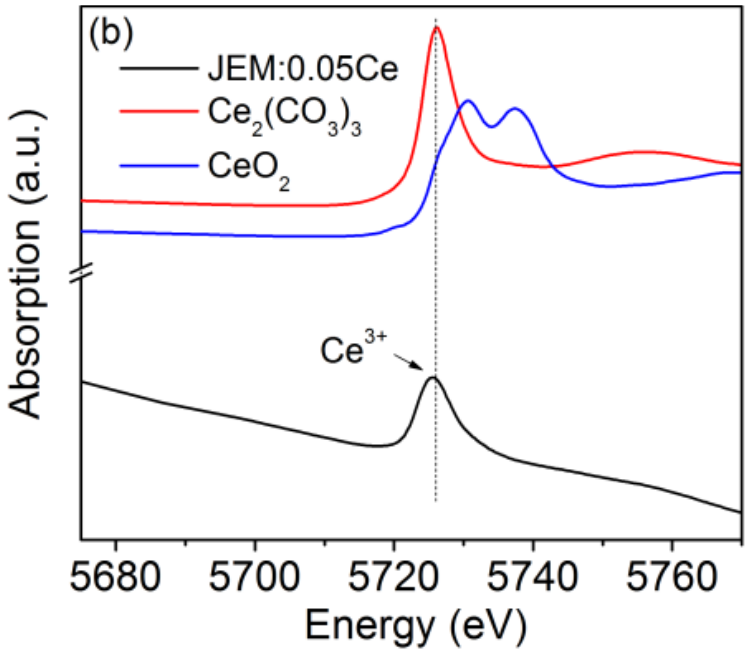

Figure 4.2 (a) Excitation spectra and emission spectra of 1% Ce and 5% Ce doped JEM phosphors. The fitted emission spectrum of JEM:0.01Ce phosphor after 355 nm excitation is shown as an inset. (b) Ce L_3 XANES spectra of JEM:0.05Ce phosphor and $Ce_2(CO_3)_3$, CeO_2 referenced samples for Ce^{3+} and Ce^{4+}, respectively.

4.3.3 Luminescence decay and redshift of JEM:0.01Ce phosphor

Figure 4.3 shows the luminescence decay of 1% Ce doped JEM phosphor when monitoring the 420 nm emission, exhibiting a linear decay curve. Since there is only one crystallographic site in JEM structure that can be occupied by Ce atoms, the decay curve can be fitted with single exponential decay, giving a short lifetime of 25.6 ns. Note however that for the JEM:Eu phosphor, the decay of the Eu^{2+} d-f emission is double exponential, indicating there are two different luminescence sites, as reported in our previous work[2]. This was attributed to different local environments caused by disorders in the structure. The luminescence from activator ions in different environments seems to be absent in JEM:Ce phosphor. This is also expressed in the width of the emission bands, as the Ce^{3+} d-f emission band is relatively narrow (74 nm), while the Eu^{2+} d-f emission is relatively broad (121 nm). The difference may be related to the difference in valence between Ce and Eu, requiring charge compensation for Eu substituted on a

La site. Also the difference in ionic radius may be a reason, as Ce^{3+} is very similar in size to La^{3+}, while Eu^{2+} is much larger.

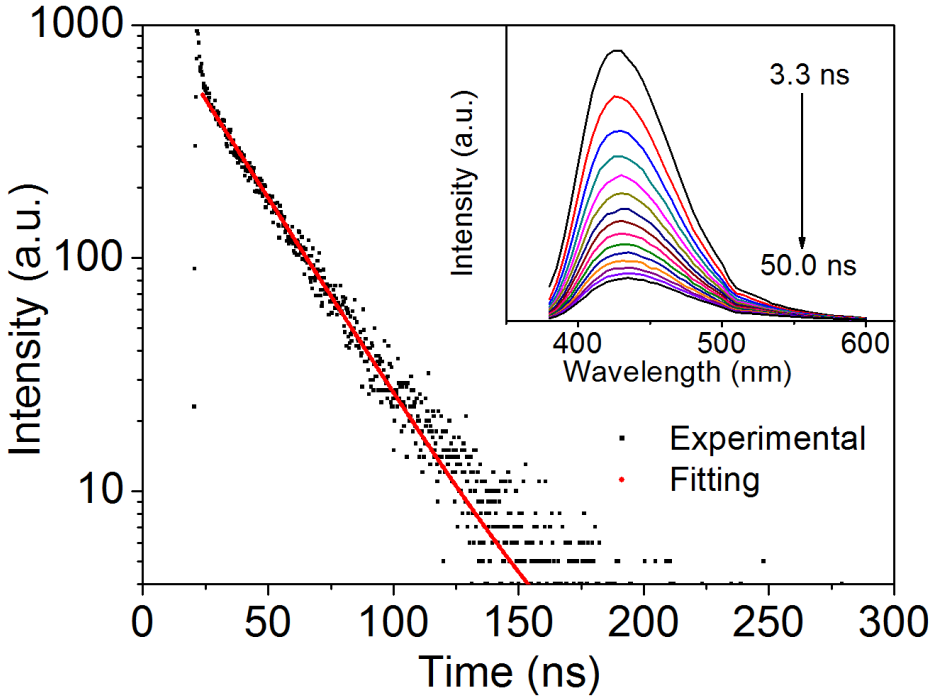

Figure 4.3 Luminescence decay curves and time-resolved photoluminescence emission spectra (inset) with an interval of 3.3 ns of 1% Ce doped JEM phosphor (λ_{ex} = 370 nm).

In order to check whether the Ce^{3+} and Eu^{2+} d-f emissions originate from Ce^{3+} and Eu^{2+} ions on similar crystallographic sites, the redshifts of the Ce^{3+} and Eu^{2+} d-f emission are compared. The redshift D(3+) of Ce^{3+} is defined as the energy difference between the lowest 4f-5d transition of the Ce^{3+} ion in a compound, and to the same transition in vacuum.[3] By fitting the excitation spectrum of a 1% Ce doped sample, see Figure 4.4, the lowest energy 4f-5d transition of Ce^{3+} in JEM (E_{fd} (Ce^{3+}, JEM)) can be estimated to be 3.44 eV (360 nm). Since the 4f-5d transition energy for Ce^{3+} ions in vacuum is 6.12 eV,[4] the redshift of Ce^{3+} can be calculated to be 2.68 eV.

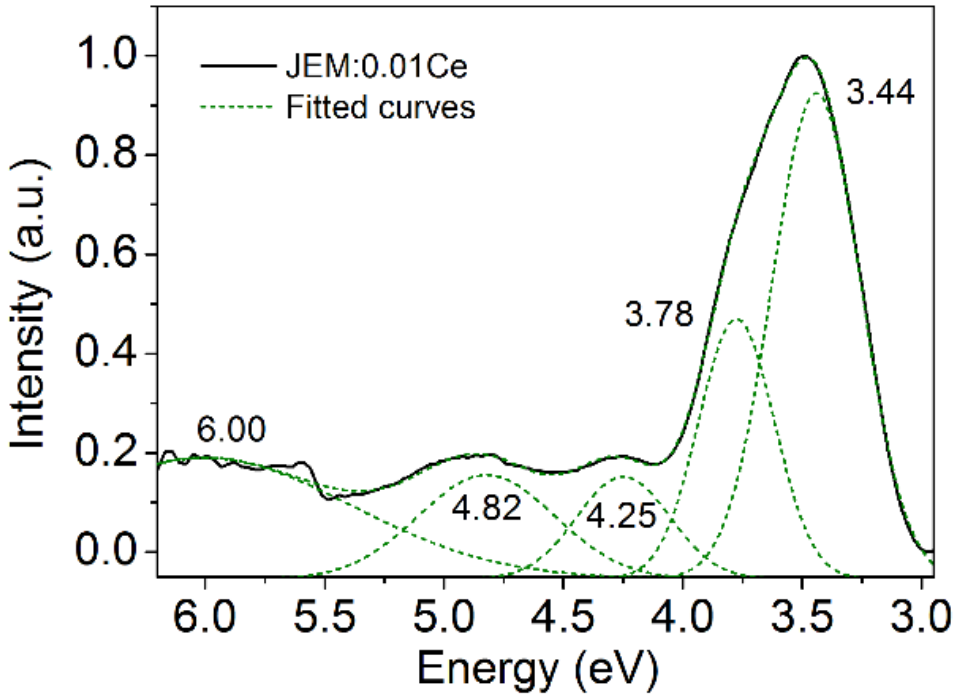

Figure 4.4 Excitation spectrum of JEM:0.01Ce phosphor monitoring 420 nm emission.

The excitation and emission spectra of JEM:0.01Eu, as I reported in our previous work[2], are shown in Figure 4.5 for comparison, together with the excitation and emission spectra of JEM:0.01Ce. Compared to the JEM:0.01Ce phosphor, the excitation and emission spectra of JEM:0.01Eu phosphor are much broader and the emission band is located at longer wavelength. The lowest energy of Eu^{2+} 4f-5d transition can be estimated to be 2.73 eV (455 nm) by taking the point at the low energy side where the excitation intensity has dropped to 15%.[5] So the redshift of Eu^{2+} observed from the excitation spectrum is 1.49 eV, since the 4f-5d transition energy of Eu^{2+} ions in vacuum is 4.22 eV.[4] Dorenbos[6] reported an empirical relation between the trivalent redshift D(3+) of Ce^{3+} and the corresponding divalent redshift D(2+) of Eu^{2+}:

$$D(2+) = 0.64\ D(3+) - 0.233 \qquad (1)$$

This relation holds if Ce^{3+} and Eu^{2+} are located in the same compound and in a similar crystallographic environment. Using the experimentally determined redshift of 1.49 eV for Eu^{2+}, it predicts an Ce^{3+} redshift in JEM of 2.69 eV. The experimental value of the Ce^{3+} redshift (2.68 eV) is thus in perfect agreement with the predicted value of 2.69 eV based on the Eu^{2+} 4f-5d transition. This confirms that Ce^{3+} and Eu^{2+} are in a similar crystallographic environment in the JEM structure.

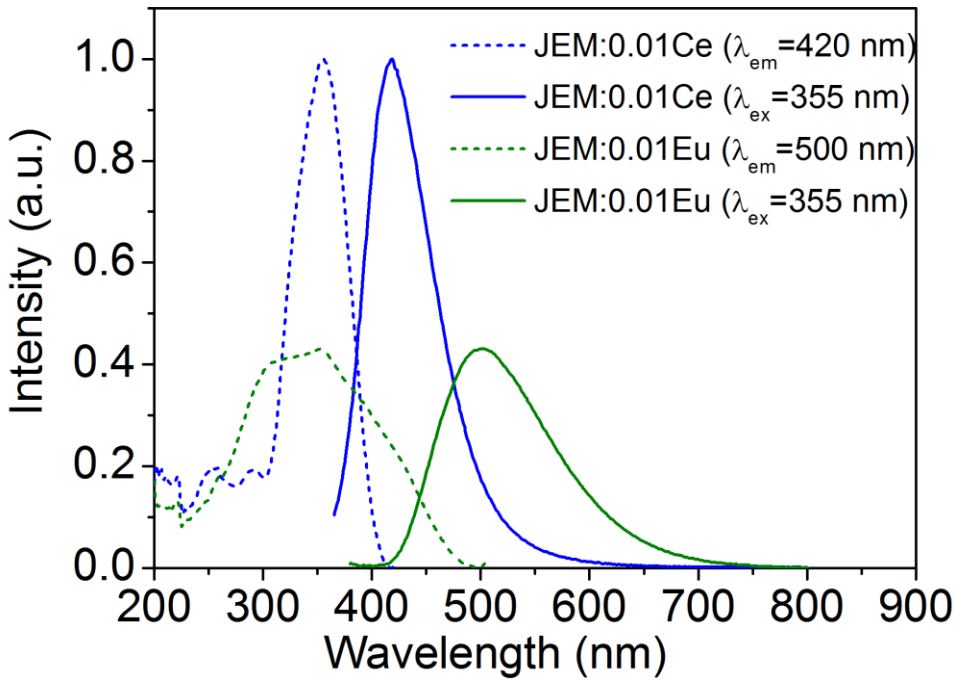

Figure 4.5 The excitation spectra and emission spectra of 1% Ce and 1%Eu doped JEM phosphors (The photoluminescence spectra of JEM:0.01Eu phosphor are from our previous work[2]).

4.3.4 Thermal quenching of JEM:Ce

Figure 4.6 shows the photoluminescence of 1% Ce doped JEM phosphor as function of temperature from 4 K to 573 K. No shift of emission band or any changes in the shape of emission spectra can be detected with increasing temperature. When the temperature is below 200 K, the luminescence intensity almost keeps constant. At room temperature, the luminescence intensity has only decreased 3% as compared to the intensity at 4 K. Above room temperature, the luminescence intensity decreases gradually with increasing temperature, with still 57% of the luminescence left at 573 K. This indicates that JEM:0.01Ce phosphor has a very good thermal stability.

The good thermal stability of the Ce doped JEM phosphor is in contrast to the thermal stability of Eu doped JEM. As shown in the inset of Figure 4.6, the luminescence of a 1% Eu doped JEM sample already starts to quench above 4 K, exhibiting a nearly linear relation between temperature and luminescence intensity. 44% of luminescence compared to that at 4 K has been

quenched when the temperature reaches room temperature, and there is only 14% of luminescence left at 573 K.

One of the mechanisms that may be responsible for thermal quenching of the 5d-4f emission, is the thermal ionization of the 5d electron to the conduction band.[7] If thermal ionization is indeed responsible for the thermal quenching, this would explain why Ce doped JEM has a much better thermal stability than Eu doped JEM. The lowest 5d state of Ce^{3+} namely is always lower in energy than the lowest 5d state of Eu^{2+} [8]. This places the lowest 5d state farther away from the bottom of the conduction band, giving it a higher energy barrier for thermal quenching.

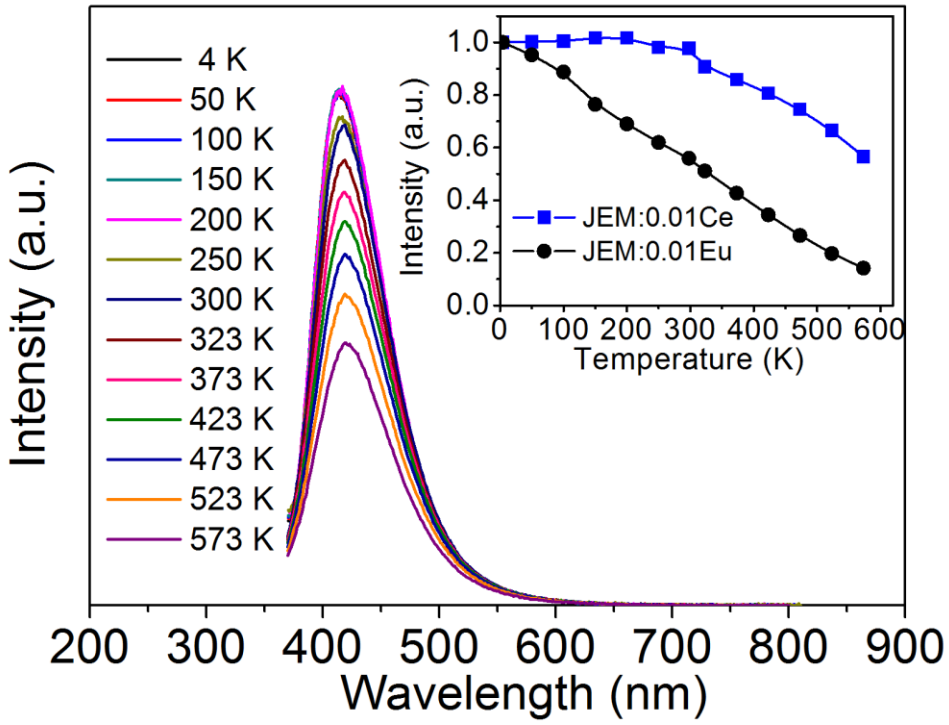

Figure 4.6 The emission spectra of JEM:0.01Ce phosphor at various temperatures (4K – 573 K) after 355 nm excitation, and the integrated emission intensity as a function of temperature (inset). The temperature dependency of luminescence for JEM:0.01Eu phosphor is included for comparison.

4.3.5 Optical properties of JEM:Yb and JEM:Sm phosphors

(1) JEM:Yb optical properties

1% and 5% Yb doped JEM samples have been prepared by solid-state reaction synthesis, also containing a trace amount (1.9%) of β-sialon impurity, when starting materials have a Si/Al ratio of 2.3 and an N/O ratio of 6.0. Figure 4.7a shows the diffuse reflectance spectra of non-doped and Yb doped JEM samples. The non-doped sample has strong absorption of UV light up to around 320 nm, which is attributed to band gap absorption. From the reflectance spectrum, an optical bandgap of 258 nm (4.81 eV) is deduced. This means that the band gap of this host material, including the exciton binding energy, is approximately 5.20 eV by using the method in ref.[9]. Compared to the non-doped sample, the 1% Yb doped sample also displays strong absorption between 320 and 600 nm. The absorption in Yb doped compounds can be related to either the electronic transition of Yb^{2+} from the 4f ground state to the 5d excited state, or the charge transfer (CT) transition of Yb^{3+}, or a combination of both. The CT transition is the result of the transfer of an electron from a neighboring anion towards Yb^{3+}.

As shown in Figure 4.7b, excitation of the 1% Yb doped sample at 365 nm results in a broad (FWHM = 160 nm) emission band centered around 580 nm, as well as a narrow emission line at 980 nm. The sharp line at 980 nm is very typical for the Yb^{3+} 4f-4f emission from the $^2F_{5/2}$ excited state to the $^2F_{7/2}$ ground state, indicating that at least a part of the Yb should be in the trivalent state. The emission band at 580 nm on the other hand, cannot be related to Yb^{3+} and is more typical for the 5d-4f emission of Yb^{2+}. This indicates that divalent and trivalent Yb ions coexist in JEM, and that the absorption between 320 and 600 nm in Figure 7a can be assigned to a combination of Yb^{2+} 4f-5d absorption and the Yb^{3+} CT transition. Similar cases of the coexistence of Yb^{2+} and Yb^{3+} have also been reported for several other (oxy-)nitridosilicate compounds, such as $CaAlSiN_3$:Yb[10]. Note that excitation of the 5% Yb doped sample gives a similar emission spectrum, but with much lower intensity.

The excitation spectrum (Figure 4.7b) monitoring the Yb^{2+} 5d-4f emission at 580 nm (2.14 eV) contains several bands centered at 320, 370, 425 and 480 nm. Such an excitation spectrum is again typical for the 4f-5d transitions of Yb^{2+}. The band at 480 nm (2.58 eV) is lowest in energy and is therefore assigned to the lowest spin-allowed transition from the $4f^{14}$ ground state to the lowest $4f^{13}[^2F_{7/2}]5d_1$ excited state. The excitation band centered at 320 nm (3.88 eV) is 1.30 eV higher in energy. This closely corresponds to the expected energy difference (~1.28 eV[11]) between the $4f^{13}[^2F_{7/2}]5d_1$ and $4f^{13}[^2F_{5/2}]5d_1$ states. The band at 320 nm can therefore be assigned

to the spin-allowed $4f^{14}$-$4f^{13}[^2F_{5/2}]5d_1$ transition. The other bands at 370 and 425 nm are related to the spin-allowed transition to higher energy crystal field split 5d states. The spin-forbidden 4f-5d transitions usually have very low intensity and can therefore not be observed. The lowest spin-forbidden level, from which the Yb^{2+} 5d-4f emission takes place, is about 0.24 eV lower in energy than the lowest spin-allowed band.[12] Therefore, the unresolved spin-forbidden band in the excitation spectrum of Yb^{2+} should be located around 530 nm (2.34 eV). From this, a Stokes shift of 0.20 eV for the Yb^{2+} emission in JEM can be derived.

In the excitation spectrum of the 980 nm emission (Figure 4.7b), a broad excitation band is observed that is composed of at least two separate bands, of which the peaks are located at 365 nm (3.40 eV) and 416 nm (2.98 eV). As the bands give rise to Yb^{3+} 4f-4f emission, they can most likely be assigned as Yb^{3+} charge transfer (CT) transitions due to the transfer of an electron from a neighboring anion (O^{2-} or N^{3-}) towards Yb^{3+}. These Yb^{3+} CT transitions have also given rise to Yb^{3+} 4f-4f emission in other nitridosilicate compounds, such as $CaAlSiN_3$:Yb[10]. It should however be noted that, due to the coexistence of Yb^{2+} in the sample, energy transfer may occur from Yb^{2+} to Yb^{3+}, meaning that Yb^{2+} 4f-5d absorption gives rise to Yb^{3+} 4f-4f emission. This type of energy transfer is well known and has for example been reported in CaF_2[13]. Therefore, the excitation spectrum of the 980 nm emission may partly contain the Yb^{2+} 4f-5d absorption bands, making it difficult to assign the exact location of the Yb^{3+} CT band based on the excitation spectrum. This will be further discussed in section 6.

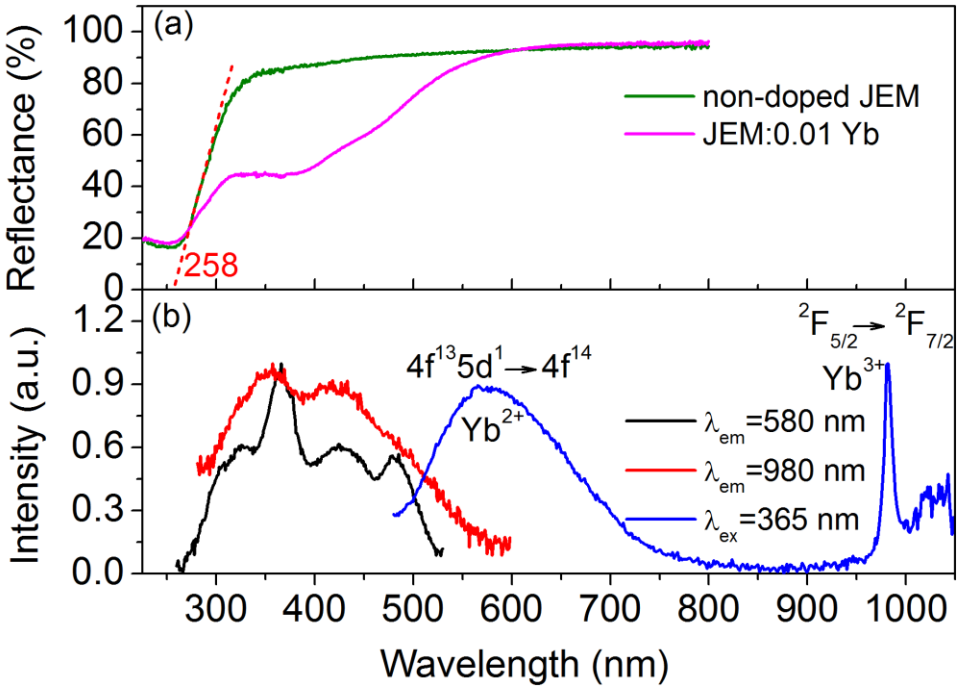

Figure 4.7 (a) Diffuse reflectance spectra of non-doped and 1% Yb doped JEM. (b) Photoluminescence spectra of JEM:0.01Yb phosphor.

The temperature dependency of the Yb^{2+} 5d-4f emission is shown in Figure 4.8. Between 4 K and 100 K the emission intensity is almost constant. Above 100 K the emission intensity starts to drop, falling with about 50% around 350 K. At 573 K only 20% of the emission intensity remains. The Yb^{2+} d-f emission is thus less temperature stable than the Ce^{3+} d-f emission (Figure 4.6). As compared to the Eu^{2+} d-f emission, the temperature at which 50% of the Yb^{2+} d-f emission has quenched is similar. The main difference as compared to Eu^{2+} is that Eu^{2+} has an abnormal nearly linear quenching behavior starting at 4 K, while for Yb^{2+} the emission starts to drop only above 100 K.

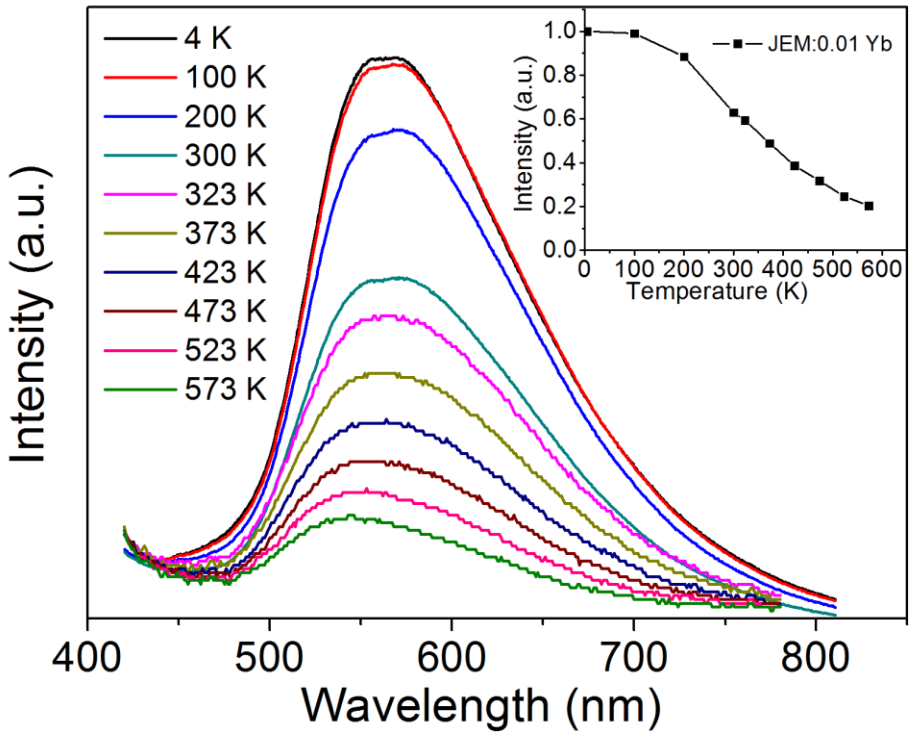

Figure 4.8. Temperature dependency of emission spectra and luminescence intensity (inset) of JEM:0.01Yb phosphor after 365 nm excitation.

(2) JEM:Sm optical properties

The series of JEM:xSm (x = 0.01, 0.03, 0.05) samples have been prepared with a z value of 1.12. A small amount of β-sialon (< 2%) impurity phase can be detected. Figure 4.9a represents the diffuse reflectance spectra of JEM:xSm (x = 0.01, 0.03, 0.05) samples. Compared to the non-doped sample, the Sm doped sample shows a lower reflectance between 280 and 800 nm, due to the presence of several strong absorption bands. The broad band absorption in Sm doped samples can be due to either Sm^{2+} 4f-5d transitions or to the charge transfer (CT) transitions from an anion to Sm^{3+}. The higher concentrated samples show a similar reflectance behavior; the absorption bands just become stronger with increasing Sm concentration.

The emission and excitation spectra of the Sm doped samples are shown in Figure 4.9b. After 310 nm excitation, the emission spectra show emission lines with maxima at 561 nm, 599 nm, 646 nm, and 704 nm. These emission lines can be ascribed to $^4G_{5/2}$ to ^6H_J (J = 5/2, 7/2, 9/2 and 11/2) transitions of Sm^{3+}, indicating that at least a part of the Sm is present in the trivalent state.

Monitoring the 646 nm emission shows several weak absorption lines centered around 347 nm, 363 nm, 379 nm, 409 nm, 426 nm, and 475 nm, which can be assigned to absorptions from the Sm^{3+} $^6H_{5/2}$ ground state to the excited 4f states of Sm^{3+}. Apart from the 4f-4f absorption lines, a broad excitation band (FWHM = 73 nm) centered at 310 nm (4.00 eV) is also present in the excitation spectra. This band could most likely be attributed to the Sm^{3+} charge transfer (CT) transitions, as will be further commented on in section 6. The CT absorption can also be seen in the reflectance spectrum of Figure 4.9a between 270 and 400 nm. However, as was mentioned before, there are also other strong absorption bands between 400 and 800 nm. Exciting the samples with these wavelengths does not result in any luminescence at all, even if the samples are cooled down to 4 K. The absorption bands could be assigned to Sm^{2+} 4f-5d transitions, indicating the presence of Sm^{2+} in coexistence with Sm^{3+} in the sample. This will also be further discussed in the next section.

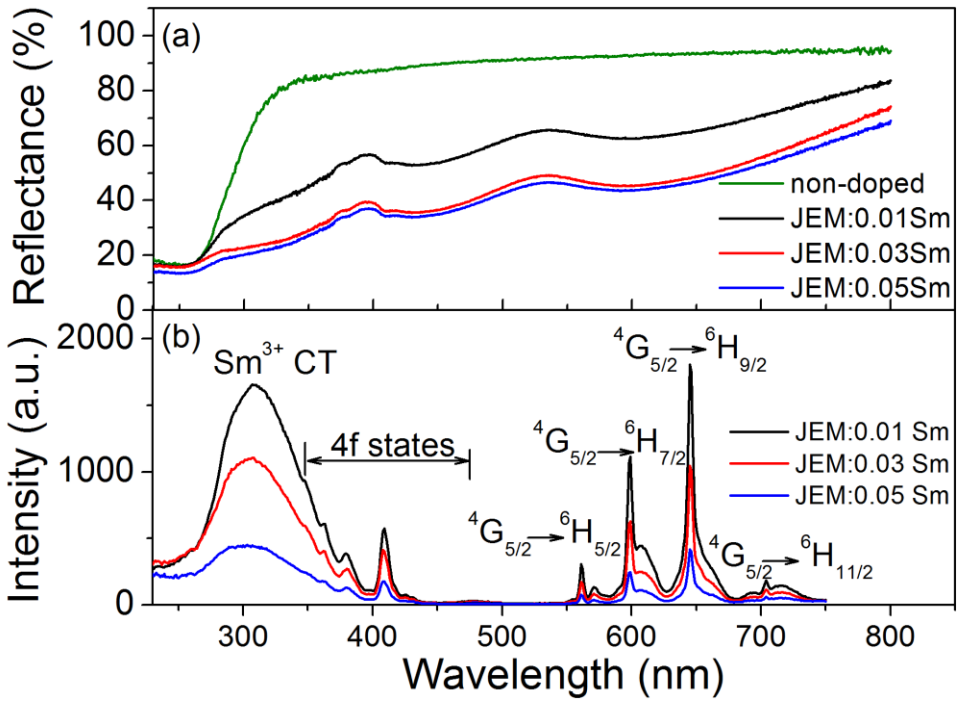

Figure 4.9 (a) Diffuse reflectance spectra of JEM:xSm samples (x = 0, 0.01, 0.03, 0.05) and (b) photoluminescence emission (λ_{ex} = 310 nm) and excitation (λ_{em} = 646 nm) spectra of Sm doped JEM phosphors.

4.3.6 Energy level locations of Ce, Eu, Sm and Yb in JEM

In the previous section, several absorption bands in the Yb and Sm doped samples were attributed to CT transitions of Yb^{3+} and Sm^{3+} respectively. In order to get a better understanding whether this assignment is correct and consistent with the optical data obtained for JEM:Eu and JEM:Ce samples, the positions of the energy levels of the lanthanide impurities are determined with respect to the JEM valence band. As illustrated in Figure 4.10, the energy $\Delta E(Ce^{3+})$ between the Ce^{3+} 5d level and the bottom of the conduction band is given by the equation:

$$\Delta E(Ce^{3+}) = E_g - E_{df(Ce^{3+})} - E_{VB\text{-}4f(Ce^{3+})} \qquad (2)$$

Where E_g is the bandgap (5.20 eV) and $E_{df(Ce^{3+})}$ the energy of the Ce^{3+} 5d-4f emission (3.00 eV). $E_{VB\text{-}4f(Ce^{3+})}$ is the energy difference between the top of the valence band and the 4f ground state of Ce^{3+}. From the thermal quenching data of Ce^{3+} in Figure 4.6, the energy barrier for the thermal quenching of the Ce^{3+} emission can be estimated to be 0.92 eV:[7] ($T_{50\%}$/680 eV = 625/680 eV = 0.92 eV). If, as discussed before, the thermal quenching is the result of thermal ionization towards the conduction band, then the energy $\Delta E(Ce^{3+})$ between the 5d level and the conduction band should be about 0.92 eV. Using equation (2) this means that $E_{VB\text{-}4f(Ce^{3+})}$ is about 1.28 eV.

By using the models of the energy levels of the lanthanides as obtained by Dorenbos,[4] now it is possible to estimate the energy levels of the other lanthanide ions within the JEM host. The models have been successfully applied in many halide, chalcogenide and nitride compounds. Examples for silicon-based (oxy)nitride compounds are $M_2Si_5N_8$ (M = Ca, Sr, Ba),[14] $LaSi_3N_5$,[15] $CaAlSiN_3$,[16], $CaSi_2O_2N_2$[17] and Ca-α-sialon.[18] It is known that the 4f ground state of Eu^{3+} is 5.24 eV lower in energy than the 4f ground state Ce^{3+},[4] which places the Eu^{3+} 4f ground state at about -3.96 eV below the top of the valence band. So, if the energy difference U between the 4f ground states of Eu^{2+} and Eu^{3+} is known, the energy between the top of the valence band and the 4f ground state of Eu^{2+} can be determined (see also Figure 4.10).

The energy difference U between the 4f ground states of Eu^{2+} and Eu^{3+} can be determined via the chemical and centroid shift models.[4] The energy difference U is also called the Coulomb repulsion energy and it is related to the centroid shift of Ce^{3+} as follows:[19]

$$U = 5.44 + 2.834\, e^{-\varepsilon_c/2.2} \qquad (3)$$

Here is ε_c the centroid shift given in eV of Ce^{3+}. As shown in Figure 4.4, the excitation spectrum of JEM:0.01 Ce sample can be fitted with four 5d bands located at 4.82, 4.25, 3.78 and 3.44 eV, respectively, while the band fitted at 6.00 eV is attributed to the bandgap absorption. The fifth 5d band is probably hidden by the other 5d bands. So the centroid shift ε_c of the 5d configuration of Ce^{3+} in JEM can be estimated to be 1.89 eV using the following formula:[4]

$$\varepsilon_c = 6.35 - \frac{1}{4}\sum_{i=1}^{4} E_{f\,d_i}(Ce^{3+}) \qquad (4)$$

Here 6.35 means the 4f-5d energy for the free Ce^{3+} ion in eV, and $E_{f\,d_i}(Ce^{3+})$ are the energies of the 4f-5d transitions of Ce^{3+}. From equation (4) it follows that the centroid shift of the Ce^{3+} 5d level is about 2.28 eV, and from equation (3) it follows that the Coulomb repulsion U is 6.45 eV. Note that the Coulomb repulsion is the same as in $LaSiO_2N$,[4, 20] which is logical as that is also a lanthanum oxy-nitridosilicate.

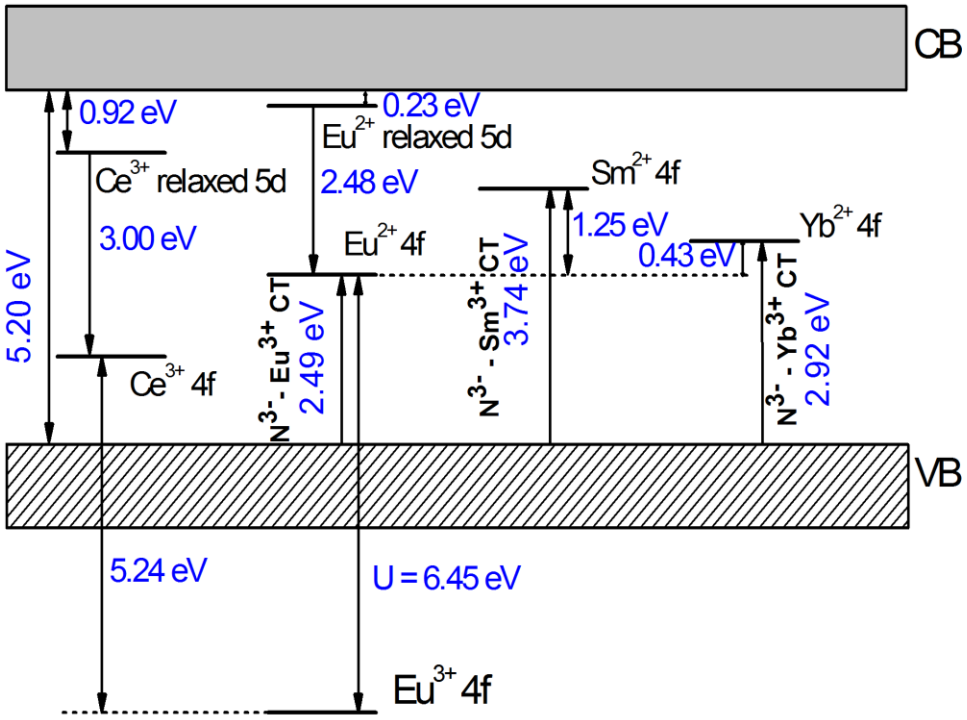

Figure 4.10 Schematic energy scheme showing the approximate location of Eu^{2+}, Sm^{2+}, Yb^{2+}, Ce^{3+} and Eu^{3+} lanthanide impurity 4f and 5d levels in JEM (Note that the width of conduction band CB and valence band VB has no physical meaning).

We now know that the energy difference between the Eu^{2+} and Eu^{3+} 4f ground states is 6.45 eV and that the Eu^{3+} 4f ground state is -3.96 eV below the top of the valence band. This means that the 4f ground state of Eu^{2+} is 2.49 eV above the top of the valence band. Using the Eu^{2+} 5d-4f emission (2.48 eV) this places the Eu^{2+} 5d relaxed state at around 0.23 eV below the bottom of the conduction band, as illustrated in Figure 4.10. The relaxed 5d state of Eu^{2+} is thus indeed much closer to the conduction band than the 5d of Ce^{3+}, as discussed before and its close proximity to the bottom of conduction band is in good agreement with the fast thermal quenching of the Eu^{2+} 5d-4f emission.

The 4f ground state of Yb^{2+} is always 0.43 eV higher in energy than the 4f ground state of Eu^{2+}.[4] This places the 4f ground state of Yb^{2+} at around 2.92 eV above the top of the valence band. As the energy of the CT transition of Yb^{3+} should be equal to the energy difference between the top of the valence band and the 4f ground state of Yb^{2+}, this means that the CT of Yb^{3+} would be expected around 2.92 eV (425 nm). This is in good agreement with the position of the band centered at 416 nm (2.98 eV) in the excitation spectrum of the 980 nm emission (see Figure 4.7b), making it likely that this band contains CT transition of Yb^{3+}. From the CT transition of Yb^{3+}, as discussed above, we know that the energy between the top of the valence band and the 4f ground state of Yb^{2+} is 2.98 eV. Since the electronegativity of oxygen is higher than that of nitrogen, the energy of the charge transfer transition from O^{2-} to Yb^{3+} should be higher than from N^{3-} to Yb^{3+}. The band observed at higher energy, i.e. at 365 nm (3.40 eV), may contain the CT transitions from O^{2-} to Yb^{3+}.

The 4f ground state of Sm^{2+} is usually 1.25 eV higher in energy than that of Eu^{2+}.[4] Therefore, the charge transfer transition from N^{3-} to Sm^{3+} can be predicted to be around 3.74 eV (332 nm). This is relatively close to the band observed at 4.00 eV (310 nm) in the excitation spectrum of the Sm^{3+} 4f-4f emission (Figure 4.9b), confirming that this band may indeed be the CT band of Sm^{3+}. Local coordination effects, involvement of O^{2-} to Sm^{3+} charge transfer transitions, as well as small errors in the estimated values may explain why there is a small disagreement between the predicted and observed values.

Based on the optical properties of Ce, Eu, Yb and Sm doped JEM phosphors presented above, the energy levels of Ce, Eu, Yb and Sm have been established within the JEM host (Figure 4.10). A complete energy level scheme can now constructed, showing the lowest 4f and unrelaxed 5d

levels of all trivalent and divalent lanthanide ions with respect to the top of the valence band, by using the theories of Dorenbos that relate the energy levels of the different lanthanides to each other.[21-22] The resulting energy level scheme is shown in Figure 4.11. Note here that the positions of the energy levels should not be taken too literally as there is some uncertainty (around 0.2-0.3 eV) in their exact location. These uncertainties are the result of local coordination effects around the lanthanide impurities that the models do not take into account, as well as estimations that have been done based on the available optical data.

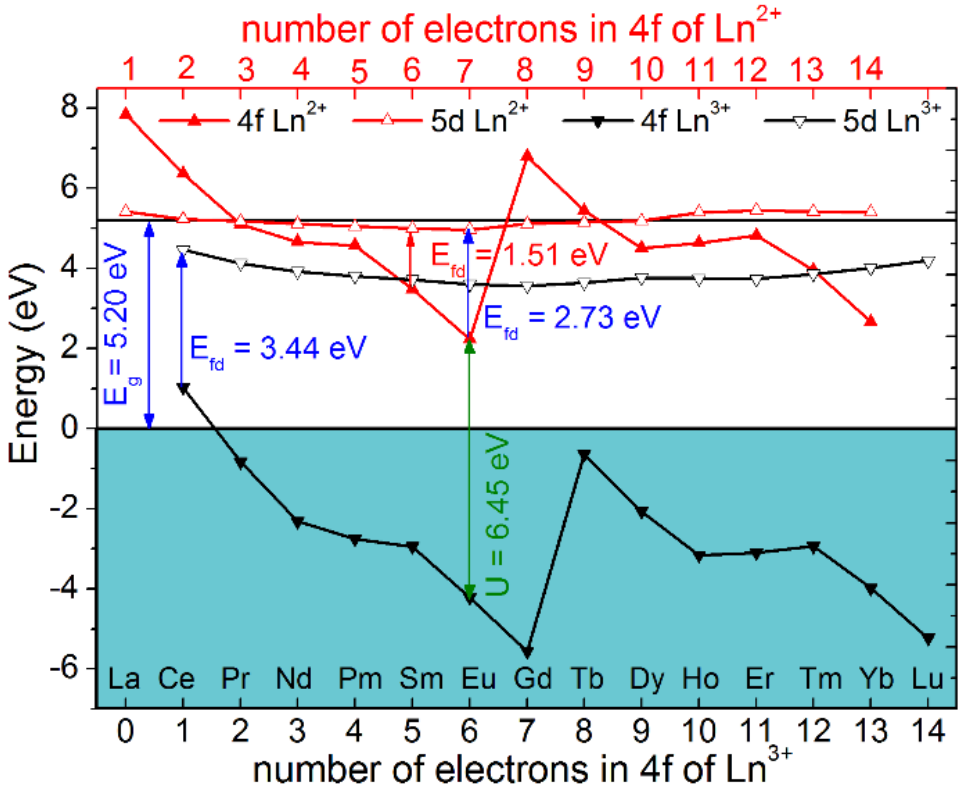

Figure 4.11 Energy level scheme, showing the approximate positions of the 4f ground states and lowest unrelaxed 5d states of the divalent and trivalent lanthanide ions with respect to the top of the valence band of JEM.

Based on the diffuse reflectance spectra of the Sm doped samples (Figure 4.9a), it was suggested that the absorption bands observed between 400 and 800 nm may be attributed to Sm^{2+} 4f-5d transitions, indicating the presence of Sm^{2+} in the samples in coexistence with Sm^{3+}. Using the energy scheme presented in Figure 4.11, this assignment can be verified. The scheme

predicts the lowest energy Sm^{2+} 4f-5d transition at 1.51 eV (821 nm). This nicely agrees with the diffuse reflectance spectra of JEM:Sm phosphors as they suggest that the absorption bands extend up to slightly above 800 nm, confirming that the bands may be due to Sm^{2+} 4f-5d transitions. The absence of any luminescence from Sm^{2+} after excitation in these bands can be attributed to non-radiative relaxation from the 5d to the lower 4f states of Sm^{2+} considering the low energy of the Sm^{2+} 4f-5d transition.

The energy scheme can also be used to comment on the divalent and trivalent states of lanthanide ions as dopants in JEM. The Fermi energy (E_F) is approximately one half of the band gap energy in pure compounds.[18] The ground state of Eu^{2+} is more close to the valence band than to the conduction band, making divalent Eu more stable in JEM than trivalent Eu. The ground states of Yb^{2+} and Sm^{2+} are higher in energy, but still more than 1 eV below the bottom of the conduction band, resulting in the presence of Yb and Sm in both the divalent and the trivalent state, when the synthesis is carried out under reducing conditions. The other ground states are closer to the conduction band, or even inside (as for Ce), making the presence of divalent ions less likely.

4.4 Conclusions

Nearly single phase JEM:Ce doped phosphors have been obtained via a solid-state reaction at 1850 °C for 2 hours by using La_2O_3, LaN, Si_3N_4, AlN and CeO_2 as starting materials. JEM:Ce phosphors can be excited by UV or near UV light and emit a blue luminescence. JEM:0.05Ce phosphor shows a Ce^{3+} 5d-4f emission band with a FWHM of 81 nm centered at 430 nm, after the excitation of 355 nm light; and a high internal quantum efficiency up to 75% is achieved. The XANES results further confirm that all Ce is in the trivalent state. The luminescence decay of the JEM:Ce phosphors shows a single exponential behavior, coinciding with the single crystallographic site for Ce. JEM:Ce phosphors have better quantum efficiency and thermal stability than JEM:Eu phosphors, because the lowest 5d level of Ce^{3+} is much farther from the bottom of the conduction band than that the 5d level of Eu^{2+} is. This gives a larger barrier for thermal quenching of the Ce^{3+} 5d-4f emission, due to the higher energy needed for the thermal ionization.

Based on optical data it was concluded that JEM:Yb and JEM:Sm phosphors contain both divalent and trivalent lanthanide ions. The trivalent ions give typical 4f-4f emission lines after charge transfer (CT) band excitation. By constructing an energy level scheme that shows the positions of the 4f and 5d levels of the lanthanides with respect to the valence band of JEM, it was shown that the positions of the CT bands observed in the excitation spectra are in good agreement with the optical data of the JEM:Ce and JEM:Eu samples. JEM:Yb phosphors show also Yb^{2+} d-f emission next to the Yb^{3+} f-f emission. For the JEM:Sm phosphors only Sm^{3+} f-f emission is observed, which agrees well with the prediction of the energy level scheme.

The method to construct the energy level scheme can also be applied to other phosphors, being very helpful for the interpretation of the optical properties of the lanthanide doped materials, as it was used in this work to elucidate thermal quenching mechanisms, valencies and charge transfer transitions. In addition, the scheme also allows for the prediction of the energy level positions of the other lanthanides in the same compound, which is for example useful for afterglow applications. If the ground state of a divalent lanthanide ion is located below the conduction band, as predicted for Dy and Ho in the JEM structure, the Dy^{3+} and Ho^{3+} can act as electron traps. This means that Dy^{3+} and Ho^{3+} may be used as co-dopants to enhance afterglow emission.

4.5 References

(1) Takahashi, K.; Hirosaki, N.; Xie, R.-J.; Harada, M.; Yoshimura, K.-i.; Tomomura, Y. Luminescence Properties of Blue $La_{1-x}Ce_xAl_z(Si_{6-z}Al_z)(N_{10-z}O_z)$ ($z \sim 1$) Oxynitride Phosphors and Their Application in White Light-Emitting Diode *Applied Physics Letters* **2007**, *91*, 091923.

(2) Wang, C.-Y.; Takeda, T.; ten Kate, O. M.; Xie, R.-J.; Takahashi, K.; Hirosaki, N. Synthesis and Photoluminescence Properties of a Phase Pure Green-Emitting Eu Doped JEM Sialon ($LaSi_{6-z}Al_{1+z}N_{10-z}O_z$, $z \sim 1$) Phosphor with a Large Red-Shift of Emission and Unusual Thermal Quenching Behavior *Journal of Materials Chemistry C* **2016**, *4*, 10358-10366.

(3) Dorenbos, P. The $4f^n \leftrightarrow 4f^{n-1}5d$ Transitions of the Trivalent Lanthanides in Halogenides and Chalcogenides *Journal of Luminescence* **2000**, *91*, 91-106.

(4) Dorenbos, P. Ce^{3+} 5d-Centroid Shift and Vacuum Referred 4f-Electron Binding Energies of All Lanthanide Impurities in 150 Different Compounds *Journal of Luminescence* **2013**, *135*, 93-104.

(5) Dorenbos, P. Energy of the First $4f^7 \rightarrow 4f^6 5d$ Transition of Eu^{2+} in Inorganic Compounds *Journal of Luminescence* **2003**, *104*, 239-260.

(6) Dorenbos, P. Relation between Eu^{2+} and Ce^{3+} f↔d-Transition Energies in Inorganic Compounds *Journal of Physics: Condensed Matter* **2003**, *15*, 4797.

(7) Dorenbos, P. Thermal Quenching of Eu^{2+} 5d–4f Luminescence in Inorganic Compounds *Journal of Physics: Condensed Matter* **2005**, *17*, 8103.

(8) Dorenbos, P. A Review on How Lanthanide Impurity Levels Change with Chemistry and Structure of Inorganic Compounds *ECS Journal of Solid State Science and Technology* **2013**, *2*, R3001-R3011.

(9) Dorenbos, P. The Eu^{3+} Charge Transfer Energy and the Relation with the Band Gap of Compounds *Journal of Luminescence* **2005**, *111*, 89-104.

(10) Zhang, Z.; Otmar, M.; Delsing, A. C.; Stevens, M. J.; Zhao, J.; Notten, P. H.; Dorenbos, P.; Hintzen, H. T. Photoluminescence Properties of Yb^{2+} in $CaAlSiN_3$ as a Novel Red-Emitting Phosphor for White LEDs *Journal of Materials Chemistry* **2012**, *22*, 23871-23876.

(11) Dorenbos, P. f→ d Transition Energies of Divalent Lanthanides in Inorganic Compounds *Journal of Physics: Condensed Matter* **2003**, *15*, 575.

(12) Dorenbos, P. Anomalous Luminescence of Eu^{2+} and Yb^{2+} in Inorganic Compounds *Journal of Physics: Condensed Matter* **2003**, *15*, 2645.

(13) Kaczmarek, S. M.; Tsuboi, T.; Ito, M.; Boulon, G.; Leniec, G. Optical Study of Yb^{3+}/Yb^{2+} Conversion in CaF_2 Crystals *Journal of Physics: Condensed Matter* **2005**, *17*, 3771.

(14) Otmar, M. Ten Kate; Zhang, Z.; Dorenbos, P.; Hintzen, H. T.; Van der Kolk, E. 4f and 5d Energy Levels of the Divalent and Trivalent Lanthanide Ions in $M_2Si_5N_8$ (M= Ca, Sr, Ba) *Journal of Solid State Chemistry* **2013**, *197*, 209-217.

(15) Otmar, M. Ten Kate; Hintzen, H. T.; Dorenbos, P.; van der Kolk, E. Yb^{3+} Doped $LaSi_3N_5$ and YSi_3N_5 with Low Energy Charge Transfer for near-Infrared Light-Emitting Diode and Solar Cell Application *Journal of Materials Chemistry* **2011**, *21*, 18289-18294.

(16) Zhang, Z.; Otmar, M.; Delsing, A.; van der Kolk, E.; Notten, P. H.; Dorenbos, P.; Zhao, J.; Hintzen, H. T. Photoluminescence Properties and Energy Level Locations of RE^{3+}(RE= Pr, Sm, Tb, Tb/Ce) in $CaAlSiN_3$ Phosphors *Journal of Materials Chemistry* **2012**, *22*, 9813-9820.

(17) Yang, L.; Xu, X.; Hao, L.; Yang, X.; Tang, J.; Xie, R. Photoluminescence of Lanthanide-Doped $CaSi_2O_2N_2$ Phosphors and the Energy-Level Diagram of Lanthanide Ions in $CaSi_2O_2N_2$ *Optical Materials* **2011**, *33*, 1695-1699.

(18) Srivastava, A.; Dorenbos, P. Charge Transfer Transitions and Location of the Rare Earth Ion Energy Levels in Ca-α-Sialon *Journal of Luminescence* **2009**, *129*, 634-638.

(19) Dorenbos, P. Lanthanide 4f-Electron Binding Energies and the Nephelauxetic Effect in Wide Band Gap Compounds *Journal of Luminescence* **2013**, *136*, 122-129.

(20) Long, H.; Xue-Wen, X.; Zun-Ming, L.; Ying, F.; Yang-Xian, L.; Cheng-Chun, T. Luminescence of Ce^{3+} in Lanthanum Silicon Oxynitride *Chinese Physics B* **2010**, *19*, 127807.

(21) Dorenbos, P. Systematic Behaviour in Trivalent Lanthanide Charge Transfer Energies *Journal of Physics: Condensed Matter* **2003**, *15*, 8417.

(22) Dorenbos, P. Lanthanide Charge Transfer Energies and Related Luminescence, Charge Carrier Trapping, and Redox Phenomena *Journal of Alloys and Compounds* **2009**, *488*, 568-573.

Chapter 5 Ce doped $La_3Si_{6.5}Al_{1.5}N_{9.5}O_{5.5}$, a rare highly efficient blue-emitting phosphor at short wavelength toward high color rendering white LED application

The content of this chapter has been published as Chun-Yun Wang, Takashi Takeda, Otmar Melvin ten Kate, Masataka Tansho, Kenzo Deguchi, Kohsei Takahashi, Rong-Jun Xie, Tadashi Shimizu, Naoto Hirosaki. ACS Applied Materials & Interfaces, DOI:10.1021/acsami.7b03909.

5.1 Introduction

The so called Al-containing La N(ew)-phase[1] was initially assigned with an incorrect chemical composition of $La_3Si_6Al_2O_6N_9$ and a wrong structure model in 1992, because of the unavailability of single crystals and the difficulty to select the correct unit cell from the framework superstructure along the c-axis based on only powder X-ray diffraction data.[2] In 2001, Grins et al[2] proposed the right chemical composition of $La_3Si_{8-x}Al_xN_{11-x}O_{4+x}$ ($x \approx 1.5$) and analyzed the crystal structure by using single-crystal X-ray and time-of-flight neutron powder diffraction data. For nitride and oxynitride phosphors with 5d-4f emission, the coordination environment of Si and Al usually has a great effect on photoluminescence properties; partial substitution of Si-N by Al-O is a general way to tune photoluminescence spectra.[3,4,5] Concerning the La N-phase without Al ($La_3Si_8O_4N_{11}$), the local structures have been investigated with ^{29}Si, ^{27}Al, ^{17}O and ^{15}N nuclear magnetic resonance (NMR) spectra.[1, 6, 7] However, the coordination environments of ^{29}Si and ^{27}Al for $La_3Si_{6.5}Al_{1.5}N_{9.5}O_{5.5}$ phase are still not clear, due to unavailability of a phase pure sample. In addition, no report on lanthanide ions doped Al-containing La N(ew)-phase $La_3Si_{6.5}Al_{1.5}N_{9.5}O_{5.5}$ has been published so far.

For this work, I synthesized phase pure non-doped and Ce doped $La_3Si_{6.5}Al_{1.5}N_{9.5}O_{5.5}$ samples by the solid-state reaction method. The photoluminescence properties of Ce doped $La_3Si_{6.5}Al_{1.5}N_{9.5}O_{5.5}$ phosphor are reported. By changing Ce concentration (y value) and the Al content (x value), the effects on lattice parameters, photoluminescence properties including photoluminescence spectra, quantum efficiency, thermal quenching and decay behavior will be presented for the series of $La_{3(1-y)}Si_{6.5}Al_{1.5}N_{9.5}O_{5.5}$:3yCe (y = 0.005-0.50) and $La_{2.85}Si_{8-x}Al_xN_{11-x}O_{4+x}$:0.15Ce (x = 0-2.0) phosphors, respectively. The local structures of ^{29}Si and ^{27}Al for $La_3Si_{6.5}Al_{1.5}N_{9.5}O_{5.5}$ sample have also been investigated.

5.2 Experimental section

5.2.1 Sample preparation

Non-doped $La_3Si_{6.5}Al_{1.5}N_{9.5}O_{5.5}$ and Ce doped $La_{3(1-y)}Si_{8-x}Al_xN_{11-x}O_{4+x}$:3yCe (x = 0.5-2.0, y = 0.005-0.50) phosphor powder samples were synthesized with a solid-state reaction method. The starting materials used include La_2O_3 (Shin-Etsu Chemical Co.), α-Si_3N_4 (SN-E10, Ube Industries), SiO_2 (Kojundo Chemical Laboratory Co. Ltd, Tokyo, Japan), AlN (Tokuyama, E-grade) and CeO_2 (Shin-Etsu Chemical Co., Ltd., Japan). The powders were mixed with designed chemical compositions and then packaged in boron nitride crucibles in air. Without Al samples ($La_3Si_8O_4N_{11}$ and $La_3Si_8O_4N_{11}$:Ce) were mixed by adding additional LaN without SiO_2 in a glove box filled with highly pure nitrogen gas. All of the samples were fired in a nitrogen gas-pressure sintering furnace (Fujidempa Kogyo Co. Ltd., Osaka, Japan) at 1800 °C for 2 hours. After heating, the sintered samples were finely ground with a mortar for further characterization.

5.2.2 Characterization

The measurements of X-ray diffraction, photoluminescence spectra, diffuse reflectance spectra, temperature dependent luminescence spectra, quantum efficiency and luminescence decay were carried out according to the description in the sections of 2.2 and 2.3 in Chapter 2. The temperature-dependent luminescence decay curves were recorded in combination with the same type of cryostat and heating cell that were used for the temperature dependency emission spectra measurement. A 370 nm spectraLED (Horiba) was used as the excitation source for the afterglow measurements.

The high resolution ^{29}Si and ^{27}Al solid state Nuclear Magnetic Resonance (NMR) experiments were carried out on finely ground powder of non-doped $La_3Si_{6.5}Al_{1.5}N_{9.5}O_{5.5}$. The ^{29}Si magic-angle spinning (MAS) NMR spectrum was collected at a magnetic field of 11.75 T (JEOL RESONANCE ECA 500 spectrometer) corresponding to the Larmor frequency 99.4 MHz for ^{29}Si. A standard 4 mm Chemagnetics MAS probe with a MAS frequency of 10 kHz was used. The single pulse sequence with 3.6 μs, which is π/2 pulse, and a relaxation delay of 5,400 s were required. ^{29}Si MAS NMR spectrum was referenced to the ^{29}Si shift of tetramethylsilane (TMS). The ^{27}Al one dimensional magic-angle spinning (MAS) experiment and ^{27}Al two dimensional triple-quantum magic-angle spinning (2D 3QMAS) experiment were performed by using a JEOL RESONANCE ECA 800 spectrometer at 18.79 T and a 3.2 mm home-made MAS probe with a MAS frequency of 20 kHz. The ^{27}Al Larmor frequency is 208.5 MHz. For ^{27}Al 1D MAS spectrum, a single-pulse excitation of 0.7 μs corresponding to a 1/3 of π/2

pulse width, and a recycle delay of 1 s were required. An external referenced sample of 1mol% $AlCl_3$ aqueous solution was used for 0 ppm. The ^{27}Al 2D 3QMAS spectrum was collected by using a z-filtering 3QMAS pulse sequence.[8] The duration of the triple-quantum excitation pulse was 0.25 s.

A white LED was fabricated by combining a UV LED chip (365 nm) with commercial green ($SrSi_2O_2N_2:Eu^{2+}$) and red emitting ($Sr_{0.9}Ca_{0.1}AlSiN_3:Eu^{2+}$) phosphors and the prepared 5% Ce doped $La_3Si_{6.5}Al_{1.5}N_{9.5}O_{5.5}$ blue phosphor. The optical properties of the LED were measured using an integrated sphere spectroradiometer system (LHS-1000, Everfine Co., Hangzhou, China).[9] The LED was operated at a bias current of 300 mA and a voltage of 3.756 V.

5.3 Results and discussion

5.3.1 Phase identification and photoluminescence properties of $La_3Si_{6.5}Al_{1.5}N_{9.5}O_{5.5}$:0.05Ce phosphor

A single phase $La_3Si_{6.5}Al_{1.5}N_{9.5}O_{5.5}$:0.05Ce sample has been obtained for the first time, by carefully controlling the synthesis condition. As shown in Figure 5.1a, all of the peaks of the X-ray diffraction (XRD) pattern match well with the candidate Al-containing La N-phase (ICSD 93506), no impurity can be detected. $La_3Si_{6.5}Al_{1.5}N_{9.5}O_{5.5}$:0.05Ce phosphor crystalizes in space group I2/a with a = 15.8383 (18) Å, b = 4.8989(6) Å, c = 18.029(2) Å, β = 114.807(5)°, V = 1269.8(3) $Å^3$. The lattice parameters are slightly smaller than those reported by Grins et al. [2], which is due to that Ce ions are slightly smaller than La ions.[10] In $La_3Si_{6.5}Al_{1.5}N_{9.5}O_{5.5}$ crystal structure, there are two La sites that can be occupied by Ce atoms. The La1 site is octahedrally coordinated by 4 X ($X = N_{0.56}O_{0.44}$) atoms and 2 O atoms at distances of 2.48-2.74 Å, and the La2 site is coordinated by 5 X atoms, 2 O atoms and 1 N atom at distances of 2.51-3.01 Å, which approximately form a cubic antiprism,[2] as shown in Figure 5.1b.

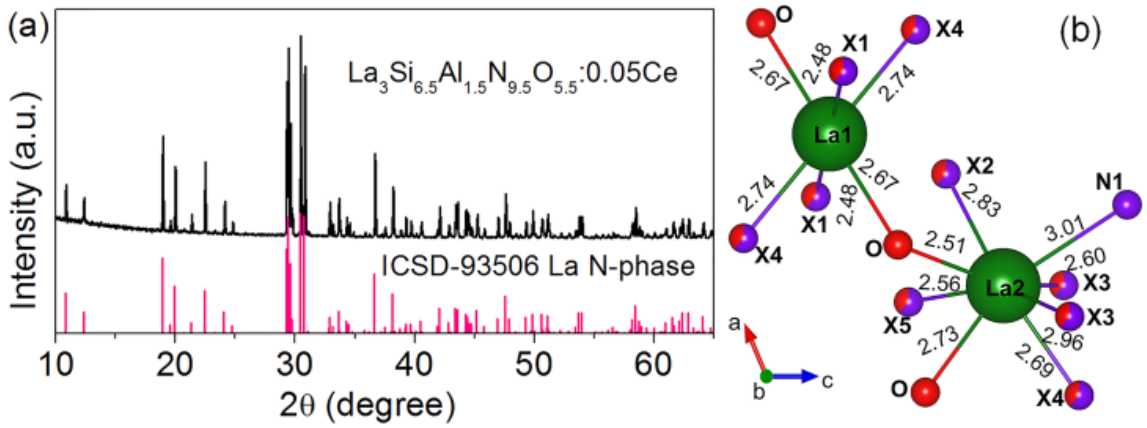

Figure 5.1 (a) The XRD pattern of 5% Ce doped $La_3Si_{6.5}Al_{1.5}N_{9.5}O_{5.5}$ phosphor; (b) the coordination of the two La sites in $La_3Si_{6.5}Al_{1.5}N_{9.5}O_{5.5}$ phase (X = O/N) on which Ce can substitute.

Figure 5.2a and 2b present the photoluminescence emission and excitation spectra of 5% Ce doped $La_3Si_{6.5}Al_{1.5}N_{9.5}O_{5.5}$ phosphor. Excitation at 355 nm results in a narrow Ce^{3+} 5d-4f emission band at 425 nm with a full width at half maximum of 71 nm. When monitoring the 425 nm emission, a broad band is observed, extending from the UV up to 425 nm with a maximum at 355 nm. This band is attributed to the Ce^{3+} 4f-5d absorption. From the Ce L_3 XANES spectra as shown in Figure 5.2c, one can see there is only Ce^{3+}, although the starting material containing Ce is CeO_2. This is due to carbon reduction at high temperature, which can provide the reductive atmosphere.[11] The emission maximum at 425 nm indicates that the phosphor has a deep blue emission. The short wavelength blue emission is an advantage for application in UV excitable white LEDs, as it will result in a high color rendering.[12-13] The CIE coordinates (x = 0.155 and y = 0.079) of $La_3Si_{6.5}Al_{1.5}N_{9.5}O_{5.5}$:0.05Ce phosphor are close to the National Television System Committee (NTSC) blue standard (x = 0.155; y = 0.070), better than AlN:Eu^{2+} phosphor (x = 0.139 and y = 0.106)[14], and similar to $LaSi_3N_5$:Ce (x = 0.156 and y = 0.067)[15] in the color purity, as shown in Figure 5.2d.

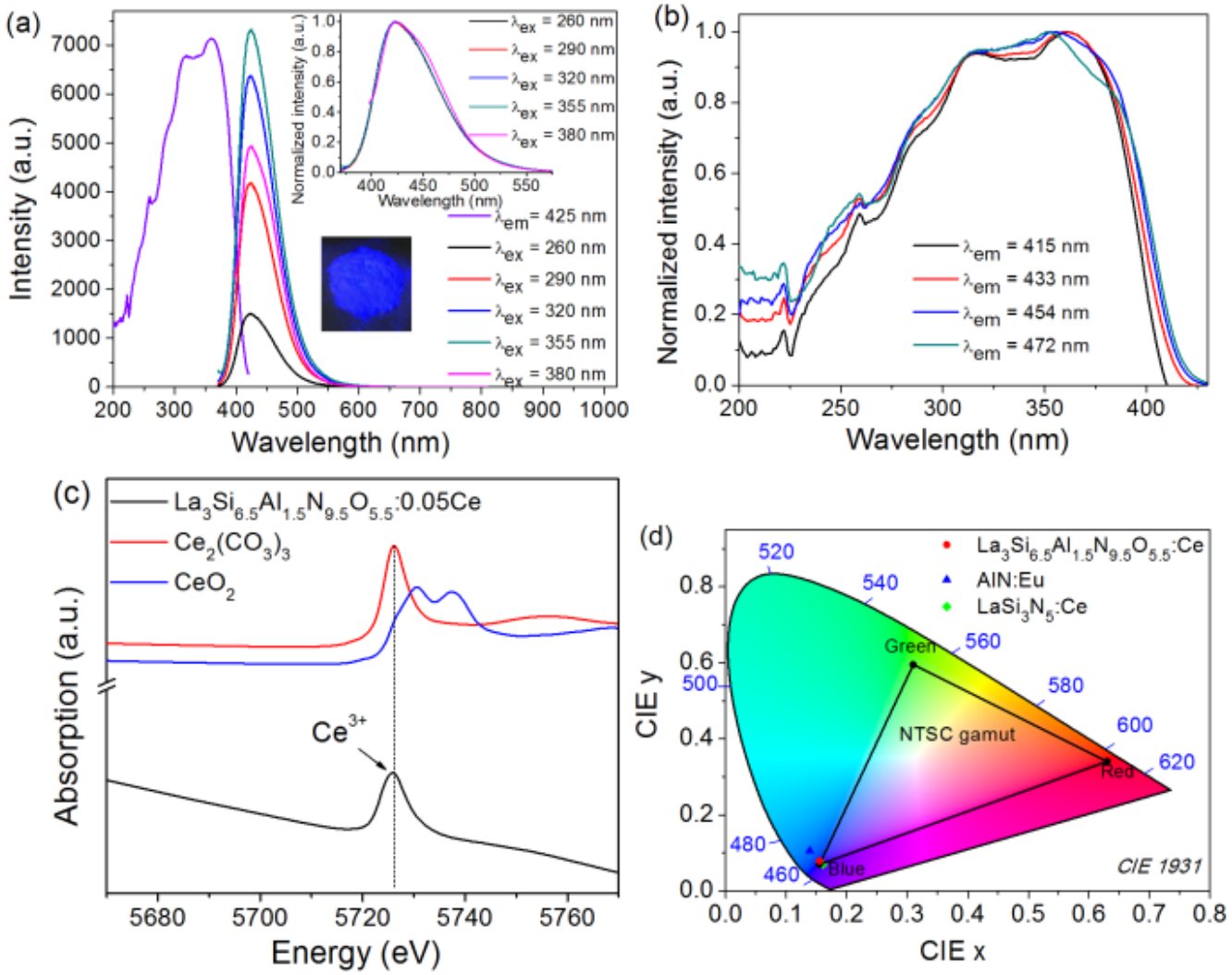

Figure 5.2 (a) Excitation spectrum monitoring 425 nm emission and excitation wavelength dependent emission spectra at room temperature for 5% Ce doped $La_3Si_{6.5}Al_{1.5}N_{9.5}O_{5.5}$ phosphor and its luminescence photo excited by a 365 nm UV lamp. The inset is the normalized emission spectra. (b) Emission wavelength dependent excitation spectra of $La_3Si_{6.5}Al_{1.5}O_{5.5}N_{9.5}$:0.05Ce phosphor at room temperature. (c) Ce L_3 XANES spectra of the $La_3Si_{6.5}Al_{1.5}O_{5.5}N_{9.5}$:0.05Ce phosphor and $Ce_2(CO_3)_3$, CeO_2 referenced samples for Ce^{3+} and Ce^{4+} respectively. (d) The CIE chromaticity coordinates of $La_3Si_{6.5}Al_{1.5}O_{5.5}N_{9.5}$:Ce, AlN:Eu and $LaSi_3N_5$:Ce phosphors.

As there are two La sites on which Ce can substitute, as shown in Figure 5.1b, two different local environments for Ce may be expected, resulting in differences between excitation and emission spectra

for the luminescence centers. However, when the sample is excited at different wavelengths, no changes in shape or position of emission spectra can be observed, except for 380 nm excitation, as shown in Figure 5.2a. The emission spectrum becomes slightly broader at the long wavelength side after 380 nm excitation. In order to check whether the broadening is caused by self-absorption or by emission from another site with lower energy, the emission wavelength dependent excitation spectra are measured, as shown in Figure 5.2b.

There are small changes in the shape of excitation spectra monitoring different emission wavelengths. There is a small broadening of the excitation spectra when monitoring the longer wavelength emission as compared to the shorter wavelength emission, but the main difference between the excitation spectra can be seen around 370 nm where the excitation spectrum monitoring the 472 nm emission has a different shape. This different shape cannot be just attributed to self-absorption, but is more likely to be the result of the excitation of different luminescent centers. However, since the differences in the excitation and emission spectra are all relatively small, this indicates that the two luminescent centers have similar energy, resulting in a strong overlap between the emission spectra from the two different luminescence sites, and keeping the emission bands relatively narrow (FWHM = 71 nm).

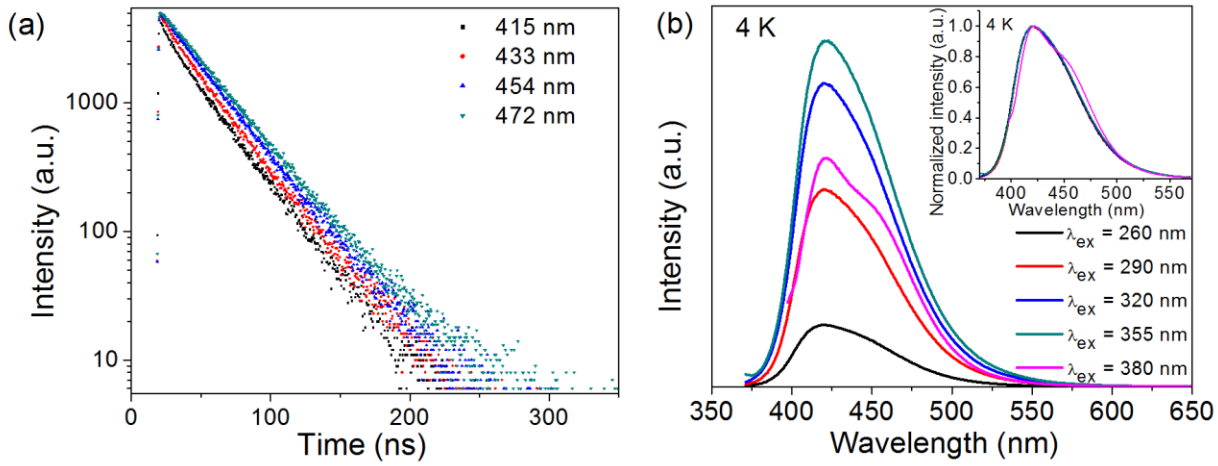

Figure 5.3 (a) Luminescence decay curves of 5% Ce doped $La_3Si_{6.5}Al_{1.5}N_{9.5}O_{5.5}$ phosphor after 370 nm excitation, monitoring the 415 nm, 433 nm, 454 nm and 472 nm emission. (b) Excitation wavelength dependent emission spectra and the normalized spectra (inset) at 4 K for 5% Ce doped $La_3Si_{6.5}Al_{1.5}N_{9.5}O_{5.5}$ phosphor.

As shown in Figure 5.3, the decay curves monitoring the different emissions from 415 nm, 433 nm, 454 nm and 472 nm are very similar. Since it is difficult to fit the data as a single exponential decay curve and because there are two luminescence sites, the decay curves are reasonably fitted with a bi-exponential equation according to [16]

$$I = A_1 \exp\left(-\frac{t}{\tau_1}\right) + A_2 \exp\left(-\frac{t}{\tau_2}\right)$$

and the decay time is calculated with the equation

$$\tau = (A_1\tau_1^2 + A_2\tau_2^2)/(A_1\tau_1 + A_2\tau_2)$$

The lifetimes of different emissions are different but still very close with $\tau_{(\lambda em = 415\ nm)}$ = 25.93 ns, $\tau_{(\lambda em = 433\ nm)}$ = 30.92 ns, $\tau_{(\lambda em = 454\ nm)}$ = 31.96 ns and $\tau_{(\lambda em = 472\ nm)}$ = 32.84 ns. The shape of the emission spectrum after 380 nm at 4 K shown in Figure 5.3b is obviously different from the one at room temperature shown in Figure 5.2a. A shoulder located around 450 nm appears at 4 K that can easily be attributed to the other luminescent site. At room temperature this shoulder is less clear, which is due to energy transfer between the two sites with different energy. The room temperature luminescence decay times as well as the emission spectra at 4 K confirm that there are indeed two luminescence centers in 5% Ce doped $La_3Si_{6.5}Al_{1.5}O_{5.5}N_{9.5}$ phosphors with similar energy.

5.3.2 $La_{3(1-y)}Si_{6.5}Al_{1.5}N_{9.5}O_{5.5}$:3yCe (y = 0.005-0.50) phosphors

$La_{3(1-y)}Si_{6.5}Al_{1.5}N_{9.5}O_{5.5}$:3yCe samples have been made with various Ce concentrations ranging from y = 0.005 to y = 0.50. The Ce concentration has been verified by EDS analysis, presented in the supplementary information (Figure 5.S1). No impurity phase can be detected in the XRD patterns for any of the concentrations. The large solubility of Ce in the La N-phase can be understood by the similarity of the radii of the La^{3+} and Ce^{3+} ions. Note that Ce N(ew)-phase also exists.[2] As shown in Figure 5.4a, the excitation and emission band gradually shift to longer wavelength with increasing Ce concentration. The emission peak wavelength can be shifted from 417 nm to 450 nm when the Ce concentration is increased from y = 0.005 to y = 0.50. No distinct change in shape of excitation and emission spectra or the luminescence decay curves (see Figure 5.S2 and 5.S3) can be observed, again indicating that the energy of Ce on the two different sites is very close. The redshift of the emission can be explained by reabsorption and energy transfer. As there is strong overlap between excitation and emission spectra, the high energy emitted light can be reabsorbed, resulting in a shift of emission band towards lower energy. Upon further increasing the Ce concentration, the redshift of emission can be

enhanced by energy transfer. For high concentrated samples, the average distance between the Ce^{3+} ions becomes much shorter. This increases the probability for non-radiative energy transfer among Ce^{3+} ions, resulting in the redshift. This has also been observed for other phosphors in which the Ce^{3+} ion is located on multiple sites, such as in Ce^{3+} doped $La_5Si_3O_{12}N$.[17] Additionally, shrinkage of the lattice also contributes to the redshift of the emission, as the lattice constants become smaller with increasing Ce concentration due to the smaller size of the Ce^{3+} ion as compared to the La^{3+} ion. The increased crystal field splitting caused by the shrinkage of the lattice shifts the lowest 5d level to lower energy.

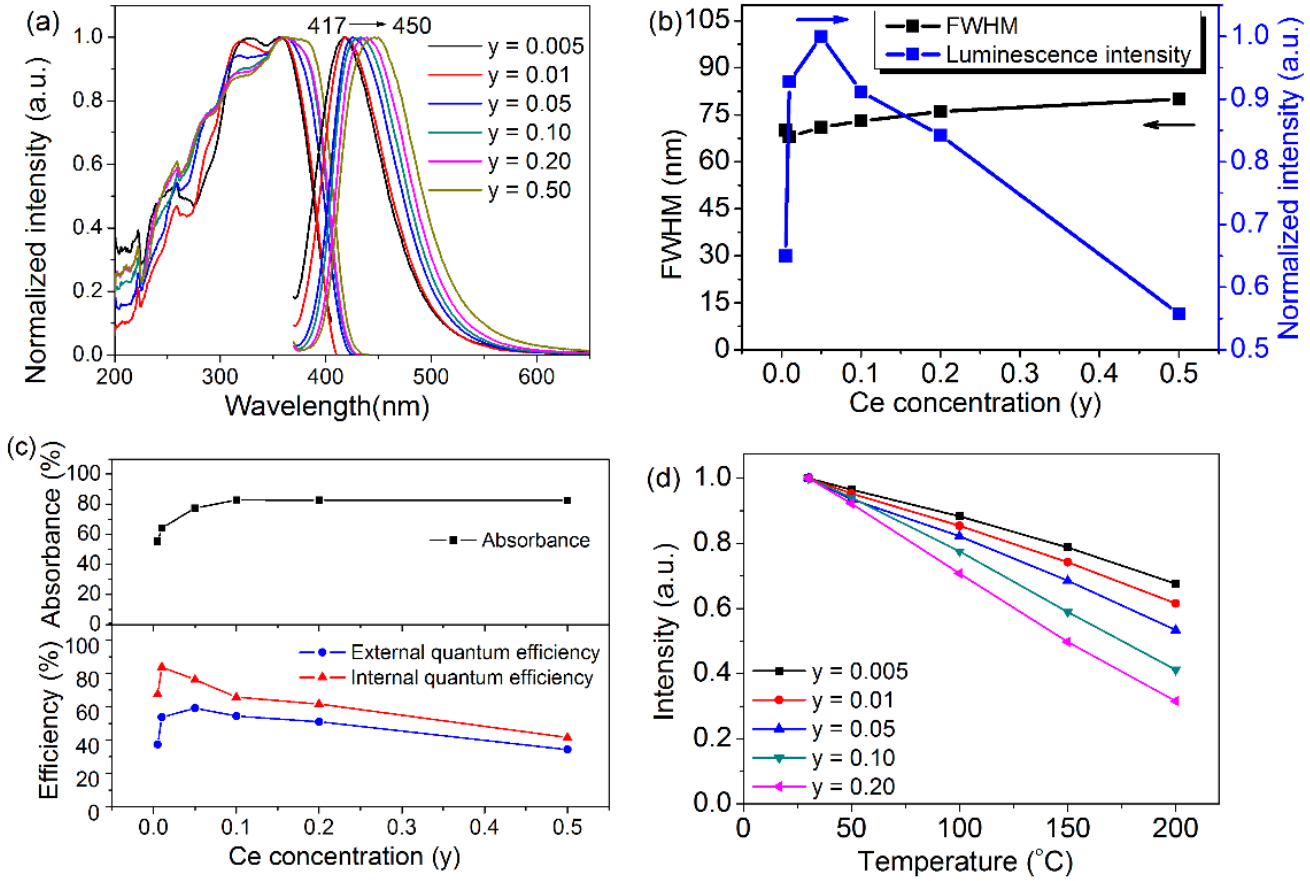

Figure 5.4 (a) The normalized photoluminescence spectra, (b) luminescence intensity and FWHM, (c) absorbance, internal quantum efficiency and external quantum efficiency, and (d) temperature dependence of emission intensity from 25 °C to 200 °C for $La_{3(1-y)}Si_{6.5}Al_{1.5}N_{9.5}O_{5.5}$:3yCe (y = 0.005-0.50) phosphors. All samples were excited with 355 nm light and the excitation spectra monitored the emission peak wavelength.

With raising the concentration of Ce, the luminescence intensity tends to increase and reaches a maximum when y is 0.05, as shown in Figure 5.4b, which corresponds to a highest external quantum efficiency (EQE) of 60% (see Figure 5.4c). Further increase of the Ce concentration (y value) results in a decrease in luminescence intensity, because of concentration quenching. The emission band becomes broader, increasing the full width at half maximum (FWHM) from 68 nm at y = 0.005 to 80 nm at y = 0.5. When y is 0.01, a high internal quantum efficiency (IQE) of 84% is obtained at room temperature. Figure 5.4d shows the temperature dependency of the luminescence for various Ce concentrations. The luminescence quenches much faster with higher Ce concentrations. This is due to thermally activated concentration quenching, as also happens in for example YAG:Ce^{3+}.[18] When the Ce concentration is below 10%, the luminescence quenches with less than 50% at 200 °C, as compared to the intensity at room temperature: the emission intensity drops to 68%, 62% and 54% for 0.5% Ce, 1% Ce and 5% Ce doped samples, respectively.

5.3.3 5% Ce doped $La_3Si_{8-x}Al_xN_{11-x}O_{4+x}$ (x = 0-2.0) phosphors

(1) Structural evolution

Figure 5.5a shows the XRD patterns of $La_3Si_{8-x}Al_xN_{11-x}O_{4+x}$ (x = 0-2.0) samples with a constant 5% doping of Ce at La site. When x is changed from 0 to 1.5, the XRD patterns match well with the candidate La N-phase (ICSD-93506); no impurity phase can be detected. A trace amount of $LaAlO_3$ (ICSD-92555) impurity forms for a sample with x value of 2.0, demonstrating that the approximate solubility limit is 1.5, which is consistent with the Al substituted La N-phase structure ($La_3Si_{8-x}Al_xN_{11-x}O_{4+x}$, x ≈ 1.5) derived by Grins et al.[2] When x value is increased from 0 to 1.5, the main XRD peaks shift markedly toward lower angles with increasing x, indicating a lattice expansion due to substitution of larger AlO^+ combination ($^{[4]}r(Al^{3+}) + {}^{[4]}r(O^{2-}) = 0.39 + 1.38 = 1.77$) for SiN^+ ($^{[4]}r(Si^{4+}) + {}^{[4]}r(N^{3-}) = 0.26 + 1.46 = 1.72$ Å).[10] Within the 2θ range of 29.0 to 31.0, the peaks depending on the lattice parameter b, such as the (-4 -1 1), (-4 -1 3), (2 1 3) and (2 1 -5) peaks show a large shift towards smaller 2θ with increasing x value. Similarly, the (0 2 0) peak shifts from 36.94 degrees for x = 0 to 36.65 degrees for x = 1.5. On the other hand, the peaks independent of the lattice parameter b show a slight shift towards larger 2θ, such as the (2 0 4), (0 0 2) and (2 0 0) peaks. Since the β angle increases from 114.406(6) degrees to 114.807(5) degrees when x value is increased from 0 to 1.5, the lattice parameters a and c also become larger. These variations caused by Al substitution indicate that b increases the most,

which is consistent with the calculated lattice parameters shown in Figure 5.5b. The unit cell volume of $La_3Si_{6.5}Al_{1.5}N_{9.5}O_{5.5}$:0.05Ce is 1.21% larger than that of $La_3Si_8N_{11}O_4$:0.05Ce.

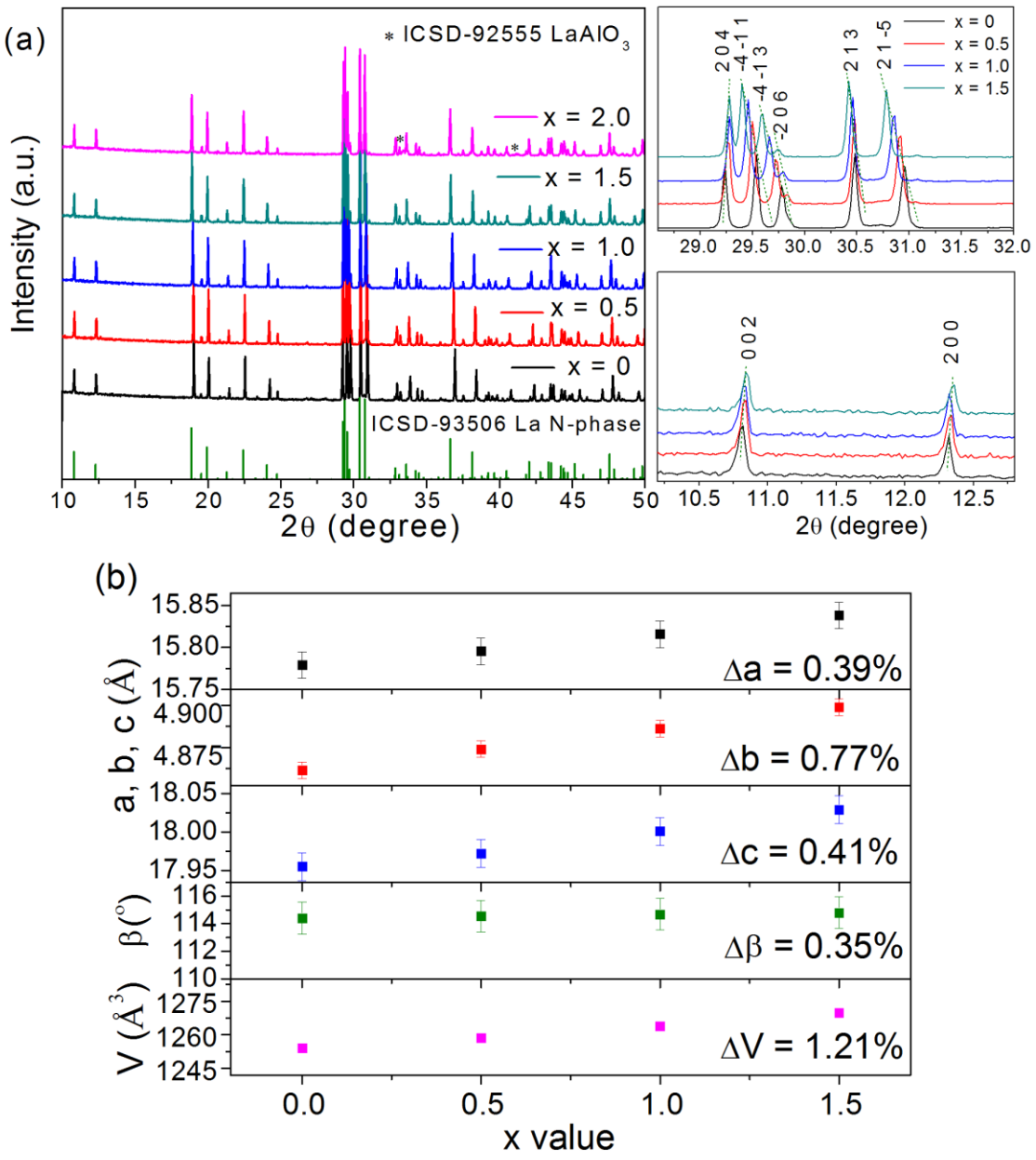

Figure 5.5 (a) XRD patterns of 5% Ce doped $La_3Si_{8-x}Al_xN_{11-x}O_{4+x}$ (x = 0-2.0) samples and (b) the lattice parameters with varying x value (x = 0-1.5).

In order to check the effect of the SiN → AlO substitution on the local structure of $La_3Si_{8-x}Al_xN_{11-x}O_{4+x}$, ^{29}Si and ^{27}Al NMR measurements have been performed for non-doped $La_3Si_{6.5}Al_{1.5}N_{9.5}O_{5.5}$ sample. Figure 5.6b shows the ^{29}Si MAS NMR spectrum with two distinct peaks in a 3.4:1 integral intensity ratio at δ_{Si} = -54.7 ppm and δ_{Si} = -67.0 ppm, respectively. Note that the small signal at -22 ppm is from silicone rubber used in the NMR probe, while another one at -160 ppm is a ghost signal called spinning sideband, since the spinning speed used is 10 kHz. For the compound without Al ($La_3Si_8O_4N_{11}$), the two peaks in an intensity ratio of 3:1 at δ_{Si} = -57.3 ppm and δ_{Si} = -68.2 ppm, have been assigned to ([SiN_4]+[SiN_3O]) and [SiN_2O_2] by Koroglu et al., respectively [7], combining with the La N-phase crystal structure model (shown in Figure 5.6a). Since the peak at δ_{Si} = -57.3 ppm is much broader than the peak at δ_{Si} = -68.2 ppm, this assignment is reasonable due to the chemical shifts of the [SiN_4] and [SiN_3O] tetrahedra are very similar, which has been observed for both the melilite and J-phases in the Y-Si-O-N system[19, 20]. The case in $La_3Si_{6.5}Al_{1.5}N_{9.5}O_{5.5}$ is similar to $La_3Si_8O_4N_{11}$, so the two peaks at δ_{Si} = -54.7 ppm and δ_{Si} = -67.0 ppm is assigned to ([SiN_4] + [SiN_3O]) and [SiN_2O_2], respectively. With the introduction of Al to the structure, the relative intensity of the [SiN_2O_2] peak thus decreases, indicating that the Si → Al substitution occurs at oxygen rich sites.

Figure 5.6c displays the ^{27}Al 1D MAS NMR spectrum of non-doped $La_3Si_{6.5}Al_{1.5}N_{9.5}O_{5.5}$ sample. The 1D MAS NMR spectrum exhibits a narrow peak at δ_{Al} = 97 ppm and a broad shoulder at δ_{Al} = 85 ppm. Note that these values are the positions of peak maxima and do not correspond to the isotropic chemical shifts due to the quadrupole nature (I = 5/2). The ^{27}Al 2D 3QMAS NMR spectrum shown in Figure 5.6d exhibits three distinct peaks of 102 ppm, 91 ppm and 80 ppm in the spectrum of projecting to isotropic dimension, which can be assigned to whether [AlN_2O_2], [$AlNO_3$] and [AlO_4] or [AlN_3O] [AlN_2O_2] and [$AlNO_3$], respectively.[21, 22] Considering a local structure analogous to $La_3Si_8O_4N_{11}$ with a Si-N → Al-O substitution, [AlN_3O], [AlN_2O_2] and [$AlNO_3$] is most plausible.

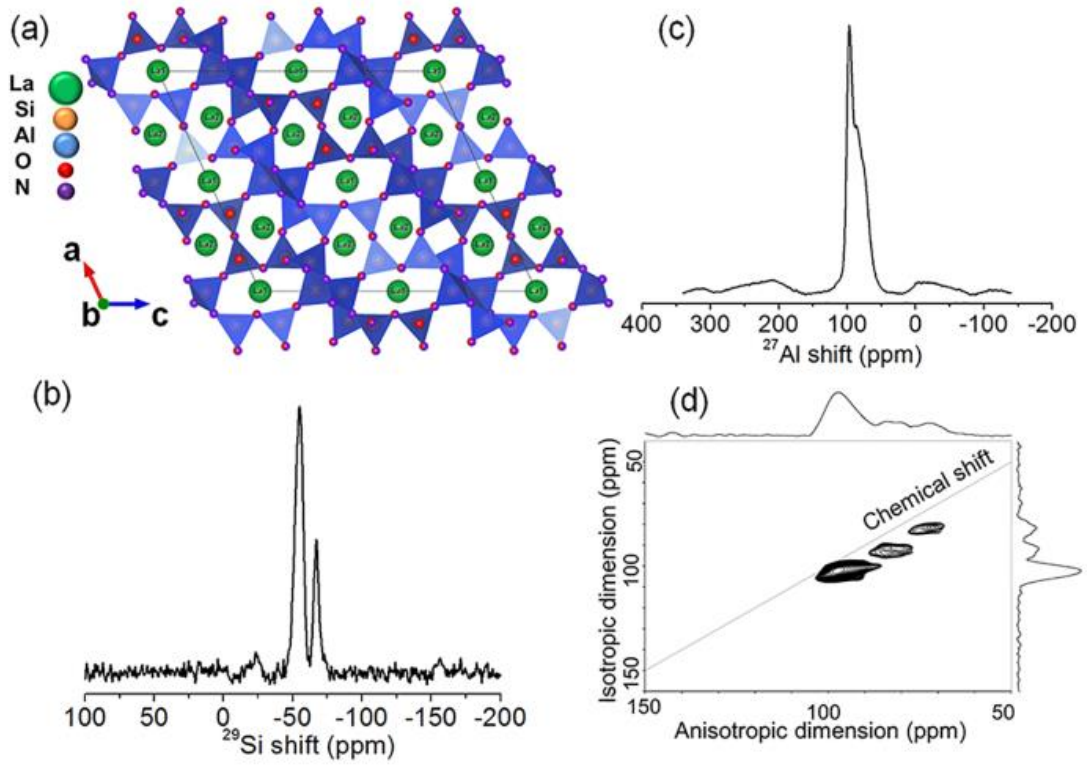

Figure 5.6 The crystal structure (a), ^{29}Si MAS NMR spectrum (b), ^{27}Al 1D MAS NMR spectrum (c) and ^{27}Al 2D 3QMAS NMR spectrum (d) of non-doped $La_3Si_{6.5}Al_{1.5}N_{9.5}O_{5.5}$ sample.

(2) Photoluminescence properties

As shown in Figure 5.7, the excitation spectra and emission spectra of the $La_3Si_{8-x}Al_xN_{11-x}O_{4+x}$:5%Ce samples with different x values at room temperature are very similar in shape and there is almost no shift in the maximum wavelength. The excitation spectra (Figure 5.7a), monitoring the emission peak wavelength, all have a maximum at 355 nm and a minimal blue-shift (5 nm) at the long wavelength side. Excitation at 355 nm results in a narrow Ce^{3+} 5d-4f emission band centered at 425 nm for all of the samples with different x values. The emission spectra (Figure 5.7b) overlap at the short wavelength side and become slightly broader with increasing x value, resulting in a slender red-shift. Notice that the photoluminescence spectra for the sample without Al (x = 0) are similar to what has been reported by Dierre et al.,[23] but the emission band in this work (FWHM = 71 nm) is slightly narrower than that reported by Dierre et al. (FWHM = 80 nm), which may be due to an improvement of phase purity. The emission intensity is enhanced by partially substituting Al-O for Si-N and reaches a maximum when x

value is 1.5. The sample with x value of 2.0 shows the lowest emission intensity, which is probably due to the $LaAlO_3$ impurity phase.

When Si-N is partially replaced by Al-O, two effects can occur simultaneously. 1) The replacement of Si by Al will result in a loss of rigidity of the structure.[24] Since the Stokes shift tends to be larger for less rigid compounds, this will shift the emission to longer wavelengths. 2) The replacement of N by O will increase the energy between the 4f ground state and the 5d excited states, because the nephelauxetic effect (centroid shift) and crystal field splitting are generally weaker for oxides than for nitrides. This will thus shift the excitation and emission bands to shorter wavelengths. The total effect of the replacement of Si-N by Al-O will be a combination of these two effects, depending on which of the effects is dominant. This is nicely illustrated by Chen et al.[3] for the SiN → AlO replacement in the $M_2Si_5N_8$ (M = Ca, Sr, Ba) series. In $Ca_2Si_5N_8$, the blue shift of the excitation and emission bands caused by the N to O replacement dominates because the smaller O^{2-} ions (as compared to N^{3-}) prefer to substitute close to the Eu^{2+} instead of close to Ca^{2+}, as this will reduce the lattice strain caused by the substitution of the large Eu^{2+} on the small Ca^{2+} site. In $Ba_2Si_5N_8$ on the other hand, the redshift of the emission caused by the loss of rigidity dominates because the O^{2-} ions prefer not to be positioned close to Eu^{2+} ions. Eu^{2+} is smaller than Ba^{2+} and thus prefers larger N^{3-} ions around it to minimize lattice strain. In $Sr_2Si_5N_8$, where Eu^{2+} is similar in size as Sr^{2+}, a combination of the two effects takes place: a small blue shift of the excitation band and a small redshift of the emission band. The latter is the same as we observe for SiN → AlO substitution in Ce^{3+} doped La N-phase: the difference in ionic size between Ce^{3+} and La^{3+} is relatively small, so there is not a large preferential occupation for the O^{2-} ions to reduce lattice strain. As a result a small blue shift of the excitation band is observed due to the introduction of O, in combination with a very small redshift of the emission band due to the loss of rigidity.

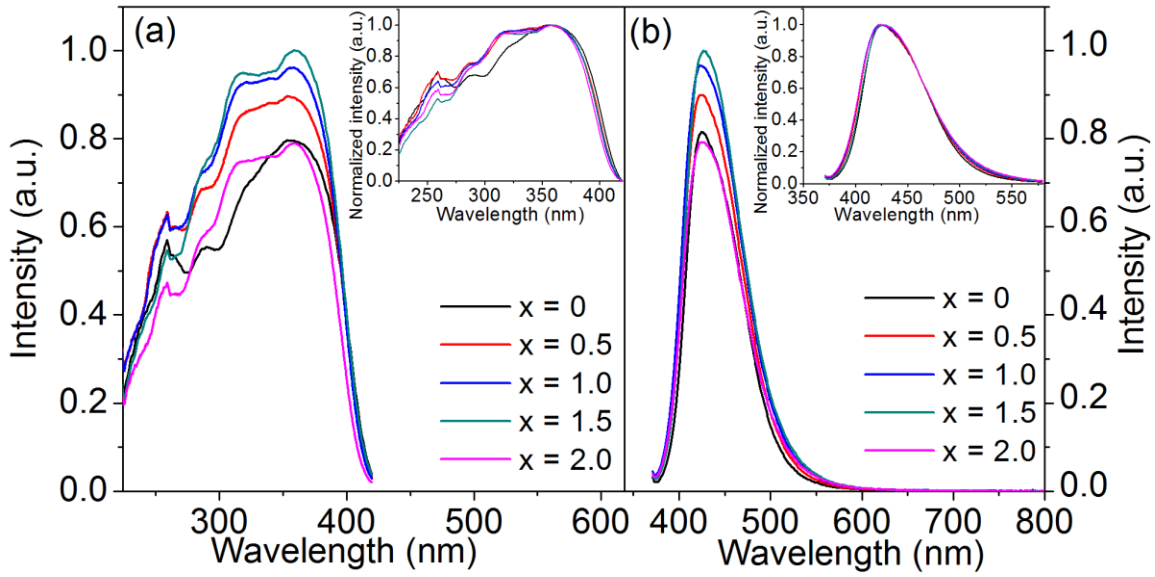

Figure 5.7 Excitation spectra monitoring 425 nm emission (a) and emission spectra after 355 nm excitation (b) at room temperature for 5% Ce doped $La_3Si_{8-x}Al_xN_{11-x}O_{4+x}$ (x = 0 - 2.0) phosphors. The normalized excitation spectra (a) and emission spectra (b) are shown as insets.

In Figure 5.8a, the time resolved emission spectra of the La N-phase with and without Al are shown at different delay times ranging from 53 ns to 796 ns. For both the sample with and without Al, a small red-shift of the emission spectrum is observed with increasing delay times, as can also be seen from the Figure 5.8b. When comparing the normalized emission spectra of the samples with and without Al for the shortest time (53 ns), one can see that the emission maxima are at the same position and that the spectra overlap at the short wavelength side. At the long wavelength side however, the emission spectrum of the Al containing sample is slightly broader, making the spectrum slightly red-shifted. A similar difference is observed when comparing the samples with and without Al at a longer time (796 ns). From this it is concluded that the small broadening of the emission spectrum at the long wavelength side by doping with Al, as seen in Figure 5.7, is most likely to be caused by an increase of Stokes shift after Al-O substitution.

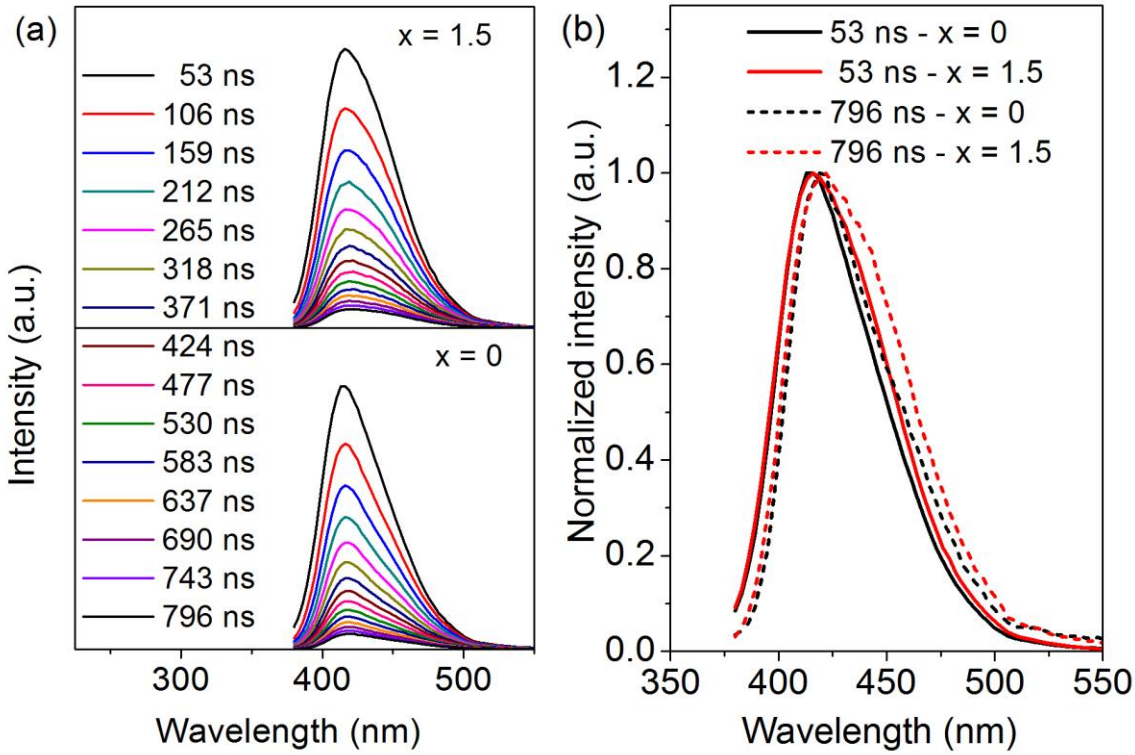

Figure 5.8 (a) Time-resolved emission spectra of 5% Ce doped $La_3Si_{8-x}Al_xN_{11-x}O_{4+x}$ (x = 0, 1.5) phosphors with an interval of 53 ns delay times and (b) the normalized time-resolved emission spectra with delay times of 53 ns and 796 ns.

(3) Thermal stability and quantum efficiency

Figure 5.9 shows the emission spectra of 5% Ce doped La N phase without Al (x = 0, $La_3Si_8O_4N_{11}$) and with Al (x = 1.5, $La_3Si_{6.5}Al_{1.5}N_{9.5}O_{5.5}$) at various temperatures. For the 5% Ce doped $La_3Si_{6.5}Al_{1.5}N_{9.5}O_{5.5}$ phosphor, as shown in Figure 5.9a, the emission intensity shows almost no decrease up to 250 K, and only 10% of the luminescence is quenched at room temperature compared to the intensity at 4 K. At 573 K, still 25.7% of the luminescence is left. No shift of the emission band or any changes in the shape of emission band can be detected for the Al-containing sample, over a temperature range from 4 K to 573 K. Concerning the 5% Ce doped $La_3Si_8O_4N_{11}$ phosphor without Al, the emission intensity starts to decrease directly above 4 K, falling off 20% at room temperature. At 573 K, about 22.6% of the luminescence is left compared to the intensity at 4 K, which can be seen in the inset of Figure 5.9b. When temperature is increased from 4 K to 573 K, a slight change in the shape of the

emission spectrum and a minimal red-shift of the position of the emission band (8 nm) can be observed. This is related to some temperature dependent energy transfer between the two luminescent centers. Since the luminescence intensity of a sample with x value of 1.5 is less thermally quenched than a sample with x value of 0 at room temperature, this explains why the Al containing sample (x = 1.5, IQE = 76%, EQE = 60%) has a higher luminescence efficiency than the sample without Al (x = 0, IQE =65%, EQE = 50%).

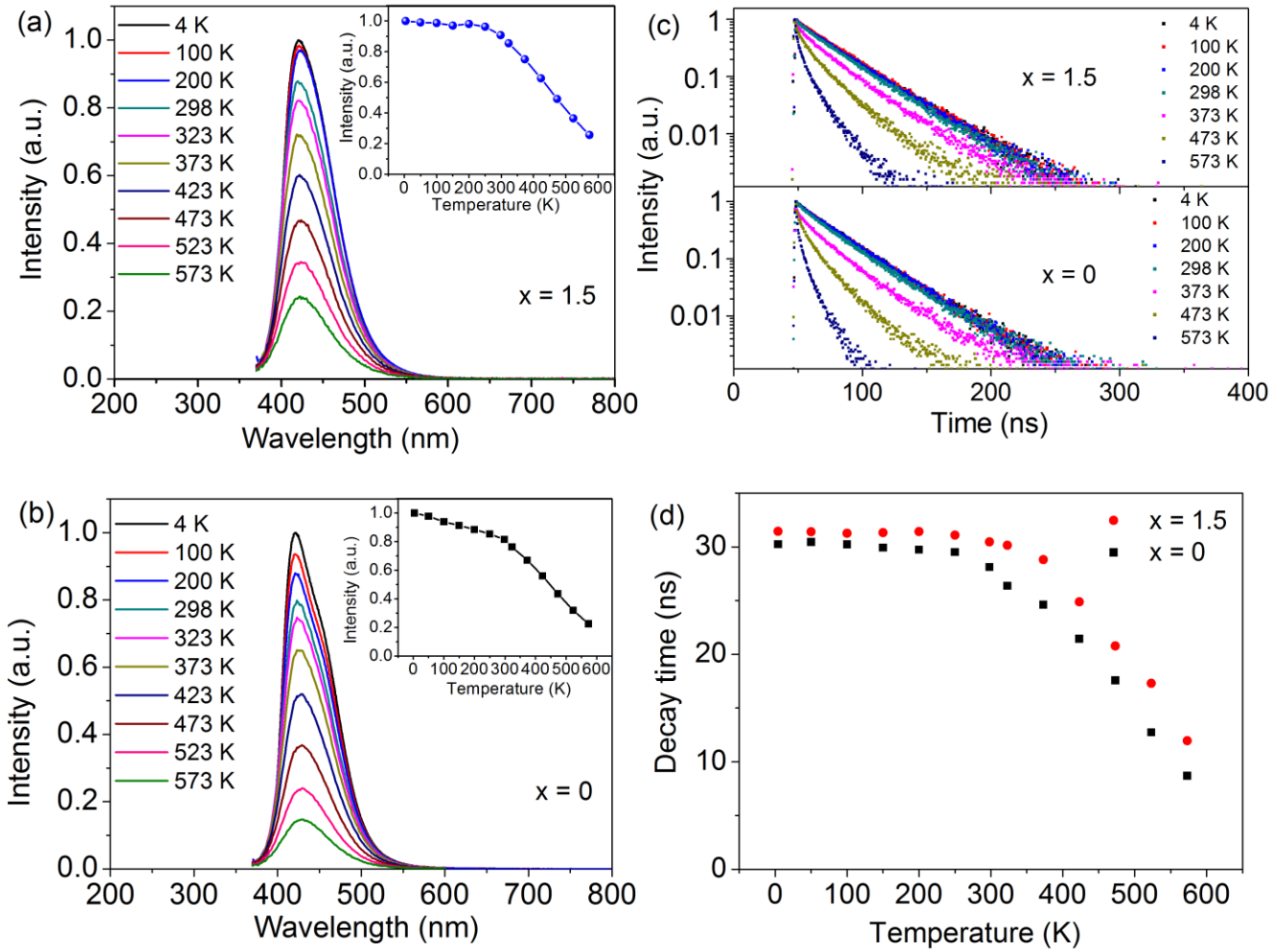

Figure 5.9 Temperature dependence of emission spectra after 355 nm excitation and integrated emission intensity (shown as insets) for 5% Ce doped $La_3Si_{8-x}Al_xN_{11-x}O_{4+x}$ phosphors with x = 1.5 (a) and x = 0 (b), respectively. The comparison of temperature dependence of luminescence decay (c) and decay time (d) monitoring the 425 nm emission.

In order to clarify the reason for the difference in thermal quenching behavior between the samples with and without Al, the temperature dependence of the luminescence decay has been monitored. As shown in Figure 5.9c, for both the samples with and without Al, the decay curves measured at various temperatures overlap when the temperature is below 250 K, indicating that the decay time keeps constant, as illustrated in Figure 5.9d. For an allowed transition like the Ce^{3+} 5d-4f emission, the radiative lifetime usually does not change strongly with temperature. Only when thermal quenching sets in, the luminescence lifetime shortens due to the non-radiative contribution to the decay process.[25, 26] This implies that the luminescence quenching between 4 K and 250 K observed for the sample without Al is not an intrinsic quenching, since the decay time remains constant.[18] The decrease in emission intensity between 4 K and 250 K for the sample without Al should therefore be ascribed to a lower absorption strength, resulting in a lower light output. In the Al containing sample, there is no decrease in emission intensity between 4 K and 250 K, implying that the absorption strength remains constant. The reason for the difference between the two samples could be related to some defects. It may be that non-luminescent defects in the sample without Al give rise to a competing absorption, causing a relatively lower absorption strength by Ce and therefore a decrease in luminescence intensity. Something similar also happens in YAG:Ce, where a non-intrinsic decrease in luminescence intensity is observed while the decay time remains constant.[18] The SiN → AlO substitution may reduce these defects, resulting in less thermal quenching between 4 K and 250 K for the Al containing sample.

Note that for the sample without Al a weak afterglow emission can be observed for several seconds after the excitation source has been removed. The delayed luminescence of the 5% Ce doped $La_3Si_8O_4N_{11}$ phosphor, with a lifetime in the ms range, is also shown in Figure 5.10. This afterglow behavior is not observed for the 5% Ce doped $La_3Si_{6.5}Al_{1.5}N_{9.5}O_{5.5}$ phosphor. The cause of the afterglow in the sample without Al can very well be related to the defects mentioned earlier, which are absent in the Al containing sample. The defects may act as an electron trap, causing the delay in luminescence. The afterglow behavior therefore gives a strong indication for the presence of defects in the sample without Al and that the Al-O substitution can remove these defects.

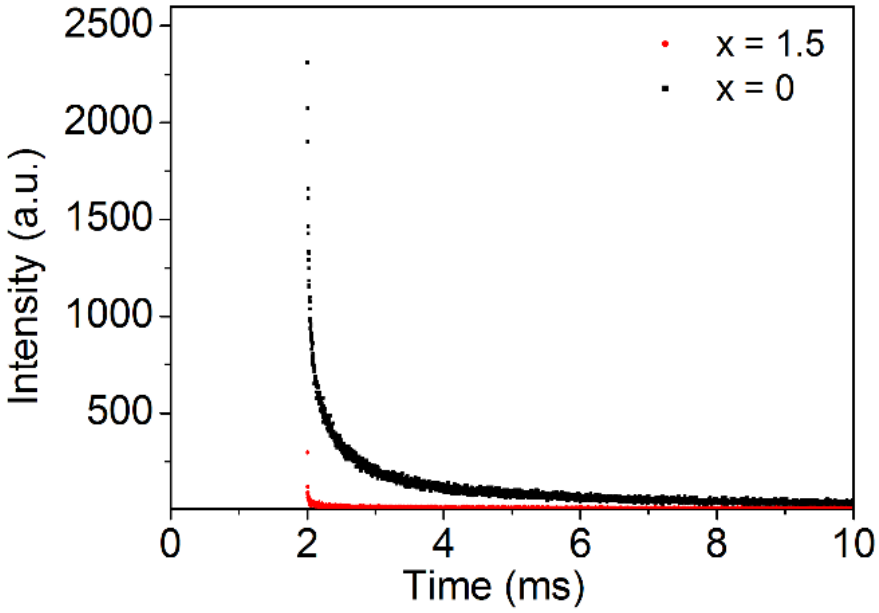

Figure 5.10 Decay curves of the delayed luminescence (ms scale) of 5% Ce doped $La_3Si_{8-x}Al_xN_{11-x}O_{4+x}$ samples (x = 1.5, 0) excited at 370 nm monitoring the 425 nm emission (The excitation light was shut off after 2 ms and the initial intensity is 10^6 a.u.).

Above 250 K, the decay times of both the samples with and without Al become smaller with increasing temperature, indicating that in both samples intrinsic thermal quenching starts to occur around 250 K. Note that between 350 and 573 K the decrease of decay time with temperature is very similar for both samples. This implies that, if the intrinsic thermal quenching is caused by thermal ionization of the electron from the 5d to the conduction band, the energy difference between the 5d state and the conduction band should be very similar.[27] In order to check this, the reflectance spectra of non-doped Al-containing sample (x = 1.5) and the sample without Al (x = 0) have been measured (shown as an inset in Figure 5.11). The Kubelka–Munk absorption spectra shown in Figure 5.11 are calculated from the reflectance by using: [28]

$$f(R) = \frac{(1-R)^2}{2R} = \frac{K}{S}$$

Where R is the absolute reflectance of the sampled layer, K is the molar absorption coefficient and S is the scattering coefficient. From the absorption edge in the UV region, the same value of 4.34 eV for the optical band gap is derived for $La_3Si_8O_4N_{11}$ and $La_3Si_{6.5}Al_{1.5}N_{9.5}O_{5.5}$. This implies that, taking into account the similarities in 5d-4f emission for the samples, the energy between the 5d state and the

conduction band are similar, explaining the similarities in thermal quenching behavior at higher temperatures.

Note that, while $La_3Si_8O_4N_{11}$ and $La_3Si_{6.5}Al_{1.5}N_{9.5}O_{5.5}$ have the same bandgap, there is still some difference in reflectance of both samples at longer wavelengths in the 300-450 nm region. For example, at 400 nm, the reflectance of the Al containing sample is 88%, while the sample without Al has a reflectance of 83%. The stronger absorption in the sample without Al can be attributed to the defects discussed earlier, that lower the efficiency of this sample.

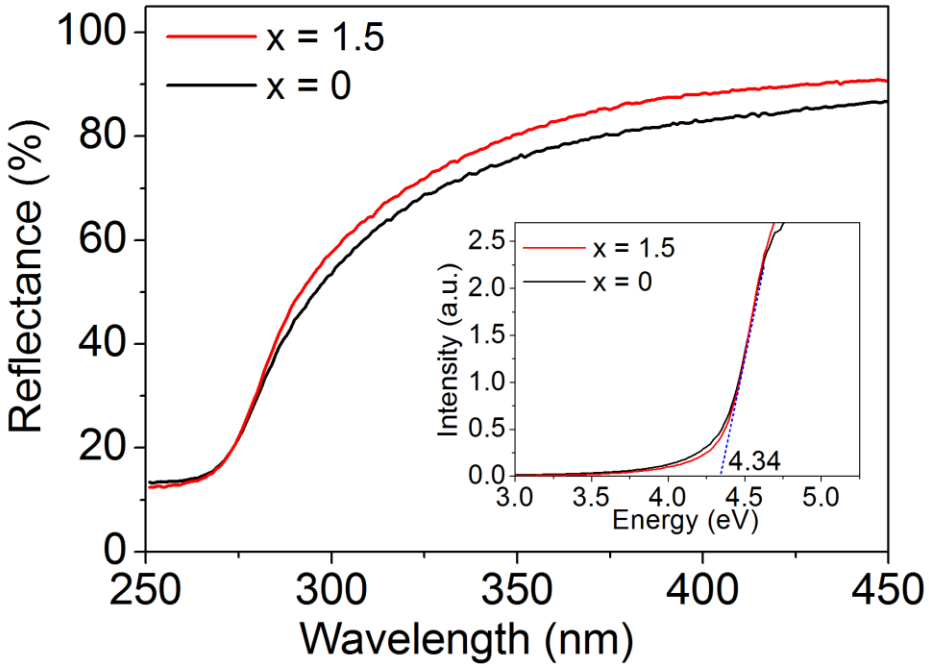

Figure 5.11 Diffuse reflectance spectra and the Kubelka–Munk absorption spectra (shown as an inset) of non-doped $La_3Si_{8-x}Al_xN_{11-x}O_{4+x}$ samples (x = 1.5, 0).

5.3.4 Application in a white LED

In order to test the potential of the deep blue emitting 5% Ce doped $La_3Si_{6.5}Al_{1.5}N_{9.5}O_{5.5}$ phosphor for solid-state white lighting, a white LED has been fabricated. The white LED, which is shown on the photos in Figure 5.12, contains the 5% Ce doped $La_3Si_{6.5}Al_{1.5}N_{9.5}O_{5.5}$ phosphor as the blue phosphor in combination with $SrSi_2O_2N_2:Eu^{2+}$ and $Sr_{0.9}Ca_{0.1}AlSiN_3:Eu^{2+}$ as green and red phosphors respectively, and a 365 nm UV-LED chip for excitation. The electroluminescence spectrum of the white LED is shown in Figure 5.12 as well.

The white LED has a correlated color temperature (CCT) of 4351 K giving a natural bright white color. The LED has chromaticity coordinates of x = 0.3669 and y = 0.3707, being close to the standard white point at x = 1/3 and y = 1/3. In Table 5.1 the color rendering indexes of the white LED are presented, showing that it has a high color rendering index (CRI) with all indexes above 88. The Ra value is 93.2 and the R9 value is 91.4. This makes the phosphor promising for white LED applications. The white LED has a luminous efficacy of 6.46 lm/W, which is a bit low due to the low efficiency of the LED chip that was used (0.78 lm/W).

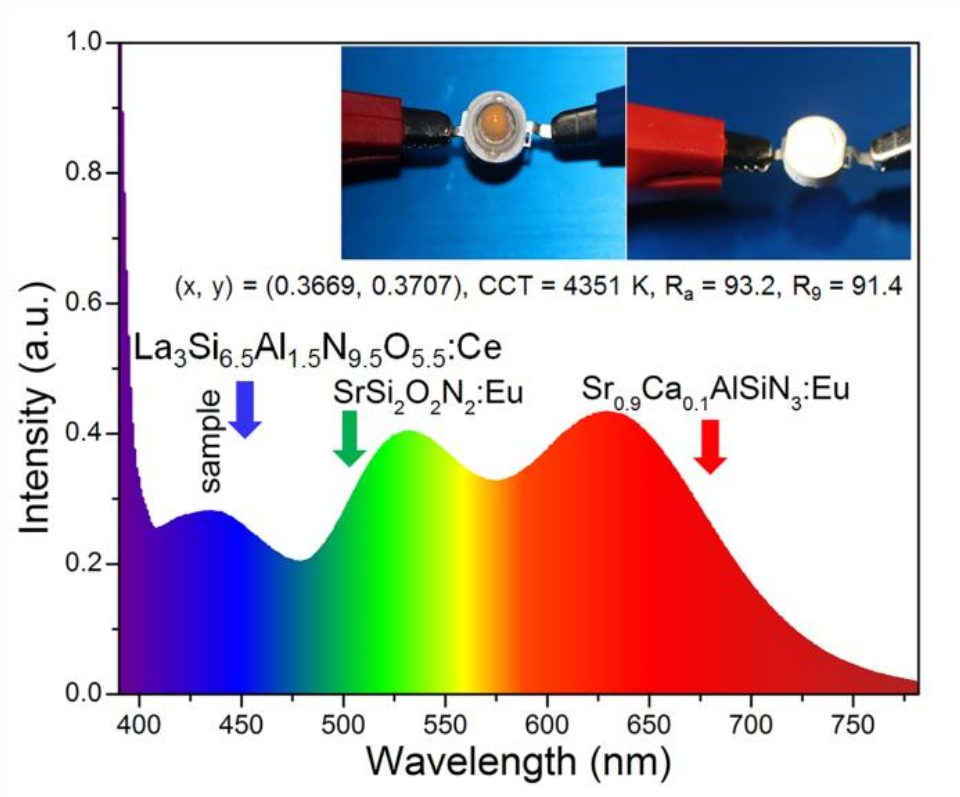

Figure 5.12 Electroluminescence spectrum of a white LED using a UV-LED chip (365 nm) and $La_3Si_{6.5}Al_{1.5}N_{9.5}O_{5.5}$:5%Ce, $SrSi_2O_2N_2:Eu^{2+}$ and $Sr_{0.9}Ca_{0.1}AlSiN_3:Eu^{2+}$ phosphors. The inset shows photographs of the LED while off and on.

Table 5.1 Color rendering indexes of the white LED containing 5% Ce doped $La_3Si_{6.5}Al_{1.5}N_{9.5}O_{5.5}$ blue phosphor

Ra	R1	R2	R3	R4	R5	R6	R7	R8	R9	R10	R11	R12	R13	R14	R15
93.2	96.2	96.5	88.3	88.8	95.8	96.1	91.9	91.9	91.4	90.2	88.2	89.5	98.6	92.5	95.9

5.4 Supporting Information

5.4.1 Energy-dispersive X-ray spectroscopy (EDS) analysis

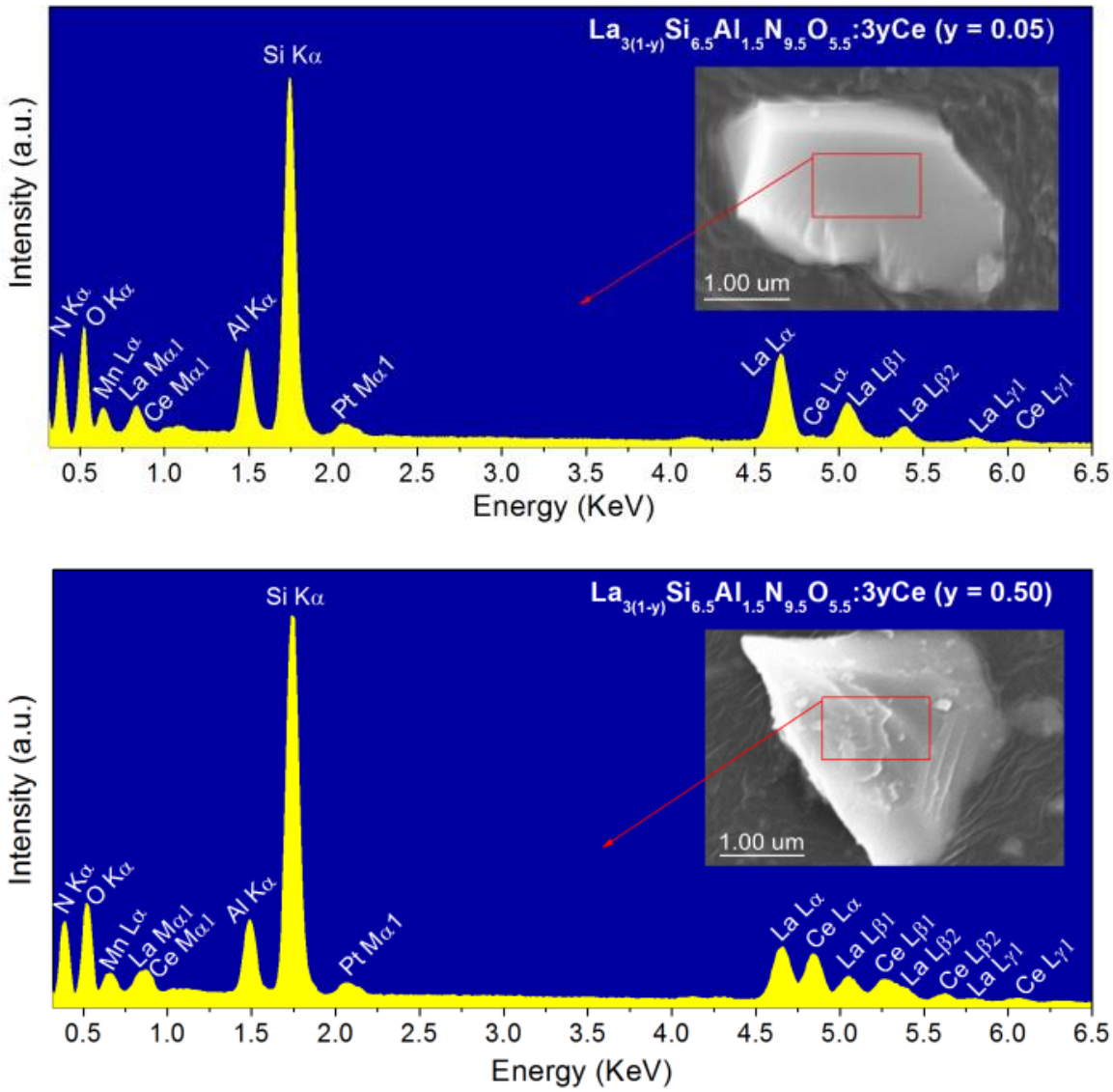

Figure 5.S1 EDS results of the $La_{3(1-y)}Si_{6.5}Al_{1.5}N_{9.5}O_{5.5}$:3yCe samples with y = 0.05 (left) and y = 0.50 (right).

The molar ratios of each element in the y = 0.05 sample are (ignoring the impurity elements Mn and Pt that are caused by EDS measurement):

n(La): n(Ce): n(Si): n(Al): n(N): n(O) = 6.94%: 0.52%: 17.46%: 3.94%: 43.93%: 27.21%

n(Ce): n(La) = 0.07; n(Al): n(Si) = 0.23 n(O): n(N) = 0.62

which are close to the ratios in starting materials:

n(Ce): n(La) = 0.05; n(Al): n(Si) = 0.23 n(O): n(N) = 0.58

The molar ratios of each element in the y = 0.50 sample are (ignoring the impurity elements Mn and Pt that are caused by EDS measurement):

n(La): n(Ce): n(Si): n(Al): n(N): n(O) = 5.33%: 5.09%: 22.89%: 4.24%: 39.79%: 22.66%

n(Ce): n(La) = 0.95; n(Al): n(Si) = 0.19 n(O): n(N) = 0.57

which are close to the ratios in starting materials:

n(Ce): n(La) = 1.00; n(Al): n(Si) = 0.23 n(O): n(N) = 0.58

5.4.2 Luminescence decay

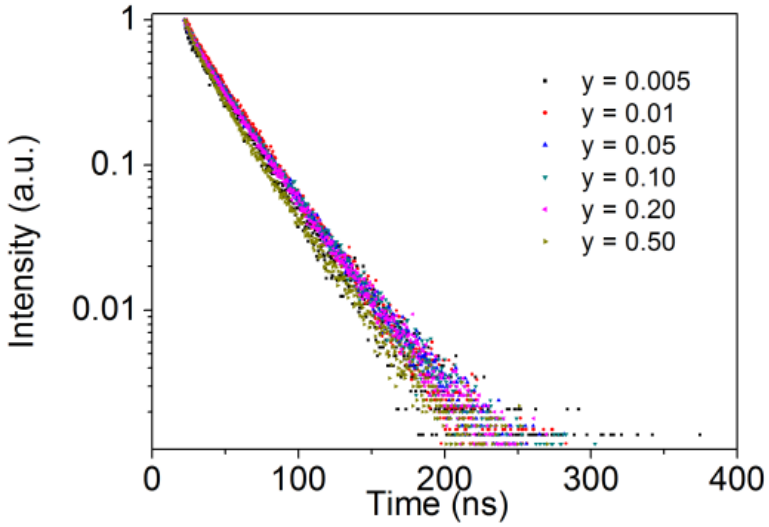

Figure 5.S2 Luminescence decay curves of $La_{3(1-y)}Si_{6.5}Al_{1.5}N_{9.5}O_{5.5}$:3yCe (y = 0.005-0.50) phosphors.

5.4.3 Excitation and emission wavelength dependent spectra

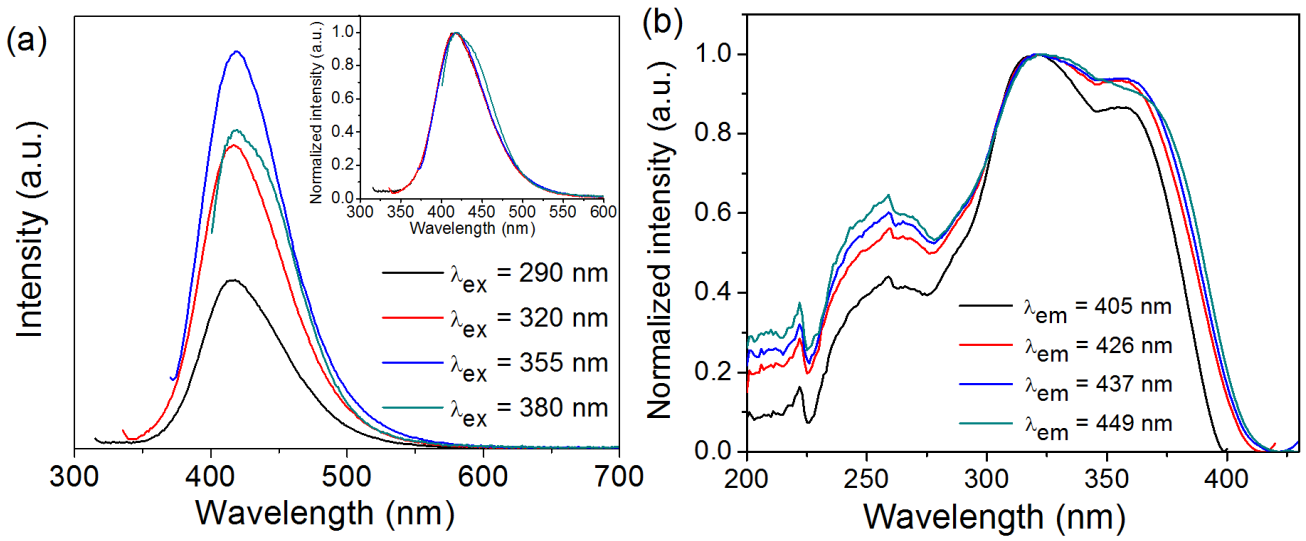

Figure 5.S3 Excitation wavelength dependent (a) and emission wavelength dependent (b) photoluminescence spectra of $La_{3(1-y)}Si_{6.5}Al_{1.5}N_{9.5}O_{5.5}$:3yCe (y = 0.005) phosphor at room temperature.

5.5 Conclusions

The $La_3Si_{6.5}Al_{1.5}N_{9.5}O_{5.5}$ single phase non-doped material and Ce doped phosphors have been synthesized for the first time with a solid-state reaction method at 1800 ^oC for 2 hours, by using La_2O_3, Si_3N_4, SiO_2, AlN and CeO_2 as starting materials. For non-doped sample, the high resolution solid-state NMR spectra of ^{29}Si and ^{27}Al show that $La_3Si_{6.5}Al_{1.5}N_{9.5}O_{5.5}$ has $[SiN_4]$, $[SiN_3O]$, $[SiN_2O_2]$ silicon environments, and $[AlN_3O]$, $[AlN_2O_2]$, $[AlNO_3]$ Al environments, which are in good agreement with the crystal structure model of $La_3Si_{6.5}Al_{1.5}N_{9.5}O_{5.5}$. Due to overlap of $[SiN_4]$ and $[SiN_3O]$, two peaks in a 3.4:1 intensity ratio at δ_{Si} = -54.7 ppm and δ_{Si} = -67.0 ppm are observed.

$La_3Si_{6.5}Al_{1.5}N_{9.5}O_{5.5}$:1%Ce phosphor displays a broad Ce^{3+} 4f-5d absorption band (UV to 410 nm) and a narrow emission band centered at short wavelength (418 nm, FWHM = 68 nm) with high efficiency (QE = 84%). The emission band of $La_3Si_{6.5}Al_{1.5}N_{9.5}O_{5.5}$:Ce phosphor can be shifted from 418 nm to 450 nm, by changing the Ce concentration from 0.5% to 50%, which is caused by reabsorption and energy transfer. The energy of Ce from two crystallographic sites is very close, resulting in a stable emission color and a similar decay behavior independent of excitation wavelength. Compared to Ce doped $La_3Si_8O_4N_{11}$ phosphor, the quantum efficiency and thermal stability of emission for

$La_3Si_{6.5}Al_{1.5}N_{9.5}O_{5.5}$:Ce phosphor have been improved without shifting the emission peak wavelength or changing the band gap. The enhancement of quantum efficiency is ascribed to less thermal quenching. Since $La_3Si_8O_4N_{11}$:Ce phosphor contains some non-luminescent defects, the electron trapping by these defects, gives rise to lower thermal stability of emission and some weak afterglow emission. It is noted however, that the thermal quenching of 5% Ce doped $La_3Si_{6.5}Al_{1.5}N_{9.5}O_{5.5}$ phosphor at high temperatures is still a bit high for the application in high power white LEDs, but the thermal stability could possibly be further improved by adjusting the chemical composition (Ce concentration), optimizing the synthesis approach or coating a thermally stable material layer on the phosphor surface to prevent the oxidation of dopant ions at high temperatures or to remove surface defects.

It is interesting to note that the 84% luminescence efficiency is relatively high as compared to other oxy-nitridosilicate phosphors with emission maximum in the same region (410 - 440 nm). The highest IQE reported for $LaSi_3N_5$:Ce with an emission maximum around 430 nm is 63.2% [15], while the $LaSiO_2N$:Ce phosphor has an even lower efficiency and fast thermal quenching [23]. Some other blue phosphors with a relatively high efficiency have been reported, such as $BaSi_3Al_3O_4N_5$:Eu,[29] but these phosphors have their maximum efficiency at longer wavelengths (450 - 470 nm). There is thus a lack of highly efficient deep blue phosphors with a maximum emission at short wavelengths (410 - 440 nm) that can be excited with near UV light (355 - 380 nm). These phosphors are highly demanded for near UV excitable white LEDs.[12-13, 30] The highly efficient Ce doped $La_3Si_{6.5}Al_{1.5}N_{9.5}O_{5.5}$ phosphor with short wavelength blue emission and high color purity is therefore very promising.

5.6 References

(1) Harris, R. K.; Leach, M. J.; Thompson, D. P. Nitrogen-15 and Oxygen-17 NMR Spectroscopy of Silicates and Nitrogen Ceramics *Chemistry of Materials* **1992**, *4*, 260-267.

(2) Grins, J.; Shen, Z.; Esmaeilzadeh, S.; Berastegui, P. The Structures of The Ce and La N-phases $RE_3Si_{8-x}Al_xN_{11-x}O_{4+x}$ (x ≈ 1.75 for RE = Ce, x ≈ 1.5 for RE = La), Determined by Single-Crystal X-ray and Time-of-Flight Neutron Powder Diffraction, Respectively *Journal of Materials Chemistry* **2001**, *11*, 2358-2362.

(3) Chen, W.-T.; Sheu, H.-S.; Liu, R.-S.; Attfield, J. P. Cation-Size-Mismatch Tuning of Photoluminescence in Oxynitride Phosphors *Journal of the American Chemical Society* **2012**, *134*, 8022-8025.

(4) Liu, Q.; Wang, T. In *Phosphors, up Conversion Nano Particles, Quantum Dots and Their Applications*; Springer: 2017, p 343-370.

(5) Li, H.-L.; Zhou, G.-H.; Xie, R.-J.; Hirosaki, N.; Wang, X.-J.; Sun, Z. Optical Properties of Green-Blue-Emitting Ca-α-Sialon:Ce^{3+}, Li^+ Phosphors for White Light-Emitting Diodes (LEDs) *Journal of Solid State Chemistry* **2011**, *184*, 1036-1042.

(6) Harris, R. K.; Leach, M. J.; Thompson, D. P. Silicon-29 Magic-Angle Spinning Nuclear Magnetic Resonance Study of Some Lanthanum and Yttrium Silicon Oxynitride Phases *Chemistry of Materials* **1989**, *1*, 336-338.

(7) Koroglu, A.; Thompson, D. P.; Apperley, D. C.; Harris, R. K. Oxygen/Nitrogen Ordering in Lanthanum New Phase ($La_3Si_8N_{11}O_4$) *Journal of Solid State Chemistry* **2004**, *177*, 2530-2533.

(8) Bodart, P. R. Distributions of the Quadrupolar and Isotropic Chemical Shift Interactions in Two-Dimensional Multiple-Quantum Mas Nmr Spectra *Journal of Magnetic Resonance* **1998**, *133*, 207-209.

(9) Wang, L.; Wang, X.; Takeda, T.; Hirosaki, N.; Tsai, Y.-T.; Liu, R.-S.; Xie, R.-J. Structure, Luminescence, and Application of a Robust Carbidonitride Blue Phosphor ($Al_{1-x}Si_xC_xN_{1-x}:Eu^{2+}$) for Near UV-LED Driven Solid State Lighting. *Chemistry of Materials* **2015**, *27*, 8457-8466.

(10) Shannon, R. t. Revised Effective Ionic Radii and Systematic Studies of Interatomic Distances in Halides and Chalcogenides *Acta crystallographica section A: crystal physics, diffraction, theoretical and general crystallography* **1976**, *32*, 751-767.

(11) Takeda, T.; Hirosaki, N.; Xie, R.-J.; Kimoto, K.; Saito, M. Anomalous Eu Layer Doping in Eu, Si Co-Doped Aluminium Nitride Based Phosphor and Its Direct Observation *Journal of Materials Chemistry* **2010**, *20*, 9948-9953.

(12) Shur, M. S.; Zukauskas, R. Solid-State Lighting: Toward Superior Illumination *Proceedings of the IEEE* **2005**, *93*, 1691-1703.

(13) Smet, P. F.; Parmentier, A. B.; Poelman, D. Selecting Conversion Phosphors for White Light-Emitting Diodes *Journal of the Electrochemical Society* **2011**, *158*, R37-R54.

(14) Hirosaki, N.; Xie, R.-J.; Inoue, K.; Sekiguchi, T.; Dierre, B.; Tamura, K. Blue-Emitting AlN:Eu^{2+} Nitride Phosphor for Field Emission Displays *Applied Physics Letters* **2007**, *91*, 061101.

(15) Suehiro, T.; Hirosaki, N.; Xie, R.-J.; Sato, T. Blue-Emitting $LaSi_3N_5:Ce^{3+}$ Fine Powder Phosphor for UV-Converting White Light-Emitting Diodes *Applied Physics Letters* **2009**, *95*, 051903.

(16) Brower, R. W.; Meij, S.; Serruys, P. W. A Model of Asynchronous Left Ventricular Relaxation Predicting the Bi-Exponential Pressure Decay *Cardiovascular research* **1983**, *17*, 482-488.

(17) Lu, F.; Song, X.; Liu, Q. Crystal Structure and Photoluminescence of $(La_{1-x}Ce_x)_5Si_3O_{12}N$ *Journal of Alloys and Compounds* **2011**, *509*, 2099-2104.

(18) Bachmann, V.; Ronda, C.; Meijerink, A. Temperature Quenching of Yellow Ce^{3+} Luminescence in Yag: Ce *Chemistry of Materials* **2009**, *21*, 2077-2084.

(19) Koroglu, A.; Apperley, D. C.; Harris, R. K.; Thompson, D. P. Oxygen–Nitrogen Ordering in Yttrium Nitrogen Melilite *Journal of Materials Chemistry* **1996**, *6*, 1031-1034.

(20) Daniela, S. Structural Investigation of Yam-Type Yttrium Silicon Oxynitride by 15 N Magic-Angle Spinning Nuclear Magnetic Resonance *Journal of Materials Chemistry* **1993**, *3*, 1005-1006.

(21) Tu, B.; Liu, X.; Wang, H.; Wang, W.; Zhai, P.; Fu, Z. Combining 27Al Solid-State NMR and First-Principles Simulations to Explore Crystal Structure in Disordered Aluminum Oxynitride *Inorganic Chemistry* **2016**.

(22) Fitzgerald, J. J.; Kohl, S. D.; Piedra, G.; Dec, S. F.; Maciel, G. E. Observation of Four-Coordinate Aluminum Oxynitride ($AlO_{4-x}N_x$) Environments in AlON Solids by MAS ^{27}Al NMR at 14 T *Chemistry of Materials* **1994**, *6*, 1915-1917.

(23) Dierre, B.; Xie, R.-J.; Hirosaki, N.; Sekiguchi, T. Blue Emission of Ce^{3+} in Lanthanide Silicon Oxynitride Phosphors *Journal of Materials Research* **2007**, *22*, 1933-1941.

(24) Van Krevel, J.; Hintzen, H.; Metselaar, R. On the Ce^{3+} Luminescence in the Melilite-Type Oxide Nitride Compound $Y_2Si_{3-x}Al_xO_{3+x}N_{4-x}$ *Materials Research Bulletin* **2000**, *35*, 747-754.

(25) Grabmaier, B. *Luminescent Materials*; Springer Verlag, **1994**.

(26) Dorenbos, P. The $4f^n \leftrightarrow 4f^{n-1}5d$ Transitions of the Trivalent Lanthanides in Halogenides and Chalcogenides *Journal of Luminescence* **2000**, *91*, 91-106.

(27) Dorenbos, P. Thermal Quenching of Eu^{2+} 5d-4f Luminescence in Inorganic Compounds *Journal of Physics: Condensed Matter* **2005**, *17*, 8103.

(28) Hecht, H. G. The Interpretation of Diffuse Reflectance Spectra *Journal of research of the National Bureau of Standards A*, **1976**; 80A, 567-583.

(29) Tang, J.-Y.; Xie, W.-J.; Huang, K.; Hao, L.-Y.; Xu, X.; Xie, R.-J. A High Stable Blue $BaSi_3Al_3O_4N_5:Eu^{2+}$ Phosphor for White Leds and Display Applications *Electrochemical and Solid-State Letters* **2011**, *14*, J45-J47.

(30) McKittrick, J.; Hannah, M.; Piquette, A.; Han, J.; Choi, J.; Anc, M.; Galvez, M.; Lugauer, H.; Talbot, J.; Mishra, K. Phosphor Selection Considerations for near-UV LED Solid State Lighting *ECS Journal of Solid State Science and Technology* **2013**, *2*, R3119-R3131.

Chapter 6 Discovery of a new Sr-sialon phase and the photoluminescence properties when doped with Eu or Ce

6.1 Introduction

Several lanthanide doped nitride and oxynitride phosphors promising for white LED application in terms of luminescence efficiency and emission wavelength have been developed. However, some challenges still remain. One of them is the thermal quenching caused by thermal ionization, when the phosphors are subject to higher temperatures for longer time. In addition, there is also still a lack of highly efficient deep blue emission phosphors to get different types of white light.[1-2] New phosphors that can meet these requirements are highly demanded.

In order to discover new phosphors, several methods have been developed, such as mineral-inspired prototype evolution and new phase construction,[3] heuristics-assisted combinatorial chemistry[4] and the single particles diagnosis approach[5-6]. With the single-particle diagnosis approach, several types of nitride and oxynitride phosphors have been discovered, such as $Ba_5Si_{11}Al_7N_{25}$:Eu,[5] $BaSi_4Al_3N_9$:Eu,[5] $Ba_2LiSi_7AlN_{12}$:Eu,[1] $Sr_2B_{2-2x}Si_{2+3x}Al_{2-x}N_{8+x}$:Eu,[7] $Sr_3Si_{8-x}Al_xO_{7+x}N_{8-x}$:Eu,[8] $Ca_{1.62}Eu_{0.38}Si_5O_3N_6$[9] and $Eu_{3.6}LiSi_{11.4}Al_8O_{10.4}N_{19}$[10]. $Eu_{3.6}LiSi_{11.4}Al_8O_{10.4}N_{19}$ crystallizes in an trigonal structure with space group P3m1, as shown in Figure 6.1. The lattice parameters are a = 12.1164(6) and c = 4.8876(3), $\alpha = \beta = 90°$, $\gamma = 120°$. The $Eu_{3.6}LiSi_{11.4}Al_8O_{10.4}N_{19}$ structure approaches a structure with the composition $Eu_3Li(Si,Al)_{19}(O,N)_{29}$, but contains additional disorder. [10]

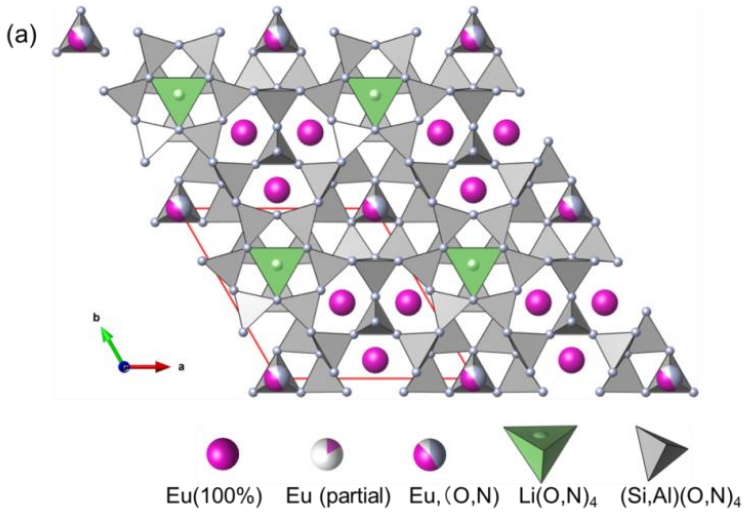

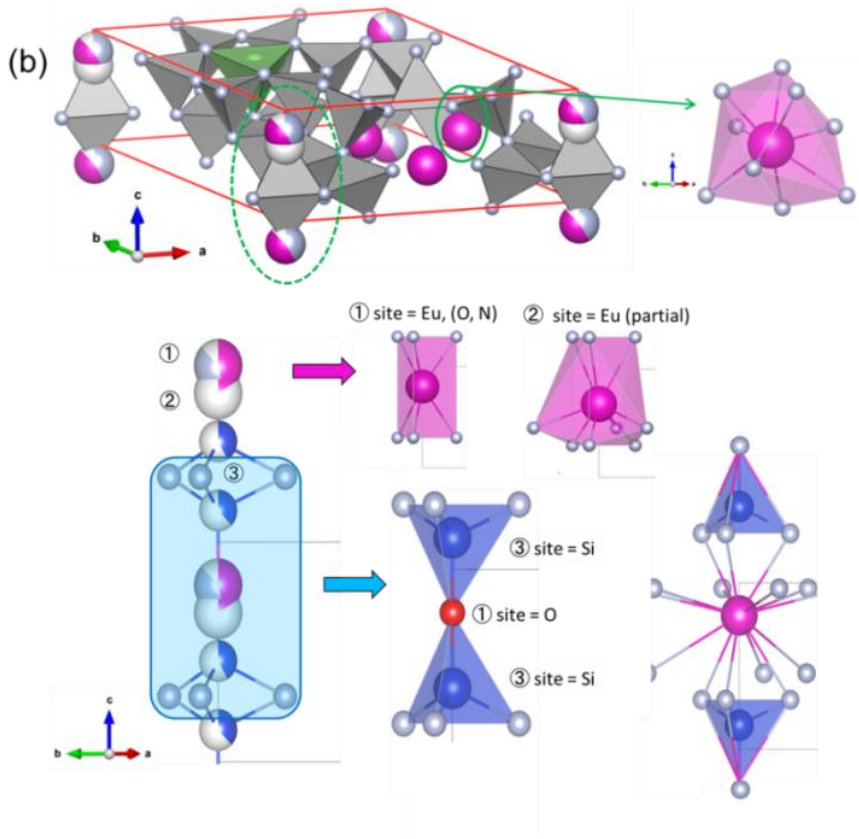

Figure 6.1 Crystal structure of a new Eu-sialon phase $Eu_{3.6}LiSi_{11.4}Al_8O_{10.4}N_{19}$ (a) and local coordination of Eu atoms (b).[10]

In this work, the discovery of a new Sr-sialon phase is reported, of which the structure resembles that of $Eu_{3.6}LiSi_{11.4}Al_8O_{10.4}N_{19}$. The photoluminescence properties of Eu and Ce doped new Sr-sialon phosphors are investigated, including photoluminescence spectra, thermal quenching, quantum efficiency and luminescence decay.

6.2 Experimental section

6.2.1 Synthesis

The new Sr-sialon phase phosphors doped with Eu or Ce have been prepared by solid-state reaction synthesis. For the synthesis of Eu doped new Sr-sialon phase, the $SrCO_3$, α-Si_3N_4, AlN and Eu_2O_3 starting materials were mixed in the designed chemical compositions. The Ce doped new Sr-sialon phase phosphors were prepared in a similar way using CeO_2 instead of Eu_2O_3. For these phosphors, Li_2CO_3

was added in a 1:2 molar ratio with CeO_2 for charge compensation. The starting materials were thoroughly mixed with pestle and mortar in air and then put in a boron nitride crucible. The samples were heated in a gas pressure furnace at 0.92 MPa for 2 hours at a temperature of 1850 °C. After synthesis, the samples were crushed to powder before characterization.

6.2.2 Measurements

All the measurements on the powder samples described in this chapter have been performed according to the descriptions of Chapter 2. The photoluminescence spectra of a single luminescent particle were measured using a micro-spectroscopic method.[5] The luminescence from the particle after 365 nm excitation of an UV-LED was observed by a spectrometer (Otsuka electronics, MCPD7700) through a microscope (Olympus, BX51M).

6.3 Results and discussion

6.3.1 Discovery of a new Sr-sialon phase

In an attempt to synthesize a Sr-JEM phase with a nominal composition of $Sr_{0.95}Si_5Al_2O_{1.025}N_{8.65}$:0.05Eu, it was found that JEM ($LaAl_2Si_5ON_9$) phase did not form at all, as shown in Figure 6.2. Instead, the main phase formed crystallizes in a phase isostructural to $Eu_{3.6}LiSi_{11.4}Al_8O_{10.4}N_{19}$ that was found by the single particle diagnosis approach.[10] At the time, the Sr-containing variant of this phase had not yet been reported. In addition to the new Sr-sialon phase, the sample contained a small amount of a Sr-containing sialon polytypoid phase ($SrSi_{10-x}Al_{18+x}O_xN_{32-x}$, $x \approx 1$)[11].

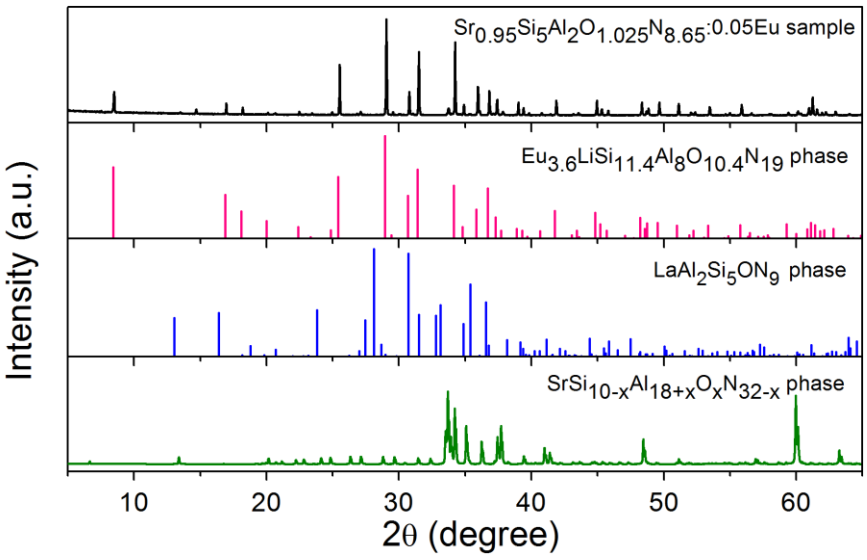

Figure 6.2 XRD pattern of sample with a nominal composition of $Sr_{0.95}Si_5Al_2O_{1.025}N_{8.65}$:0.05Eu and the candidate phases including $Eu_{3.6}LiSi_{11.4}Al_8O_{10.4}N_{19}$ (calculated pattern from the crystal structure model), and $SrSi_{10-x}Al_{18+x}O_xN_{32-x}$ ($x \approx 1$). $LaAl_2Si_5ON_9$ (JEM) phase is added for comparison.

6.3.2 Phase purity and microstructure of Eu doped new Sr-sialon phosphors

In order to improve the phase purity of the new Sr-sialon phase sample, the chemical composition of the starting materials was changed by following $0.95SrCO_3$ ~ m/3 Si_3N_4 ~ n AlN ~ 0.025 Eu_2O_3. An overview of the attempted starting compositions is shown in Table 6.1 and the XRD patters of various compositions are shown in Figure 6.3.

Table 6.1 Compositions of starting materials to prepare Eu doped new Sr-sialon phase samples

Sample No.	m	n	$SrCO_3$	Si_3N_4	AlN	Eu_2O_3
1	5.0	2.0	0.6034	1.0060	0.3527	0.0379
2	4.5	2.0	0.6354	0.9533	0.3714	0.0399
3	5.0	1.5	0.6313	1.0524	0.2768	0.0396
4	4.5	1.5	0.6663	0.9997	0.2921	0.0418

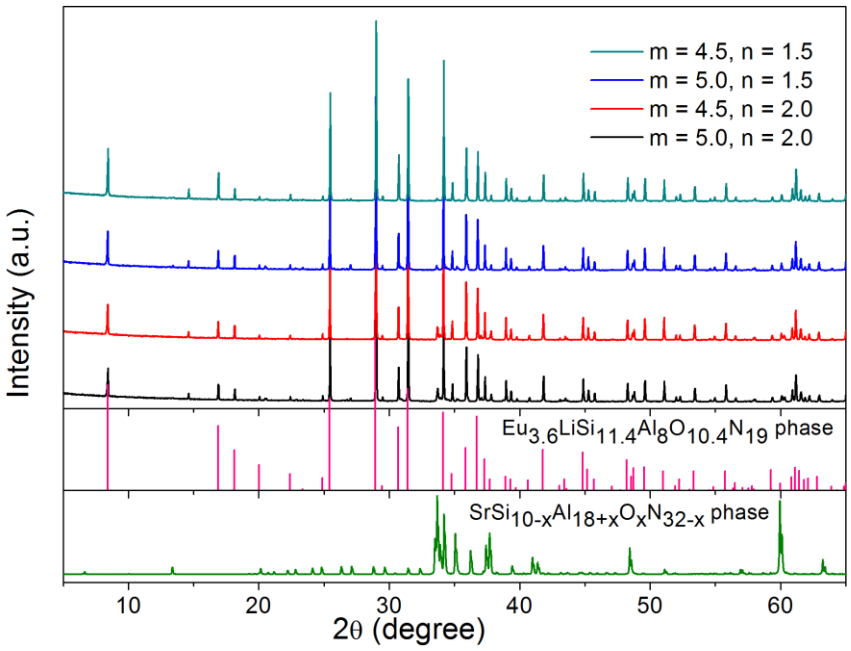

Figure 6.3 XRD of 5% Eu doped Sr-sialon phase samples using different compositions shown in Table 6.1.

The sample (No. 4) with m = 4.5 and n = 1.5 has the highest purity. The amount of $SrSi_{10-x}Al_{18+x}N_{32-x}O_x$ impurity has been reduced significantly by changing m and n values. This sample was used for the luminescence measurements and samples with other Eu concentrations were made by using the same Si/Al/O/N ratio.

The X-ray diffraction (XRD) pattern of a 5% Eu doped new Sr-Sialon phase sample (No.4 sample) is shown in Figure 6.4. A nearly single new Sr-sialon phase sample has been obtained, only a trace amount of $SrSi_{10-x}Al_{18+x}O_xN_{32-x}$ ($x \approx 1$) can be detected. It is worthwhile to emphasize that Li is not added in these samples. This suggests that the new Sr-sialon phase is stable with Li vacancy. Ignoring the trace amount of impurity, the composition of the new Sr-sialon phase is expressed as $Sr_{3.6}Si_{16.2}Al_{5.4}O_{3.6}N_{27}$.

In order to check the microstructure of 5% Eu doped new Sr-sialon phase phosphor, SEM was measured, as shown in Figure 6.5. The particles have a rod-like morphology with a length of 8 to 15 μm and a diameter of a few μm.

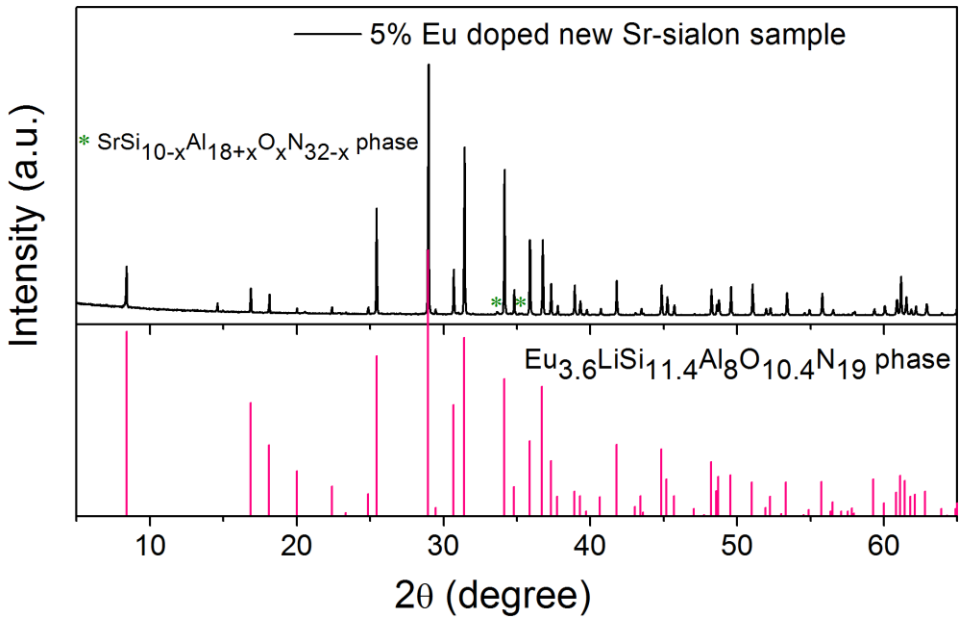

Figure 6.4 XRD pattern of the 5% Eu doped new Sr-sialon sample.

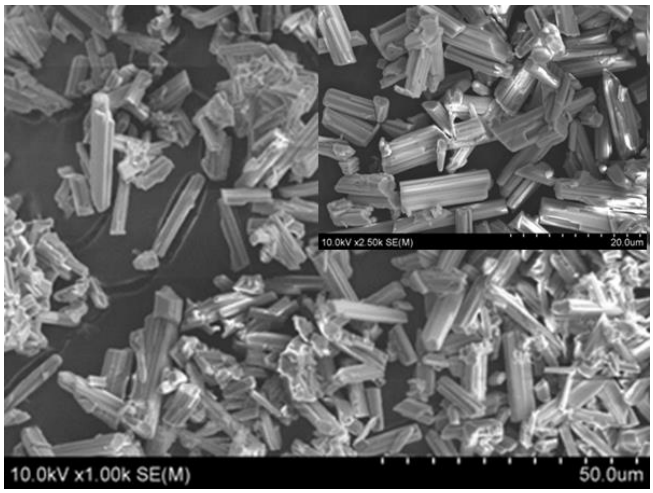

Figure 6.5 SEM image of 5% Eu doped new Sr sialon phase phosphor.

6.3.3 Luminescence properties of Eu doped new Sr-sialon phase phosphors

(1) Photoluminescence spectra of 5% Eu doped new Sr-sialon phase phosphor

The excitation and emission spectra of a 5% Eu doped new Sr-sialon phase powder sample are shown in Figure 6a. When exciting with 355 nm light, a broad emission band is observed with a maximum at 514 nm, giving a green emission color. This band is typical Eu^{2+} emission from the 5d excited state to the 4f ground state, indicating that Eu is present in the divalent state. The band has a full-width at half maximum (FWHM) of 101 nm and is asymmetrical. The emission band can be fit with two Gaussian curves with maxima at 506 nm (2.45 eV) and 546 nm (2.27eV), as shown in the inset of Figure 6a. The two bands can be attributed to Eu on at least two different sites. The excitation spectrum of the 514 nm emission shows a broad band from the UV extending up to 500 nm, which is the Eu^{2+} 4f-5d absorption band. These results indicate that the new Sr-sialon phase doped with Eu can be excited with UV or blue light, emitting green light. The emission spectrum of a Eu doped new Sr-sialon phosphor particle as shown in Figure 6b, is similar to that of powder sample indicating that the emission by the powder sample is not affected by the small impurity.

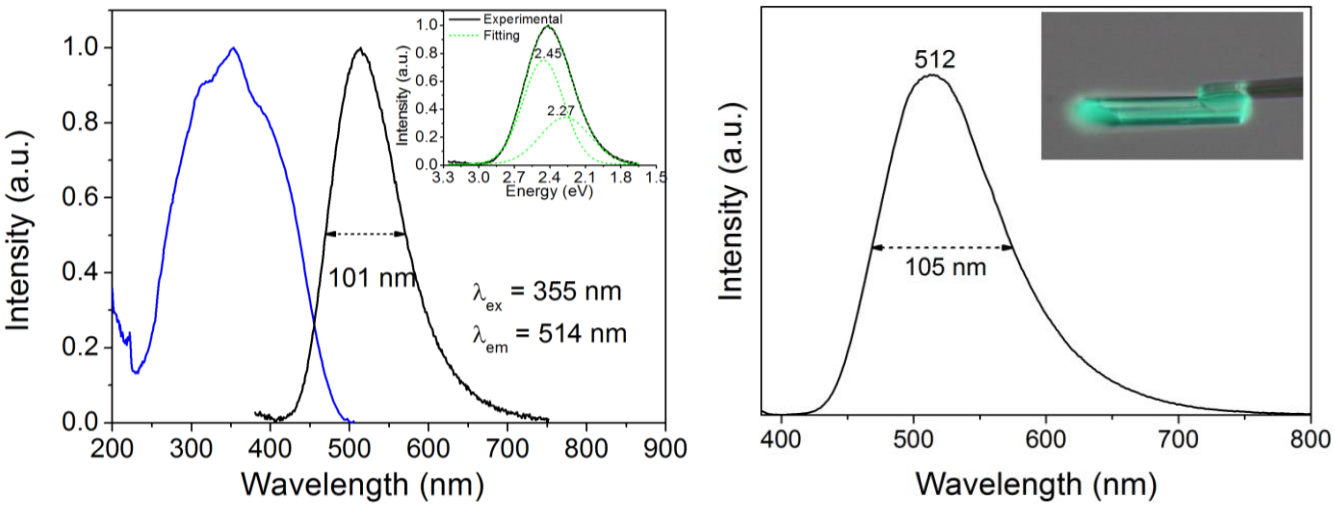

(a) (b)

Figure 6.6 (a) The excitation spectrum (monitoring the 514 nm emission) and emission spectrum (excited at 355 nm) of 5% Eu doped new Sr-sialon phase sample. The inset shows the fitted emission spectrum of the same sample. (b) The emission spectrum of a Eu doped the new Sr-sialon phosphor particle when excited at 355 nm and a luminescence photo when irradiated with a 365 nm UV LED.

(2) Luminescence decay of 5% Eu doped new Sr-sialon phase phosphor

As shown in Figure 6.7, the luminescence decay curves display a non-linear decay, which monitor 506 and 546 nm emissions after 370 nm excitation for 5% Eu doped new Sr-sialon sample. As there are two types of Eu luminescence centers discussed before, the luminescence decay curve can be reasonably fitted with a bi-exponential function:

$$I(t) = A_1 \exp(-t/\tau_1) + A_2 \exp(-t/\tau_2)$$

where I is the luminescence intensity; A_1 and A_2 are constants; t is the time; and τ_1 and τ_2 are the lifetimes for the exponential components. The 506 nm emission shows much faster decay than 546 nm emission, indicating that the high energy site has a faster decay rate than the low energy site. The effective decay times τ with 0.65 μs and 0.85μs for 506 nm and 546 nm emissions respectively can be obtained by following the formula:

$$\tau = (A_1\tau_1^2 + A_2\tau_2^2) / (A_1\tau_1 + A_2\tau_2)$$

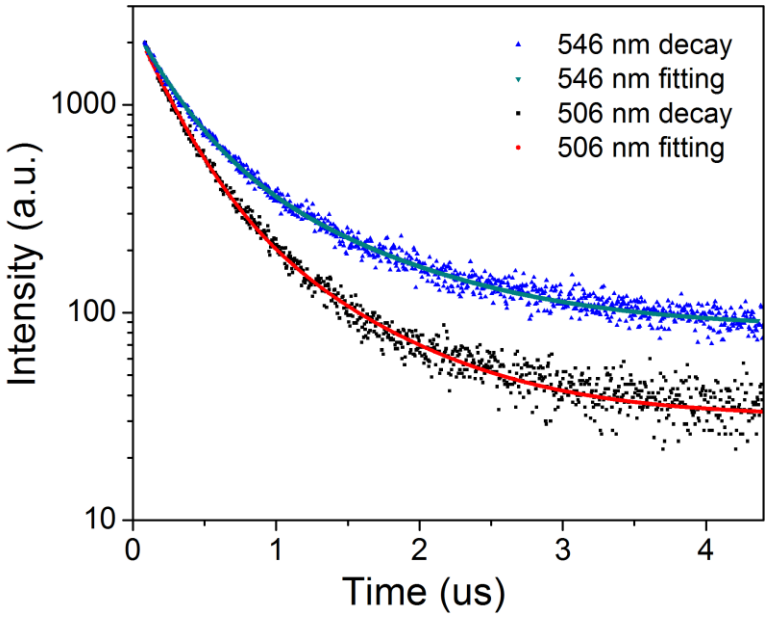

Figure 6.7 Time-resolved photoluminescence monitoring 506 and 546 nm emissions after 370 nm excitation for 5% Eu doped new Sr-sialon phosphor.

(3) Eu concentration dependent photoluminescence properties

In Figure 6.8 the excitation and emission spectra of the new Sr-sialon phase doped with different Eu concentrations are shown. The position of the emission band maximum shifts from 482 nm for a 0.5% Eu doped sample to 535 nm for a 25% Eu doped sample, changing the emission from blue to green. A redshift is typically observed with increasing amount of Eu^{2+} as a result of a lowering of the 5d level in combination with reabsorption of emission light. In addition, the redshift of the emission with increasing Eu concentration may be enhanced for the new Sr-sialon phase because of the presence of Eu on two different sites with different energy. With increasing Eu concentration the energy transfer from the high energy site to the low energy site is enhanced, causing a redshift. The emission intensity of the new Sr-sialon phosphors initially increases with increasing Eu concentration due to higher absorption strength, reaching a maximum in luminescence intensity for a 3% Eu doped sample. For higher Eu concentrations, the emission intensity starts to decrease as a result of concentration quenching. The excitation bands of the samples become broader with increasing Eu concentration, which is typically observed for Eu^{2+} doped samples.

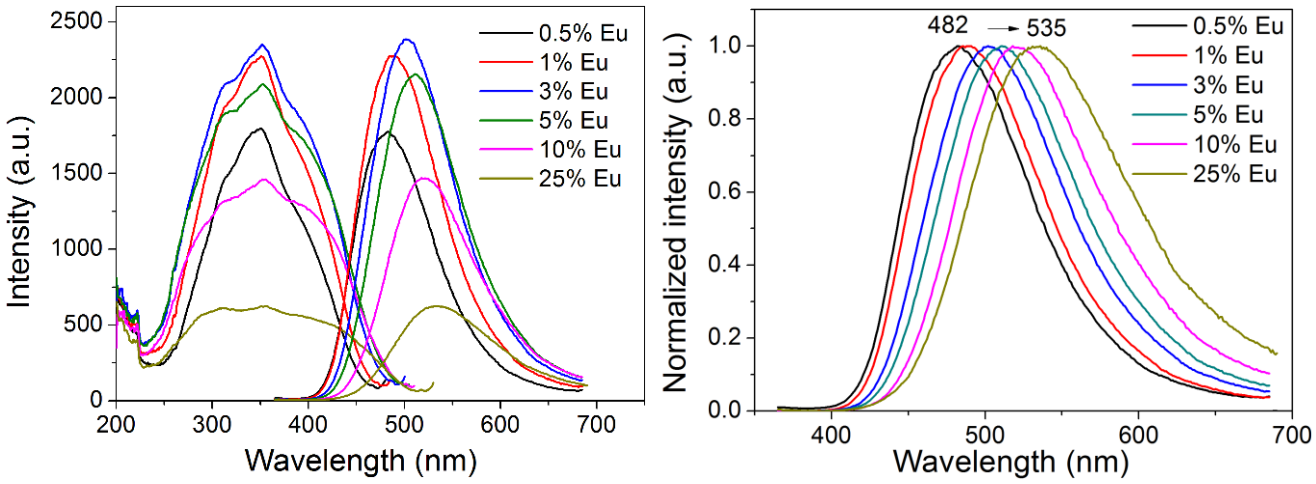

(a) (b)

Figure 6.8 (a) Excitation (monitoring the emission maxima) and emission spectra (excited with 355 nm light) of the new Sr-sialon phosphors for different Eu concentrations; (b) normalized emission spectra of the same samples.

(4) Thermal quenching of 1% Eu doped new Sr-sialon phosphor

The temperature dependency between 4 K and 573 K of the emission for the 1% Eu doped new Sr-sialon phase phosphor is shown in Figure 6.9. Starting from 4 K, the emission intensity remains constant up to 150 K and then starts to quench slowly with temperature. At room temperature about 30% of the emission intensity has been quenched and at 573 K the emission intensity has decreased to 16% compared to the original intensity at 4 K. Together with the decrease in intensity with increasing temperature, a blue shift of the emission is observed with the maximum shifting from 493 nm at 4 K to 464 nm at 573 K. The blue shift of the emission indicates that the emission from Eu^{2+} ions located on the high energy site is more thermally stable than the emission from Eu^{2+} ions located on the low energy site.

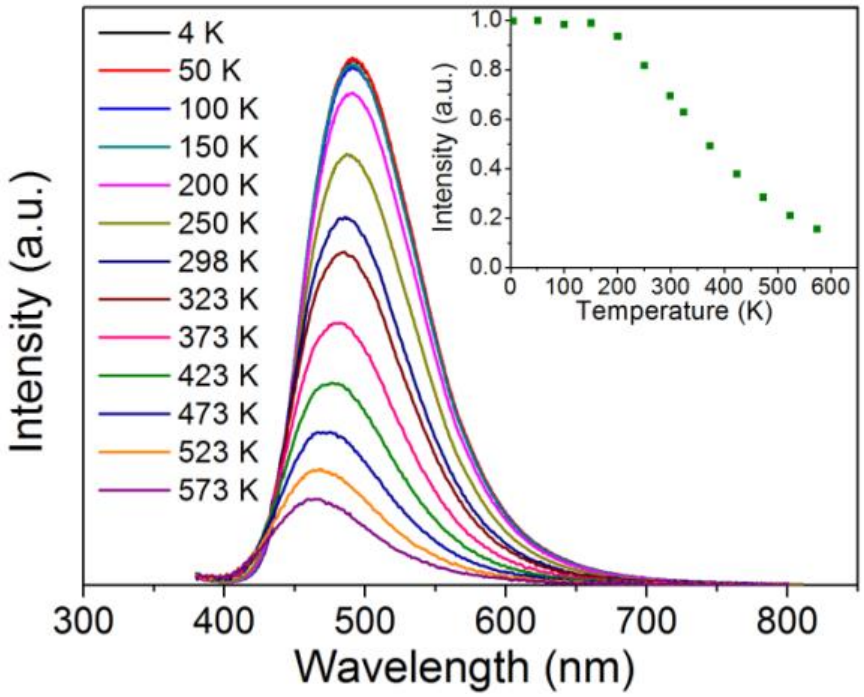

Figure 6.9 Temperature dependent emission spectra of 1% Eu doped new Sr-sialon phase phosphor after 355 nm excitation. In the inset the integrated intensity of the emission spectra is shown as a function of temperature.

(5) Quantum efficiency

The quantum efficiencies of the 1%, 3% and 5% Eu doped new Sr-sialon phase samples at room temperature are listed in Table 6.2. The internal quantum efficiency is relatively low, reaching 30% for a 1% Eu doped sample and 22% for a 5% Eu doped sample. This can be partly explained by the thermal quenching discussed above, as about 30% of the luminescence is quenched at room temperature as compared to 4 K. As there are disorders in the structure, the local defects may also play a role in quenching luminescence.

Table 6.2 Absorbance, internal and external quantum efficiency of the Eu doped new Sr-sialon phase phosphors when excited at 355 nm.

Eu concentration (%)	Abs. (%)	IQE (%)	EQE (%)
1	68.33	30.34	20.73
3	76.77	25.63	19.68
5	81.21	21.80	17.70

6.3.4 Structural properties of Ce,Li co-doped new Sr-sialon phase

5% Ce and 5% Li co-doped new Sr-sialon sample was prepared with the starting materials by following $0.95SrCO_3$ ~ 1.5 Si_3N_4 ~ 1.5 AlN ~ 0.025 Li_2CO_3 ~ $0.05CeO_2$. Since Ce^{3+} ions occupy Sr^{2+} sites, Li is added for charge compensation. From the XRD pattern shown in Figure 6.10, one can see a nearly single phase sample has been obtained and only a little $SrSi_{10-x}Al_{18+x}O_xN_{32-x}$ impurity phase can be detected, which is similar to Eu doped new Sr-sialon samples.

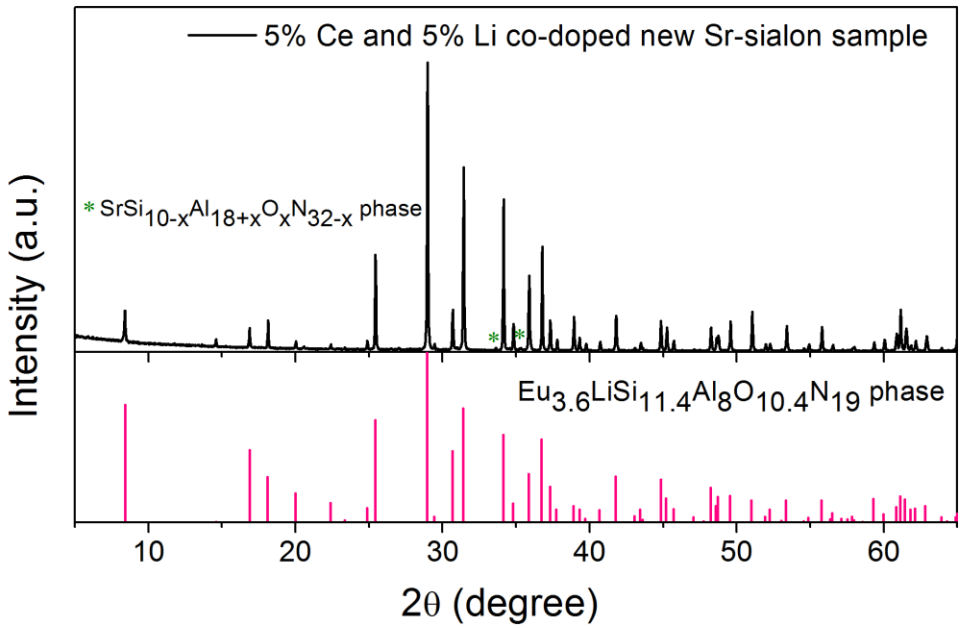

Figure 6.10 The XRD pattern of 5% Ce and 5% Li co-doped new Sr-sialon sample.

6.3.5 Photoluminescence properties of Ce, Li co-doped new Sr-sialon phosphors

(1) Photoluminescence spectra of 5% Ce and 5% Li co-doped new Sr-sialon phosphor

The excitation and emission spectra of 5% Ce and 5% Li co-doped new Sr-sialon phase are shown in Figure 6.11. Excitation with UV light results in blue light emission. The emission band has a maximum at 438 nm and a FWHM of 89 nm, which is the typical Ce^{3+} 5d-4f emission. The excitation spectrum of this band shows the typical 4f-5d absorption bands of Ce^{3+} which extend up to about 425 nm and have a maximum at 355 nm.

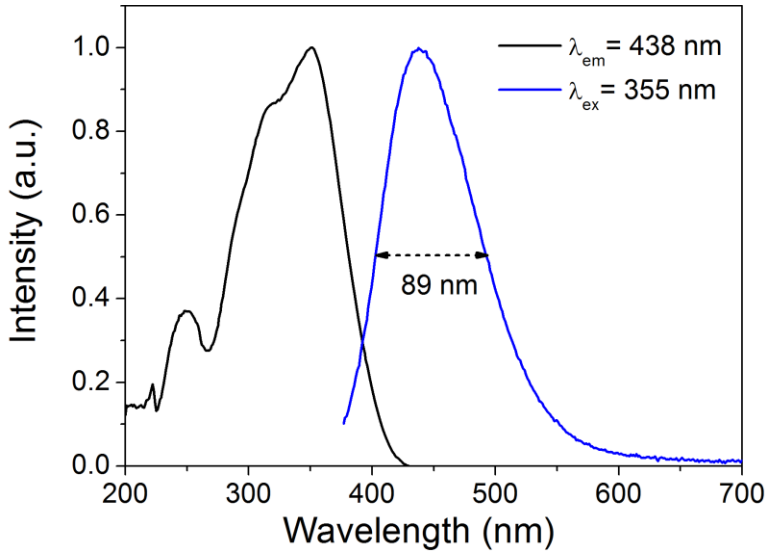

Figure 6.11 Excitation (monitoring the 438 nm emission) and emission spectrum (excited at 355 nm) of 5% Ce,Li doped new Sr-sialon phase.

(2) Ce and Li concentration dependent properties

The samples with different Ce concentrations were prepared by keeping the same Si/Al ratio (1.5 Si_3N_4 ~ 1.5 AlN). Li is added for charge compensation, which has the same concentration with Ce. The XRD patterns shown in Figure 6.12 indicate the main phase of 25% Ce doped sample is still the new Sr-sialon phase. Compared to 5% doped sample, the amount of impurity phase $SrSi_{10-x}Al_{18+x}O_xN_{32-x}$ slightly increases for 25% Ce,Li doped sample, and a small amount of unknown phase forms as well.

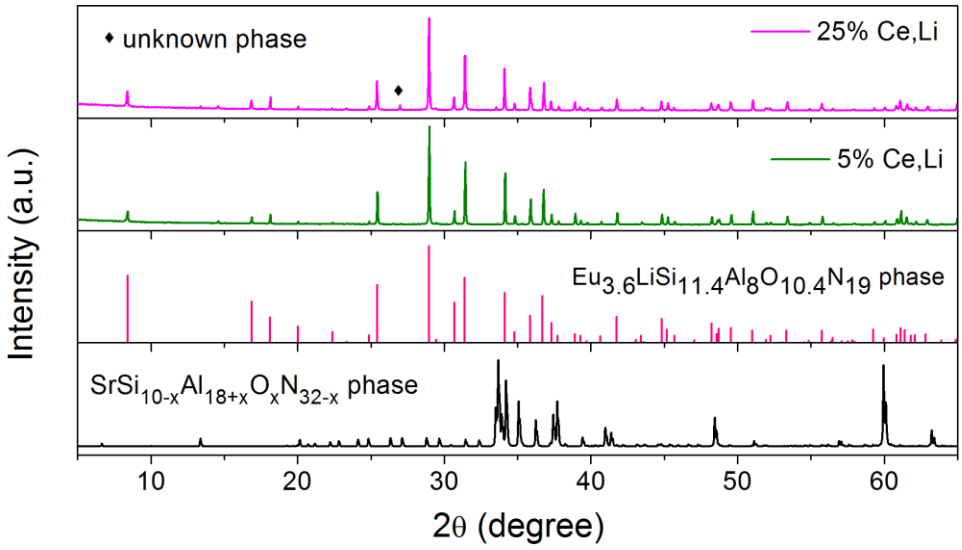

Figure 6.12 XRD patterns of 5% and 25% Ce,Li co-doping new Sr-sialon phase samples.

With increasing the Ce concentration, the position of the Ce^{3+} 5d-4f emission band in the Ce doped new Sr-sialon phase phosphors shifts from 424 nm for 0.5% Ce doping to 445 nm for a 25% Ce doped sample, as shown in Figure 6.13. The shift of the emission band with varying Ce concentration is thus much smaller (21 nm) than for the Eu doped samples (53 nm). The difference can be explained by the fact that the Ce maybe only located on one type of Sr site in the lattice or the energy difference of two Ce sites is much smaller than that for Eu sites, considering the emission band is much narrower for Ce doping than Eu doping.

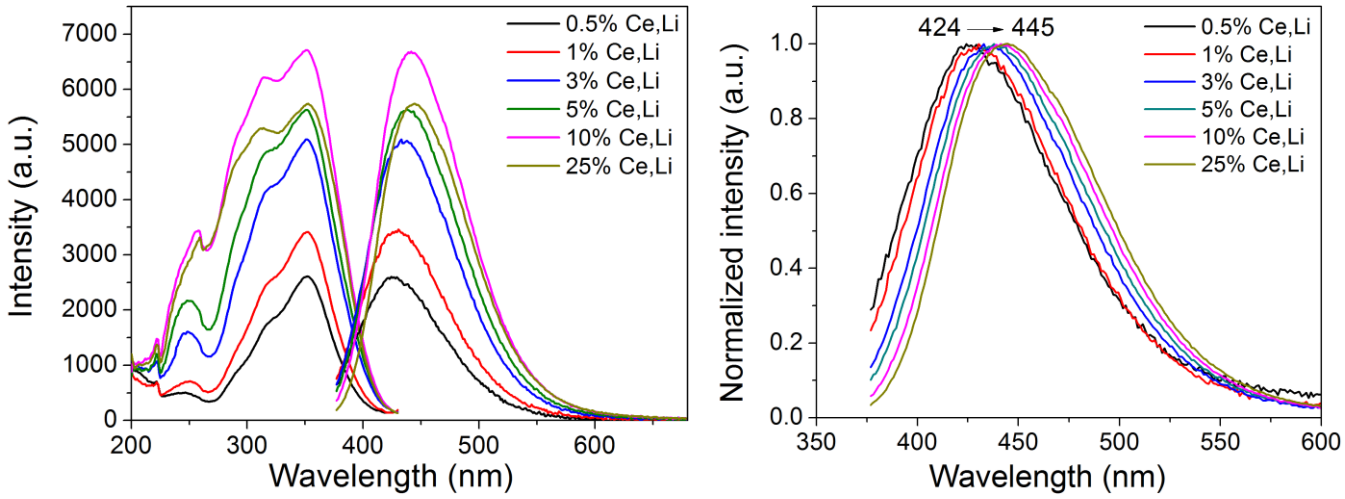

(a) (b)

Figure 6.13 (a) Excitation (monitoring the emission maxima) and emission spectra (excited at 355 nm) of the new Sr-sialon phosphors for different Ce concentrations; (b) normalized emission spectra of the same samples.

In Figure 6.14 the efficiency of the Ce doped new Sr-sialon phase phosphors is shown as a function of the Ce concentration. The highest internal quantum efficiency (IQE) of 64% is obtained for a 5% Ce doped sample. The external quantum efficiency is highest for the 10% Ce doped sample with an efficiency of 47%. The Ce doped phosphors are thus much more efficient than the Eu doped phosphors.

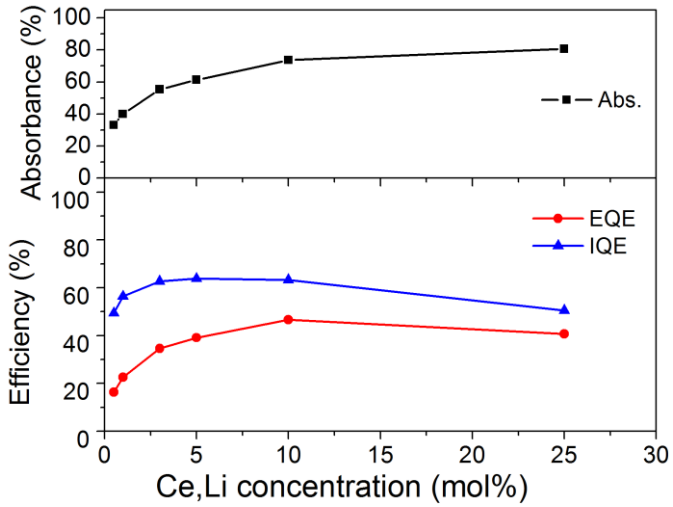

Figure 6.14 Internal quantum efficiency (IQE), external quantum efficiency (EQE) and absorption efficiency (Abs.) of the Ce doped new Sr-sialon phase phosphors as a function of the Ce concentration.

The thermal quenching of Ce doped new Sr-sialon phase phosphor is shown in Figure 6.15. For the 1% Ce doped sample, the emission intensity is stable when the sample is heated from 4 K to 250 K. Above 250 K the intensity slowly drops to 97% at room temperature and to 42% at 673 K. The emission of the Ce doped sample is thus more thermally stable than that of the Eu doped sample and much less of the emission is quenched at room temperature. This is in accordance with the higher quantum efficiency of the Ce doped sample as compared to the Eu doped sample. The position of the Ce^{3+} 5d-4f emission band does not show any shift with temperature.

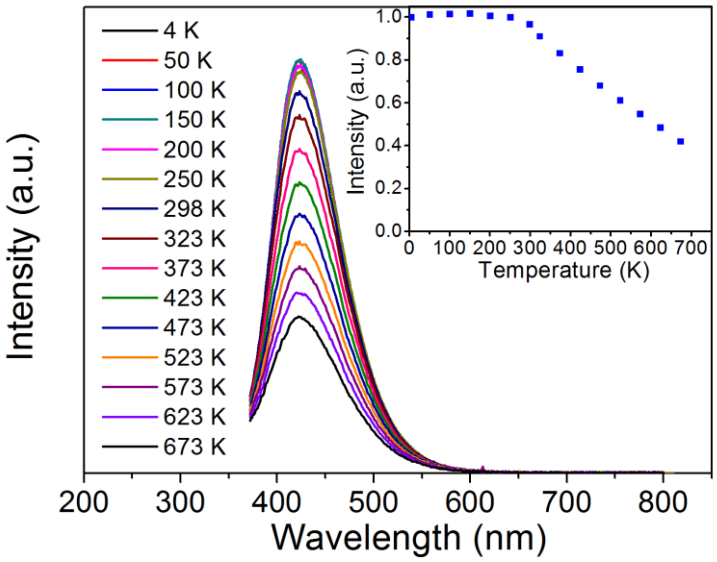

Figure 6.15 Temperature dependent emission spectra (425 nm) of 1% Ce, Li doped new Sr-sialon phase after 355 nm excitation. In the inset the integrated intensity of the emission spectra is shown as a function of temperature.

6.4 Conclusions

A new Sr-sialon phase $Sr_{3.6}Si_{16.2}Al_{5.4}O_{3.6}N_{27}$ was discovered with a solid-state reaction method at 1850 °C. Eu doped new Sr sialon phase shows blue to green emission after UV excitation when Eu concentration is ranged from 0.5% to 25%. After 355 nm excitation, 5% Eu doped new Sr-sialon phase phosphor displays a broad emission band with a FWHM = 101 nm centered at 514 nm. This phosphor has a relatively fast thermal quenching, resulting in a low quantum efficiency. With Ce,Li co-doping, the emission is in the deep blue region (424 – 445 nm) with a much smaller redshift upon increasing the concentration and a narrower emission band (FWHM = 89 – 90 nm) as compared to the Eu doped new phase. 1% Ce,Li doped new Sr-sialon phase phosphor shows better thermal stability than Eu doped one, and only 3% of luminescence is quenched at room temperature as compared to the intensity at 4 K. When the temperature is increased to 573 K, there is still 55% of luminescence left. An internal efficiency up to 64% can be achieved for a 5% Ce,Li doped new Sr-sialon phase sample. These performances indicate that Ce,Li doped new Sr-sialon phase phosphor is a promising deep blue-emitting phosphor for high color rendering white LEDs.

6.5 References

(1) Takeda, T.; Hirosaki, N.; Funahshi, S.; Xie, R.-J. Narrow-Band Green-Emitting Phosphor $Ba_2LiSi_7AlN_{12}:Eu^{2+}$ with High Thermal Stability Discovered by a Single Particle Diagnosis Approach *Chemistry of Materials* **2015**, *27*, 5892-5898.

(2) Pust, P.; Wochnik, A. S.; Baumann, E.; Schmidt, P. J.; Wiechert, D.; Scheu, C.; Schnick, W. Ca $[LiAl_3N_4]:Eu^{2+}$ – a Narrow-Band Red-Emitting Nitridolithoaluminate *Chemistry of Materials* **2014**, *26*, 3544-3549.

(3) Xia, Z.; Xu, Z.; Chen, M.; Liu, Q. Recent Developments in the New Inorganic Solid-State Led Phosphors *Dalton Transactions* **2016**, *45*, 11214-11232.

(4) Park, W. B.; Shin, N.; Hong, K. P.; Pyo, M.; Sohn, K. S. A New Paradigm for Materials Discovery: Heuristics - Assisted Combinatorial Chemistry Involving Parameterization of Material Novelty *Advanced Functional Materials* **2012**, *22*, 2258-2266.

(5) Hirosaki, N.; Takeda, T.; Funahashi, S.; Xie, R.-J. Discovery of New Nitridosilicate Phosphors for Solid State Lighting by the Single-Particle-Diagnosis Approach *Chemistry of Materials* **2014**, *26*, 4280-4288.

(6) Takeda, T.; Hirosaki, N.; Funahashi, S.; Xie, R.-J. New Phosphor Discovery by the Single Particle Diagnosis Approach *Materials Discovery* **2015**, *1*, 29-37.

(7) ten Kate, O. M.; Xie, R.-J.; Wang, C.-Y.; Funahashi, S.; Hirosaki, N. Eu^{2+}-Doped $Sr_2B_{2-2x}Si_{2+3x}Al_{2-x}N_{8+x}$: A Boron-Containing Orange-Emitting Nitridosilicate with Interesting Composition-Dependent Photoluminescence Properties *Inorganic Chemistry* **2016**, *55*, 11331-11336.

(8) Wang, X.-J.; Wang, L.; Takeda, T.; Funahashi, S.; Suehiro, T.; Hirosaki, N.; Xie, R.-J. Blue-Emitting $Sr_3Si_{8-x}Al_xO_{7+x}N_{8-x}$:$Eu^{2+}$ Discovered by a Single-Particle-Diagnosis Approach: Crystal Structure, Luminescence, Scale-up Synthesis, and Its Abnormal Thermal Quenching Behavior *Chemistry of Materials* **2015**, *27*, 7689-7697.

(9) Wang, X.-J.; Funahashi, S.; Takeda, T.; Suehiro, T.; Hirosaki, N.; Xie, R.-J. Structure and Luminescence of a Novel Orange-Yellow-Emitting $Ca_{1.62}Eu_{0.38}Si_5O_3N_6$ Phosphor for Warm White LEDs, Discovered by a Single-Particle-Diagnosis Approach *Journal of Materials Chemistry C* **2016**, *4*, 9968-9975.

(10) Shiro Funahashi, T. Takeda., Naoto Hirosaki, Rong-Jun Xie Crystal Structure Analysis of the $A_{4-x}B_yC_{19+x}$ X_{29+x} Type New Oxynitride Phosphor, *The 64th JSAP Spring Meeting*, Yokohama, Japan, **2017**.

(11) Grins, J.; Esmaeilzadeh, S.; Svensson, G.; Shen, Z. J. High-Resolution Electron Microscopy of A Sr-Containing Sialon Polytypoid Phase *Journal of the European Ceramic Society* **1999**, *19*, 2723-2730.

Chapter 7 Conclusions and outlook

The research described in this thesis encompasses the synthesis and optical and structural characterization of novel UV excitable phosphors. This enables the development of UV excitable phosphor-converted white LEDs, which will be more energy efficient and environmental friendly than traditional light sources. At the same time the UV excitable LED will have higher color rendering and color stability as compared to other types of white LEDs, which is necessary for the wide spread application of energy efficient high grade white light sources for home illumination. The work has focused on the development of lanthanide (Ce^{3+} and Eu^{2+}) doped silicon aluminum oxy-nitride (sialon) phosphors, because of their structural variability, optical tunability, chemical stability and high luminescence efficiency. However, many problems still remain, such as a low phase purity of promising phosphors and a lack of highly efficient and thermally stable deep blue emitting phosphors. The research carried out in this thesis aimed at solving these problems. The phosphors that have been studied in this research are the Eu^{2+} and Ce^{3+} doped $LaAl(Si_{6-z}Al_z)(N_{10-z}O_z)$ (termed as JEM), Ce^{3+} doped $La_3Si_{8-x}Al_xN_{11-x}O_{4+x}$ (termed as Al containing La N-phase), a newly discovered Sr sialon phase $Sr_{4-x}(Si,Al)_{19+x}(N,O)_{29+x}$ doped with Eu^{2+} and Ce^{3+}.

The phase purity of the green-emitting Eu^{2+} doped $LaAl(Si_{6-z}Al_z)(N_{10-z}O_z)$ (termed as JEM, $z \sim 1$) was improved by the careful control of sintering temperature and chemical composition of starting materials (z value; N/O ratio and Si/Al ratio), resulting in the synthesis of a single phase JEM phosphor for the first time. The emission of the JEM:Eu^{2+} phosphor upon UV excitation shifts from blue to green depending on Eu concentration. The emission has an abnormal nearly linear decrease of intensity with increasing temperature, and a non-linear decay behavior. These give strong evidences for two emission sites in Eu^{2+} doped JEM phosphor, attributed to disorder in the structure. Nearly single phase JEM:Ce phosphors have been obtained as well. JEM:Ce displays blue emission after UV excitation with higher internal quantum efficiency (up to 75%) and better thermal stability as compared to JEM:Eu phosphor. The Yb^{3+} and Sm^{3+} charge transfer transitions and the presence of divalent and trivalent Yb and Sm in JEM have been investigated. Combined with the thermal quenching data of Eu and Ce, an energy scheme has been constructed, showing the energy level positions of the lanthanide 4f and 5d states with respect to the valence band of JEM.

$La_3Si_{8-x}Al_xN_{11-x}O_{4+x}$ (x = 1.5) Al-containing La N(ew)-phase single phase non-doped material and Ce doped phosphors have been synthesized for the first time, allowing analysis of local structure by NMR. High resolution solid-state NMR spectra of ^{29}Si and ^{27}Al show that $La_3Si_{6.5}Al_{1.5}N_{9.5}O_{5.5}$ has [SiN_4], [SiN_3O], [SiN_2O_2] silicon environments, and [AlN_3O], [AlN_2O_2], [$AlNO_3$] aluminum environments, which are in good agreement with the crystal structure model of $La_3Si_{6.5}Al_{1.5}N_{9.5}O_{5.5}$. The Ce doped Al containing N-phase phosphor displays a narrow deep blue emission band after UV excitation. The 1% doped Ce phosphor has high efficiency (84%) and a high color purity with CIE chromaticity coordinates (x = 0.157 and y = 0.069) close to the NTSC blue standard (x = 0.155; y = 0.070). The efficiency is higher than that of other oxy-nitridosilicate phosphors with emission maximum in the same region (410 – 440 nm). The emission band of $La_3Si_{6.5}Al_{1.5}N_{9.5}O_{5.5}$:Ce phosphor can be shifted from 418 nm to 450 nm, by changing the Ce concentration from 0.5% to 50%, which is caused by reabsorption and energy transfer. The energy of Ce from two crystallographic sites is very close, resulting in a stable emission color and a similar decay behavior independent of excitation wavelength. Compared to Ce doped $La_3Si_8O_4N_{11}$ phosphor, the quantum efficiency and thermal stability of emission for $La_3Si_{6.5}Al_{1.5}N_{9.5}O_{5.5}$:Ce phosphor have been improved without shifting the emission peak wavelength or changing the band gap. A very high color rendering (Ra = 93.2, R9 = 91.4, R12 = 89.5) white LED has been fabricated by using $La_3Si_{6.5}Al_{1.5}N_{9.5}O_{5.5}$:0.05Ce phosphor as the blue phosphor, showing the great potential of the phosphor for white LEDs.

A new Sr-sialon phase $Sr_{3.6}Si_{16.2}Al_{5.4}O_{3.6}N_{27}$ was discovered. With Eu doping the new Sr sialon phase shows blue to green emission after UV excitation depending on concentration. The phosphor has relatively low luminescence efficiency as a result of a fast thermal quenching. With Ce,Li doping the emission is in the deep blue region, with a much smaller redshift upon increasing the concentration and a much narrower emission band as compared to the Eu doped new phase. The Ce,Li doped Sr sialon phase has an internal efficiency up to 64%, which is slightly smaller than that of the Ce doped N-phase blue phosphor, but it has a better thermal stability.

The research described in this thesis shows some interesting results that seem to be promising for application or pave the way to future research. The availability of highly pure JEM phase will make it possible to investigate the structure in more detail, and the obtained high efficiency and good thermal stability make it more likely that JEM:Ce may be applied as an LED phosphor for home illumination. The energy level scheme of the lanthanides in JEM showed to be helpful in the interpretation of the

optical data, and constructing an energy level scheme may be useful for other hosts as well to predict and interpret the luminescence results. The Ce doped N phase seems to be promising for backlighting of displays, due to its efficient and narrow deep blue emission. For application in high power LEDs, the thermal stability would need to be further improved, which may be done by changing the chemical composition, optimizing the synthesis approach or by adding a protective coating layer on the phosphor surface. The newly discovered Ce doped Sr sialon phase also has a deep blue emission and a better thermal stability, making it very promising for white LEDs. However, its complex structure still requires a more thorough investigation.

List of publications and conferences

1. Publications

(1) Chun-Yun Wang, Takashi Takeda, Otmar Melvin ten Kate, Rong-Jun Xie, Kohsei Takahashi and Naoto Hirosaki. "Synthesis and photoluminescence properties of a phase pure green-emitting Eu doped JEM sialon ($LaSi_{6-z}Al_{1+z}N_{10-z}O_z$, z∼1) phosphor with a large red-shift of emission and unusual thermal quenching behavior", *Journal of Materials Chemistry C*, 2016, 4, 10358 - 10366.

(2) Chun-Yun Wang, Takashi Takeda, Otmar Melvin ten Kate, Masataka Tansho, Kenzo Deguchi, Kohsei Takahashi, Rong-Jun Xie, Tadashi Shimizu, Naoto Hirosaki. "Ce doped $La_3Si_{6.5}Al_{1.5}N_{9.5}O_{5.5}$, a rare highly efficient blue-emitting phosphor at short wavelength toward high color rendering white LED application", *ACS Applied Materials & Interfaces*, 2017, 9, 22665 - 22675.

(3) Chun-Yun Wang, Otmar Melvin ten Kate, Takashi Takeda, and Naoto Hirosaki. "Efficient and thermally stable blue-emitting Ce^{3+} doped $LaAl(Si_{6-z}Al_z)(N_{10-z}O_z)$ phosphor (JEM:Ce) for white LEDs", *Journal of Materials Chemistry C,* 10.1039/C7TC01697B.

2. Other

(1) Chun-Yun Wang, Otmar Melvin ten Kate, Takashi Takeda. "A promising green phosphor Eu doped $LaSi_{6-z}Al_{1+z}N_{10-z}O_z$, (z ~ 1) for white light emitting diodes", De Physicus, Delft University of Technology, November 2016, 3, 48 - 51.

(2) Otmar M. ten Kate, Rong-Jun Xie, Chun-Yun Wang, Shiro Funahashi, and Naoto Hirosaki. "Eu^{2+}-Doped $Sr_2B_{2-2x}Si_{2+3x}Al_{2-x}N_{8+x}$: A Boron-Containing Orange-Emitting Nitridosilicate with Interesting Composition-Dependent Photoluminescence Properties", *Inorganic Chemistry*. 2016, 55, 11331 - 11336.

3. Presentations at conferences

(1) Chun-Yun Wang, Takashi Takeda, Kohsei Takahashi, Rong-Jun Xie, Takayuki Suehiro, Naoto Hirosaki:"Preparation and luminescence properties of Eu^{2+} doped $LaAl(Si_{6-z}Al_z)(N_{10-z}O_z)$ phosphor", *Phosphor Safari 2015*, 7/27/2015~7/30/2015, Niigata, Japan (oral presentation).

(2) Chun-Yun Wang, Takashi Takeda, Otmar Melvin ten Kate, Naoto Hirosaki: "A novel blue-emitting Ce doped $La_3Si_{6.5}Al_{1.5}N_{9.5}O_{5.5}$ phosphor with high quantum efficiency for near UV LED", *ALP International Symposium*, 11/7/2016~11/9/2016, Sapporo, Japan (poster presentation).

(3) Chun-Yun Wang, Takashi Takeda, Otmar Melvin ten Kate, Rong-Jun Xie, Kazuko Nakajima, Naoto Hirosaki:"A new, highly efficient, blue-emitting Ce doped $La_3Si_{8-x}Al_xN_{11-x}O_{4+x}$ (x = 1.5) phosphor for UV LED", *Phosphor Safari 2016,* 11/28/2016~12/1/2016, Hong Kong, China (oral presentation).

(4) Chun-Yun Wang, Takashi Takeda, Otmar Melvin ten Kate, Masataka Tansho, Kenzo Deguchi, Kazuko Nakajima, Rong-Jun Xie, Tadashi Shimizu, Naoto Hirosaki: "Luminescence property and local structure of phase pure $La_3Si_{6.5}Al_{1.5}N_{9.5}O_{5.5}$:Ce phosphor", *The 64th JSAP Spring Meeting*, 3/14/2017~3/17/2017, Yokohama, Japan (oral presentation).

(5) Chun-Yun Wang, Takashi Takeda, Shiro Funahashi , Rong-Jun Xie , Naoto Hirosaki: "New phosphor Eu^{2+} and Ce^{3+} doped $Sr_{4-x}(Si,Al)_{19+x}(N,O)_{29+x}$ for white LED applications", *SPIE. Optics + Photonics 2017,* 8/6/2017~8/10/2017, San Diego, United States (oral presentation).

(6) Chun-Yun Wang, Takashi Takeda, Shiro Funahashi , Rong-Jun Xie , Naoto Hirosaki: "Ce doped $Sr_{4-x}Li_y(Si,Al)_{19+x}(N,O)_{29+x}$, an efficient and thermally stable deep blue-emitting phosphor for white LED application", *The 78th JSAP Autumn Meetings*, 9/5/2017~9/8/2017, Fukuoka, Japan (oral presentation).

Acknowledgements

Doing three years of PhD work would never have been possible without the help and support of any professors, colleagues, friends or family, and I would therefore like to use this moment to thank everyone who helped me throughout the last three years.

First of all I would like to thank my daily supervisor at NIMS professor Takeda. He helped me a lot, from assisting with spectroscopic measurements, to helping with the interpretation of the results and in writing my papers. I learned a lot from him during the last three years. At the same time I also very much appreciate that he gave me the freedom to design my own experiments and gave me the chance to attend several scientific conferences.

My thanks also go to my subadvisors at Hokkaido University, professor Kato and professor Tadanaga. Even though I did my research work far away from Hokkaido University, they still were able to give me some valuable comments and suggestions.

I want to thank all people from the Sialon group at NIMS who have, in one way or another, helped me with my research; Hirosaki-san for giving me the opportunity to do my PhD work in his group, and Xie-san for initially introducing me to the Sialon group while I was a Master student, as well as for his preparedness to make a white LED of my N-phase phosphor. My gratitude also goes to the research-assistants in the lab, especially to Nakajima-san, for doing many quantum efficiency measurements on the phosphors I prepared. In addition, I thank Yamamoto-san and Banna-san for firing some of my samples, Takahashi-san for sharing his ideas on the N-phase phosphor, Funahashi-san for the structural analysis of the new sialon phase and our secretary Seto-san for the administrative work. In addition I thank all group members who have given me useful comments and suggestions, such as during the monthly group meetings. I thank Melvin-san for the many valuable discussions that we had about my research work and for teaching me about the construction of an energy level scheme. I also appreciate the comments he gave about writing and revising my manuscripts.

From the people outside the Sialon group, my thanks go especially to Tansho-san and Deguchi-san, who both helped me doing the NMR measurements and interpreting the results, and to Shimizu-san for giving me the opportunity to do the measurements in his group.

I also thank my colleagues and professors worldwide who inspired me, gave me new ideas or learnt something new, for example at the conferences I attended. In this regard, I would like to thank especially

professor Ueda in Kyoto University for giving me very good suggestions and for inviting me to come to his lab and let me do the photoconductivity measurements.

Last but not least I would like to thank my friends and family for their support during my PhD study.

Chunyun Wang